Bruno Ribeiro

Analysis of the structure and central properties of a sample of massive bulgeless galaxies

Departamento de Física e Astronomia
Faculdade de Ciências da Universidade do Porto
Setembro de 2012

Bruno Ribeiro

Analysis of the structure and central properties of a sample of massive bulgeless galaxies

Tese submetida à Faculdade de Ciências da Universidade do Porto para obtenção do grau de Mestre em Astronomia

Departamento de Física e Astronomia
Faculdade de Ciências da Universidade do Porto
Setembro de 2012

"[S]ince every piece of matter in the Universe is in some way affected by every other piece of matter in the Universe, it is in theory possible to extrapolate the whole of creation - every sun, every planet, their orbits, their composition and their economic and social history from, say, one small piece of fairy cake."

Douglas Adams,
The Restaurant at the End of the Universe

To Ana,
The particle to my antiparticle,
The sun to my planetary system,
The dark matter to my galaxy,
The universe to my life.

Acknowledgments

First of all I would like to give a special thanks to my advisers Catarina Lobo and Sonia Antón for providing me guidance and knowledge without which this thesis would not be possible.

A grateful thanks to Jean Michel Gomes who collaborated with me in this thesis by providing stellar synthesis population results from STARLIGHT [1] for the samples, and also to Polychronis Papaderos for helpful comments and discussion.

An acknowledgement to the nancial support from project PTDC/CTE-AST/105287/2008 from FCT.

I would also like to acknowledge Chien Peng for making the GALFIT code publicly available and for the very comprehensive explanation on how it works on its website.

A special acknowledgment to all people who are part of the Sloan Digital Sky Survey [2] (SDSS) project.

Last, but not least, I thank Ana for all the support provided during this last year and for some insightful discussions on this matter.

[1]The STARLIGHT project is supported by the Brazilian agencies CNPq, CAPES and FAPESP and by the France-Brazil CAPES/Cofecub program

[2]Funding for the SDSS and SDSS-II has been provided by the Alfred P. Sloan Foundation, the Participating Institutions, the National Science Foundation, the U.S. Department of Energy, the National Aeronautics and Space Administration, the Japanese Monbukagakusho, the Max Planck Society, and the Higher Education Funding Council for England. The SDSS Web Site is http://www.sdss.org/.

Preface

In the beginning there were us, the sun and the moon. Shortly after, the planets joined the big picture, and stars, well, stars were just like light bulbs in the walls of the universe. We evolved, and along with us, so did technology Soon, new planets were discovered, the nature of stars was revealed, we were part of something bigger than ever thought possible. Years and years had gone by and we had a universe of our own, our galaxy. Like two fried eggs, *sunny-side up*, put together, back to back, with a disk , the glair, a bulge, the yolk, and the tiny drops of hot oil bouncing moving around like the globular star clusters of the halo. However, some *spots*, not like stars, in that perfect and heavenly world puzzled astronomers. Could there be other worlds like our own spread in a larger universe? In the early 20th century, we embraced that idea. There were other worlds outside our own, thousands and thousands of them, and as different from each other as humans are. Ones were giant balls of old stars without traces of dust and gas, others more like our own galaxy and with young and newly born stars, some with beautiful spiral patterns designed by their gas and dust harboring stellar *maternity wards*, and there are even some which appeared as a scrambled mix of dust, gas and stars, places of star birth. As humans, different galaxies belong to different places. The big old ones live together in big groups accompanied by small ones most like them, and the younger were roaming free through the fields of the universe or remained in the outskirts of the elder groups. The universe seems beautiful, an organized and wonderful place to live in. But we have yet to understand all of its wonders and mechanisms.

Abstract

The aim of this thesis is to study a sample of red massive bulgeless galaxies, selected from the SDSS DR7 based on an automated algorithm that performed one-dimensional analysis of the galaxy light profiles. From an initial sample of 77 bulgeless candidates we found 38 bulgeless galaxies and 29 galaxies with a pseudo-bulge regarding their large-scale structure using two-dimensional modeling techniques. An additional sample of 20 bulge-dominated candidates was selected to serve as a control sample and all of them were confirmed as bulgy galaxies after the two-dimensional analysis. We found that the disks of pseudo-bulge galaxies have larger effective radius than the bulgeless galaxies. Additionally, using the SDSS optical spectra, we assess some physical properties of the central regions of these galaxies (central 3"). We find that the bulgy galaxies show different properties (stellar mass, metallicity, mean stellar age, dust content) from bulgeless and pseudo-bulge galaxies and that the distinction between the last two classes of galaxies is only possible when considering central stellar mass and central velocity dispersions.

Contents

List of Figures

List of Tables

Chapter 1

Introduction

Historically, disk like galaxies were thought to have bulges that resembled small, elliptical galaxies residing in the center of their disks. In fact, these central structures were well described by the $r^{1/4}$ law, such as ellipticals [39], and presented colors similar to ellipticals. In particular, the more massive bulges that reside in the center of Sa and Sb type galaxies, are consistent with being flattened by rotation, they follow similar color-magnitude relations [4], similar metallicity-luminosity relations and similar fundamental plane relations [33] as those of elliptical galaxies. All this suggests that massive bulges form in the same way as ellipticals of intermediate luminosity (i.e. either by gravitational monolithic collapse or by hierarchical merging of smaller objects [3]).

As for small bulges (hereafter pseudo-bulges), their structure is closer to an exponential disk than to that presented by classical bulges [26], [42]. Their general properties include kinematics dominated by rotation with a flattened disk-like structure, low Sérsic index surface brightness profiles (predominantly with a value of $n < 2$) closer to that of exponential disks ($n = 1$) than that of classical bulges ($n = 4$), and inhabit galaxies that often host as well nuclear features such as bars, rings and small spiral structures and active star formation regions [26]. When establishing correlations, they deviate from the correlations presented by massive bulges [42] as the Faber-Jackson relation [25], which correlates bulge luminosity and bulge velocity dispersion, or the fundamental plane relation [22] which relates radius, velocity dispersion and surface brightness. When comparing the parameters retrieved from surface brightness profile fitting, pseudo-bulges also show a distinct behavior in the correlations between them (effective radius, surface brightness at half-light radius, absolute magnitude and Sérsic index) [26], [27]. Additionally, almost all pseudo-bulges show intense star-

formation activity, occupying the blue cloud locus in the color-magnitude diagram, and have lower fractions of stellar mass (in respect to the total mass of the galaxy) than classical bulges [30]. The pseudo-bulges of galaxies are thought to form via internal secular evolution of galaxies via inflows of gas driven by existing bars and spiral patterns [42]. However, more recent works show that minor mergers can mimic these secular evolution processes [23] in a sense that they can lead to the build up of the central mass of the galaxies and that merger-induced perturbations may transfer stars from the disk to the bulge [63]. Another alternative scenario states that an excess of low angular momentum mass in the central regions at the time of disk formation naturally produces a pseudo-bulge in galaxies [58]. In a recent work, Keselman & Nusser (2012), [37], showed through numerical simulations that it is possible to form pseudo-bulges from gas-rich major mergers of pure disk galaxies. However, several other works using simulations ([38], [53]) indicate that major mergers generally lead to systems with large bulges, so this is not yet a very consensual avenue. In conclusion, there are distinct possible explanations for the formation of pseudo-bulges but the dominant process is not known and additional dedicated work on the properties of these structures is needed to shed light on this subject.

On the opposite end of morphology classes are the galactic disks with negligible bulge component, the bulgeless galaxies. There are not many detailed studies of simple disks (see [36], [41]) but some studies on low surface brightness edge-on disks which are presumably valid for simple disks. Such studies seem to show that simple disks present lower surface brightness and rotate more slowly than disks with bulges [36]. Generally they have lower metallicities and present blue colors [45], being slightly bluer than those galaxies with bulges [36]. Despite their blue colors they show some old stellar populations [18] co-habiting with regions of ongoing star formation. However, they present low star formation rates thought to be associated with a low surface density of neutral atomic hydrogen (HI) [46]. Additionally they present a low amount of dust in a clumpy distribution [17].

Some very interesting issues regarding the evolution of these galaxies, that have lately become of interest and target of active research, concern in particular the putative existence of super massive black holes in the centers of bulgeless galaxies and their possible feedback on the galaxy star formation and the mechanisms responsible for the formation of pseudo-bulges in former pure disk galaxies. These subjects triggered a work by Coelho (2010), [15], that selected a sample of red massive disk-dominated galaxies from the SDSS DR7 for detailed analysis. In the framework of that general project, it was of the utmost importance to perform a detailed analysis of the structure

of the sampled galaxies to ascertain the significance of their bulge component. One of the main objectives of my thesis was to perform that assessment. Moreover, and given that both bulgeless and pseudo-bulge galaxies integrate the sample, the comparison of structural and spectroscopically derived parameters for both classes was also pursued. This was expected to characterize several of their properties and yield insight on the preferable formation scenarios of pseudo bulges, that could contribute to building a comprehensive theory of galaxy formation.

This thesis is organized as follows. In Chapter 2 I describe the samples used in this study. In Chapter 3 I present the description of the structure analysis method and the results obtained by its application to the samples. Chapter 4 briefly describes the method for retrieving physical properties from the optical spectra and respective results. Finally, in Chapter 5 I present my conclusions on the results obtained in this work.

Chapter 2

Description of the sample

The main focus of this study is to establish a detailed structural description of a set of galaxies in order to confirm them clearly as a class of red bulgeless candidates. Further analysis are also performed to characterize other properties of these galaxies (stellar populations, star-formation history (SFH), metallicities) to gain insight on the formation of pseudo-bulges.The initial sample from which this study was carried out is issued from the New-York University Value Added Galaxy Catalog [1] (NYU-VAGC, [8]) and compiled in [15]. The sample selection criteria is summarized in table 2.1 and justified below. Throughout this study, all calculations involving cosmological parameters used $H_0 = 71 kms^{-1}Mpc^{-1}$,$\Omega_m = 0.27$ and $\Omega_\Lambda = 0.73$ (WMAP7, [44]).

The lower redshift cut ($0.02 < z < 0.06$) applied serves as a filter to not consider galaxies with relevant contamination from their peculiar velocities in the determination of the redshift and to exclude possible sources with largely extended morphology from which the recovered SDSS spectra would correspond to the very central part of the galaxy (remembering that the SDSS fiber encloses 3" in the sky plane [62]). The higher limit in redshift was chosen so that the resulting galaxies have reasonable resolution which is very important since we are interested in modeling its morphology, and structural features tend to become unrecognizable in the images as we move towards higher redshifts. Considering the SDSS plate scale of 0.396"/pixel [62] at $z = 0.06$ one side of a pixel subtends $\sim$ 444pc which is smaller than the typical size of the bulge of a galaxy and so we are, in principle, capable of clearly classifying these galaxies as bulgeless candidates.

The stellar mass cut was primarily defined to favor the selection of galaxies whose star

[1] http://sdss.physics.nyu.edu/vagc/

formation might be affected by a given mechanism, AGN feedback, for the purpose of the study of Coelho (2010) [15].

As for the assessment of the bulge's significance, one of the commonly used ways to distinguish between bulge dominated galaxies and disk dominated galaxies is to fit a Sérsic profile [55]

$$\Sigma(r) = \Sigma_e exp[-\kappa(r/r_e)^{1/n} - 1] \tag{2.1}$$

where the Sérsic index n describes the shape of the light profile, r_e is the effective radius of the profile, Σ_e is the surface brightness at radius r_e and κ is a parameter coupled to n [14] such that half of the total flux is enclosed within r_e (see section 3.1.1). An index of $n = 1$ corresponds to a typical pure disk galaxy, whereas $n = 4$ corresponds to the de Vaucouleurs profile associated to elliptical galaxies. The values of n available in the NYU-VAG catalog were obtained through the fitting of equation 2.1 to azimuthally average radial profile convolved with the estimated seeing for each galaxy [8]. Following Bell (2008) [6], only galaxies with $n < 1.5$ were selected. This is a commonly used frontier value to select bulgeless galaxies.

The limits on color index $g - r$ and on the inclination parameter q_{am} are used to limit our sample to galaxies with little star-formation activity (again, for the original study purpose of the study of Coelho (2010) [15]) .

Since younger stellar populations emit strongly on the bluer part of the optical spectra and older stellar populations emit predominantly towards higher wavelengths , the color index serves as an indicator of the relative age of the stellar populations (see Figure 2.1). Following [6], red galaxies are defined as having $g - r > 0.57 + 0.0575 \log_{10}(M_*/10^8 M_\odot)$.

As we are interested in galaxies with low star-formation rates, one needs to distinguish between red galaxies dominated by old stellar populations and dust-obscured galaxies. It is well established that dust is mainly concentrated in the disks of the galaxies [11, Chapter 25]. This means that edge-on disk galaxies have a higher column density of dust that obscures the light of the younger stellar populations leading to an apparently red galaxy. So, setting a limit on the inclination of the galaxy, minimizes the inclusion of dust obscured objects in the sample. This is often made by setting a lower limit on the axis ratio (typically $b/a > 0.5$) for selecting galaxies. This usually works because the greater the inclination of the galaxy typically leads to a decrease in this ratio. However, the approach used in [15], uses the inclination parameter, q_{am} instead,

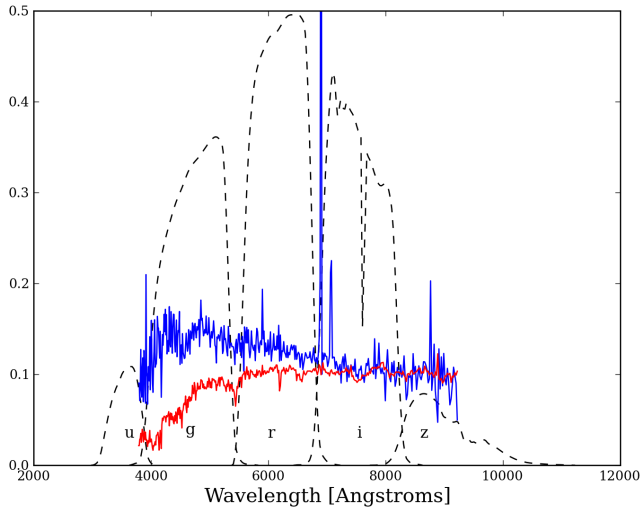

Figure 2.1: Sensitivity functions of the ugriz SDSS filter system. The blue line represents the optical spectra of a typical blue galaxy and the red line the optical spectra of a typical red galaxy. Both spectra were suitably normalized for viewing purposes. [29].

which might be a more robust indicator for the inclination

$$q_{am} = \left(\frac{1-E}{1+E}\right)^{1/2}, \ with \ E = \sqrt{m_1^2 + m_2^2} \tag{2.2}$$

where m_1 and m_2 are the second order adaptive moments of the galaxy's light profile [60] available in the NYU-VAGC catalog.

Table 2.1: Sample selection criteria. (z) Redshift, (M_*) Stellar mass, (n) r-band 1D Sérsic index, $(g-r)$ color index, (q_{am}) inclination parameter

Selection limits
$0.02 < z < 0.06$
$M_* > 10^{10} M_\odot$
$n < 1.5$
$g - r > 0.57 + 0.0575 \log_{10}(M_*/10^8 M_\odot)$
$q_{am} > 0.5$

2.1 The bulgeless nature of galaxies

Some of these parameters are too simplistic or occasionally produce wrong selections when applied automatically to large datasets. My work concentrates on the structure of a small set of galaxies: it is a detailed and dedicated analysis to provide confirmation of the bulgeless nature of these objects. Testing whether a galaxy is bulgeless or not is a delicate procedure. So in order to be certain about the structural parameters of the galaxies we wish to study, we need to be cautious about the objects we want to analyze. Bearing this in mind I started with the initial list of 113 objects that resulted from applying the previous criteria (see Table 2.1)and retained only those that passed a thorough visual inspection. The main reasons for the exclusion of an object are:

- Presence of dust lanes;
- Highly disturbed morphology;
- Overlapping of bright objects;
- Being the brightest cluster galaxy (BCG) with a bulgy shape;
- Presented obviously mis-computed colors.

The presence of dust lanes poses a challenge to 2-dimensional modeling of the galaxy since we have to take into account the decrease in brightness that affects the galaxy's light profile. Despite being possible to adjust a truncated Sérsic model we chose not to do it because it can produce unrealistic values of the Sérsic index since we do not have any central information on the true brightness of the stellar component of the galaxy. This is a conservative approach but we are focused on determining beyond any doubt the bulgeless character of these galaxies and the significant presence of dust may bias the model to unrealistic underlying profiles. Moreover the presence of dust shades doubt on the hypothesis that the red colors of the galaxy is mainly due to it being dominated by old stellar populations.

Disturbed morphology (asymmetries, tidal tails, distorted shapes) often indicates a recent or ongoing merger process which is known to likely induce a burst in star formation in gas-rich galaxies [56, Chapter 7]. Since we are interested in galaxies with low star-formation activity we chose not to include these objects in the sample. Also, the model decomposition would involve adding Fourier modes to the underlying models [50] which may affect the distinction between bulgeless and bulgy galaxies.

In the case of galaxies SDSS J083055.47+092838.0, SDSS J083404.99+434150.9 and SDSS J110509.38+380408.0 (see figure A.1) there is a bright object overlapping the galaxy's image (saturated stars in the two last ones) and due to impossible modeling of the separate components we chose to exclude these three galaxies as well.

NASA Extragalactic Database [2] (NED) classifies galaxies SDSS J004150.47-091811.2 and SDSS J122306.66+103716.4 as BCGs. These were erroneously selected due to having an extended stellar envelope that the automatic algorithm confused it with an extended disk.

The list of excluded objects and its exclusion motive are summarized in table 2.2. The color images (gri composite bands) are displayed on Figure A.1.

This conservative approach led to a sample of 77 galaxies on which this study will be based. The resulting sample may be consulted in Figure 2.2.

Table 2.2: List of excluded objects

Name	Exclusion Motive
SDSS J004150.47-091811.2	BCG
SDSS J075816.66+271029.5	Dust lane
SDSS J082205.75+562534.4	Dust lane
SDSS J083055.47+092838.0	Overlapping brigh object
SDSS J083404.99+434150.7	Overlapping brigh object
SDSS J084105.25+385439.3	Dust lane and Disturbed Morphology
SDSS J084958.78+381203.2	Dust lane
SDSS J091322.82+225156.9	Large magnitude errors
SDSS J091530.43+543129.7	Dust lane
SDSS J100204.32+505437.3	Dust lane
SDSS J102154.20+135356.4	Disturbed Morphology
SDSS J102238.05+231015.5	Dust lane
SDSS J102733.32+102018.9	Dust lane
SDSS J105804.22+170836.8	Dust lane
SDSS J110509.38+380408.0	Overlapping brigh object
SDSS J111718.56+293610.6	Dust lane
SDSS J112724.73+273714.2	Disturbed Morphology
SDSS J113732.29+092002.2	Dust lane
SDSS J114517.35+271634.4	Dust lane

[2] http://ned.ipac.caltech.edu/

Table 2.2 (continued)

Name	Exclusion Motive
SDSS J120559.45+022953.6	Dust lane
SDSS J120800.34+231307.5	Dust lane
SDSS J120801.37+325622.0	Large magnitude errors and Disturbed Morphology
SDSS J121611.87+592315.2	Dust lane
SDSS J121748.54+463454.9	Dust lane & Merger
SDSS J122306.66+103716.4	BCG
SDSS J123226.76+444339.7	Dust lane
SDSS J125227.71+600400.6	Disturbed Morphology
SDSS J131148.02+305821.3	Dust lane
SDSS J134139.23+554014.0	Disturbed Morphology
SDSS J135600.11+173041.7	Dust lane
SDSS J143351.99+272042.8	Dust lane
SDSS J160753.53+101609.7	Dust lane
SDSS J165251.83+360541.2	Dust lane
SDSS J170024.77+382115.5	Disturbed Morphology
SDSS J223002.77-001652.6	Disturbed Morphology
SDSS J230211.71+142829.0	Dust lane

2.2 Control Sample

For comparison and to test the performance of the structure-determination algorithm and other methods used in this work, besides selecting the main sample for this study consisting of bulgeless galaxies as assessed by the 1D profile fitting, an additional set of bulge-dominated galaxies was assembled. The bulgy galaxies obey the same selection criteria as the bulgeless sample in what regards the redshift interval, the stellar mass and the $g - r$ color index. No selection was performed based on the inclination parameter because we do not expect dust to be very abundant in this class of objects [56, Chapter 6] so a selection on their inclination is not relevant for our purposes. Only galaxies with a Sérsic index of $4 < n < 5.5$ were selected. This interval of Sérsic indexes was defined as such so that these galaxies had preferably no disk component to assess the differences in general properties that may arise. These were all elliptical galaxies. From all the galaxies selected in this way, twenty were

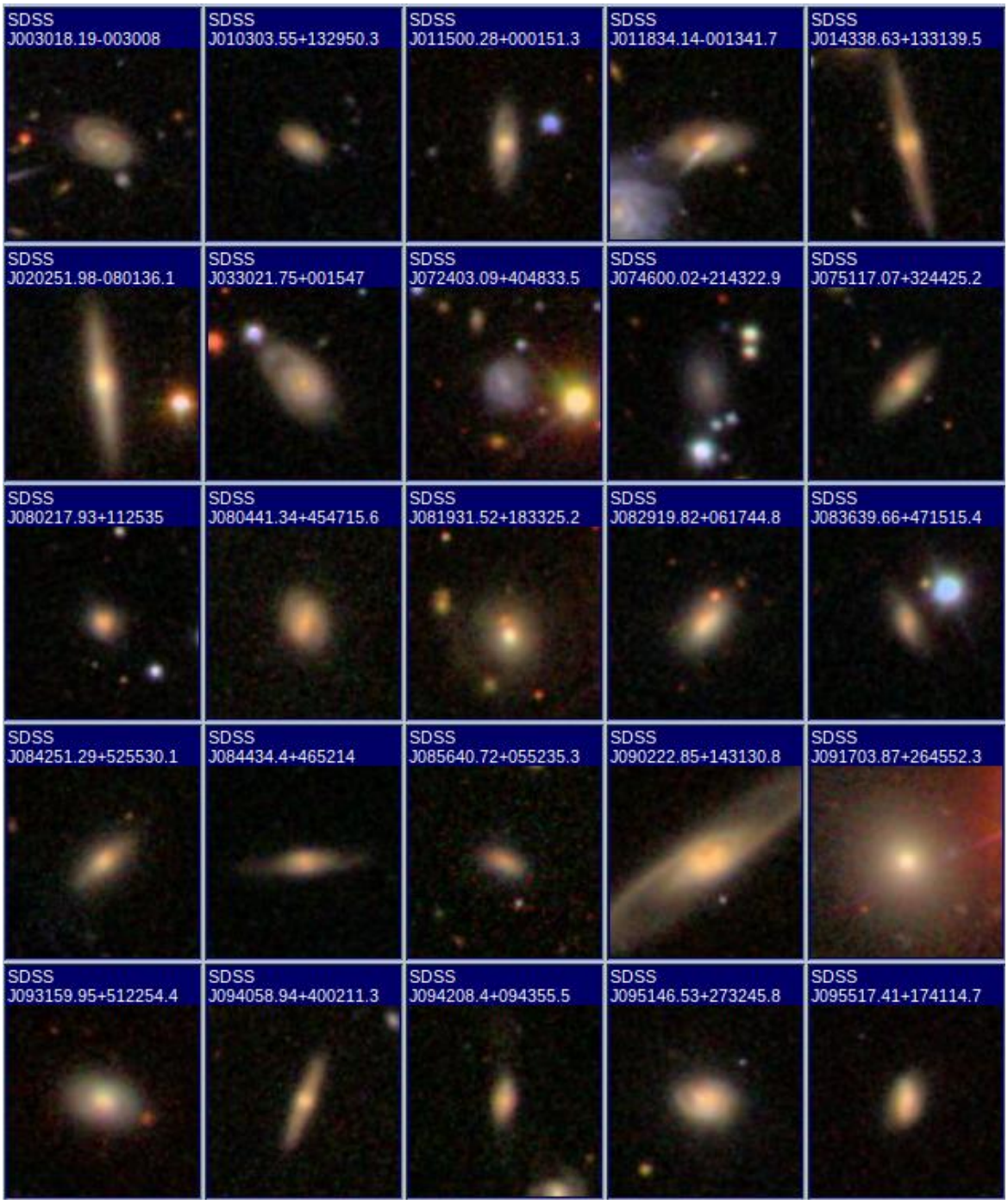

Figure 2.2: Color (gri bands) images of the 77 galaxies in the final sample.

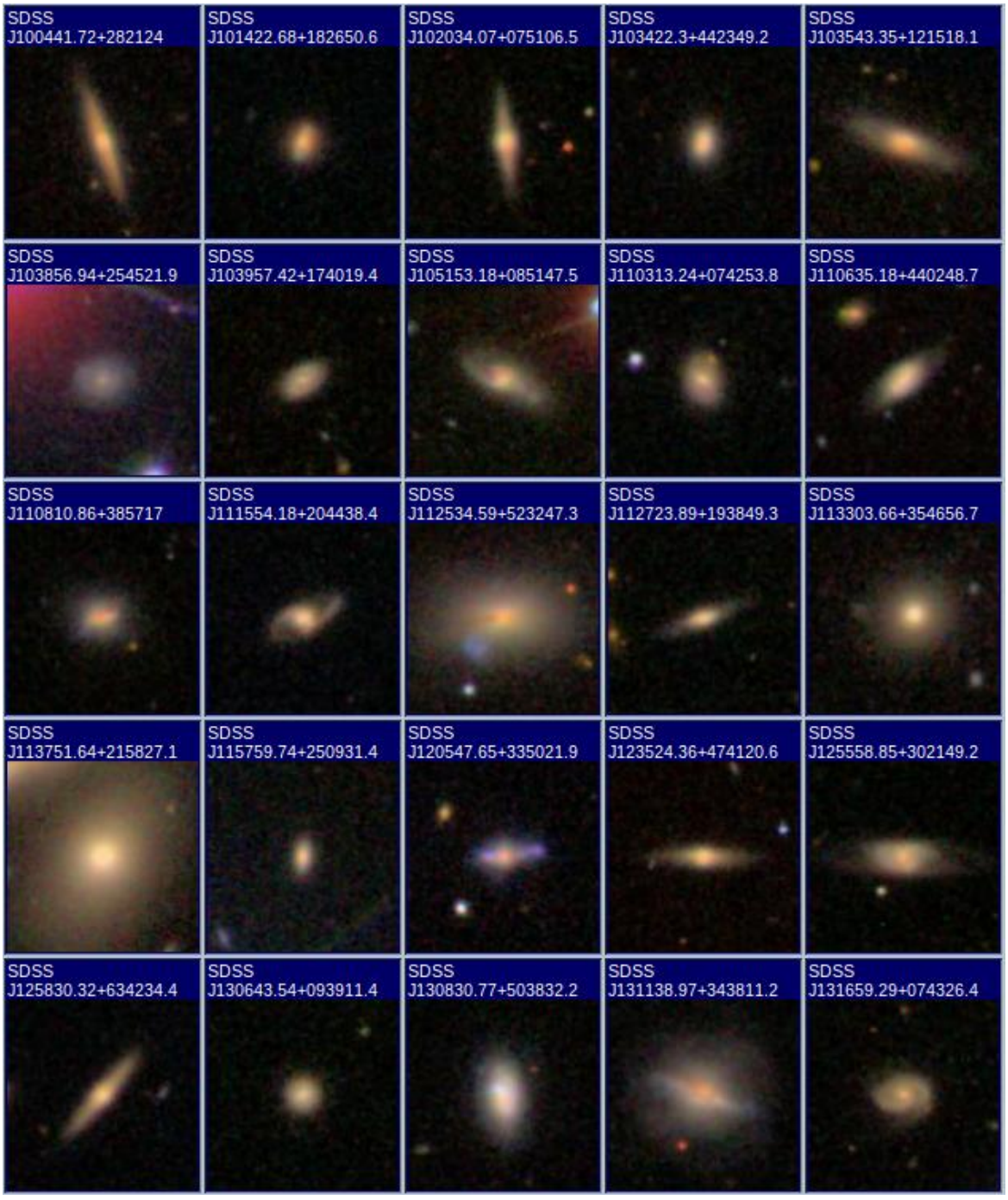

Color (gri bands) images of the 77 galaxies in the final sample. (continued)

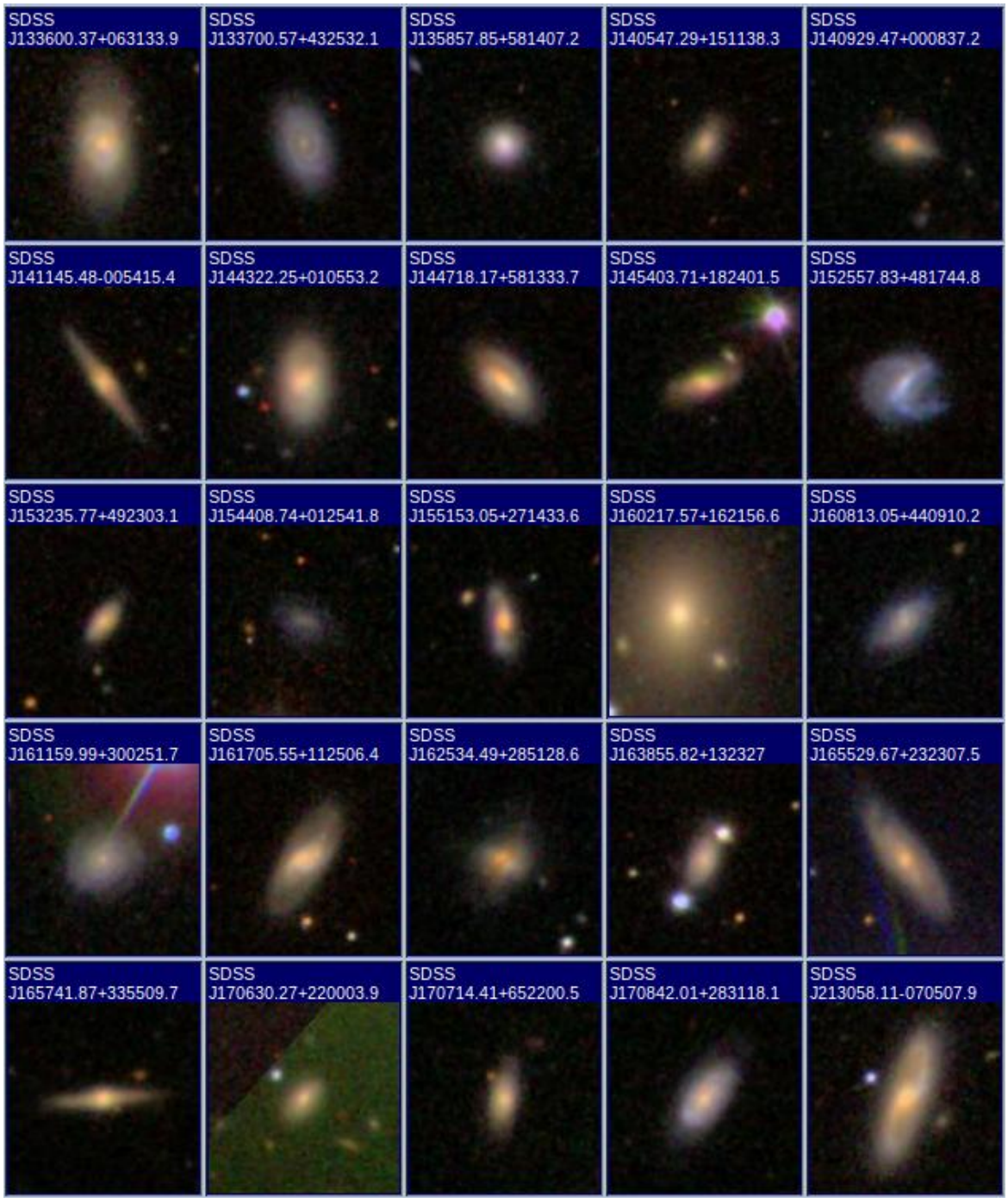

Color (gri bands) images of the 77 galaxies in the final sample. (continued)

Color (gri bands) images of the 77 galaxies in the final sample. (continued)

chosen by visual inspection to guarantee the goodness of the selection criteria (see Figure A.2). This control sample serves the purpose of investigating the recovered values by the two-dimensional modeling, to test if galaxies with a prominent bulge can be misclassified as bulgeless by this procedure and to compare with the results of the bulgeless sample so that we can test if they have different general properties.

Chapter 3

Structure analysis of the sample galaxies

Since the dawn of modern astronomy galaxies have been classified by its general shape. In 1926, Edwin Hubble proposed a classification scheme [32] where galaxies where grouped into ellipticals (with a sub-indicator for its ellipticity), spirals (normal and barred) and irregulars. This was later extended by Gérard de Vaucoulers in 1959 [21] for the inclusion of ring-like features, weak bars and apparent irregulars with some structure. Later, van den Bergh introduced an extra classification system based on the regularity of the spiral patterns [57]. Since then, several morphological classification schemes have been proposed as more robust and physically meaningful (i.e. linked with galaxy's properties such as star-formation history, mass assembly, past merger, etc.). Examples of this new type of schemes are the CAS system [16] and the EFIGI catalog (*Extraction de Formes Idealises de Galaxies en Imagerie*) [19].

Whilst qualitatively the original schemes have proven useful in understanding some fundamental relations between morphology and other properties of the galaxies (e.g. gas content, colors, star -formation rate, etc.), as the number of observed objects increased drastically with the evolution of technology, quantitative information was required to treat statistically the samples and address these scientific questions. One of the first and rather straightforward approaches consisted in using simple radial profiles for adjusting the galaxies' surface brightness: the $I(R) \propto e^{R^{1/4}}$ law proposed by de Vaucouleurs [20] reproduces well the shape of elliptical galaxies and, in combination with the exponential disk ($I(R) \propto e^{-R}$), one can reproduce the spiral galaxies' profiles [28]. These profiles were generalized by Sérsic [55] (see equation 2.1) where n can be

chosen to mimic both the de Vaucouleurs law and the exponential disk as well as to assume other values and better describe the continuous and more general shapes of galaxies.

Nowadays there are two different approaches to quantitatively classify galaxies according to their basic structure. One consists in performing one-dimensional fitting of the surface brightness profile which collapses the information of the two-dimensional image into a radial profile. Although this procedure is straightforward in its practical application, on the one hand. the passage from the image to the radial profile is not unique [50], and, on the other hand, any asymmetrical features (like arms, dust lanes, disturbed morphology, etc.) are diluted in the extracted radial profile.

Alternatively, two-dimensional techniques are now used to perform this kind of analysis, and they have been shown to better retrieve the real values through simulations [61], [31]. This type of studies not only allows us to retrieve more realistically the structural parameters when empirical laws are applied to galaxies' profiles but also provides some information on hidden details of galaxy structure which can give hints on the past history of the galaxy and provides new insights on its evolution (clumps in residuals may indicate ongoing star formation, asymmetrical features can be due to past interactions, etc.). The code used in this thesis was the publicly available GALFIT [1] - [49], [50] version 3.0 that is very flexible and has been largely tested and applied in several cases.

3.1 Detailed Decomposition of Galaxy Images using GALFIT

GALFIT is a 2-D image decomposition program written in the C language. Its high degree of flexibility allows one to fit any amount and combination of components to one image limited only by computer memory and speed.

As every observation has its own specifications on what concerns the instruments used and atmospheric conditions, it is important, if one wishes to measure the intrinsic profile of the object, to take into account these effects. This can either be done by deconvolution of the original image or by convolution of the proposed model using an appropriate point spread function (PSF). GALFIT was programmed to use the second process because it performs well even on low signal-to-noise ratio (S/N) images

[1] http://users.obs.carnegiescience.edu/peng/work/galfit/galfit.html

whereas the first one requires high S/N. The drawback of convolving the model instead of the original image is that this must be performed for each model that is generated, increasing the computational time needed.

The way GALFIT proceeds is to adjust a model to the image and chose the best one by minimizing the χ^2_ν (the reduced χ^2), which is defined as [49]:

$$\chi^2_\nu = \frac{1}{N_{dof}} \sum_{x=1}^{n_x} \sum_{y=1}^{n_y} \frac{flux(x,y) - model(x,y)}{\sigma(x,y)} \tag{3.1}$$

where

$$model(x,y) = \sum_{\nu=1}^{n_f} f_\nu(x, y, \alpha_1, ..., \alpha_n) \tag{3.2}$$

N_{dof} is the number of degrees of freedom in the fit, n_x and n_y are the sizes in the x and y dimensions respectively, $flux(x,y)$ is the flux of the image in the pixel x, y, $model(x,y)$ is the sum of the n_f model functions f_ν required, where $\{\alpha_1, ..., \alpha_n\}$ are the model parameters and $\sigma(x,y)$ is the Poisson error of the counts at each pixel which is generated from the image header keywords' *gain* and *readnoise*.

The inner working of GALFIT is summarized as follows:

1. Normalize and prepare the input PSF image for convolution;
2. Cut the section of the original input image containing the object to be fitted;
3. Generate model images based on the parameters (on the first run it uses the initial parameters estimates);
4. Cut the section of the model that corresponds to the convolution region [2] ;
5. Convolve the model with the input PSF using Fast Fourier Transforms(FFT) technique;
6. Copy the convolution region into the model image of step 3 to replace the cut in step 4;

[2]In most of the images of this master thesis the convolution region is equal to the size of the image that contains the object to be fitted.

7. Compare the model with the original image. Minimization is done using the Levenberg-Marquardt downhill-gradient method/parabolic expansion [52];

8. Iterate from step 3 onwards until convergence is reached;

9. Output model and residuals images and final parameter files;

The change in the model parameters at each step is determined by selecting a direction for which the gradient of the function is negative in order to get closer to a minimum. Convergence is reached when $\Delta\chi^2 < 5 \times 10^{-4}$ for 5 consecutive iterations.

I will detail the steps of running GALFIT in the following sections.

3.1.1 GALFIT functions

Despite having a wide variety of models available (Sérsic, Moffat, Nuker, spiral patterns, Fourier modes and more [50]) that one can use to fit the galaxies, this study wishes to establish comparisons with previous works ([6], [30]) and focuses on establishing the significance of the bulge and disk components for the sample galaxies (not concentrating on other morphological features), so only Sérsic profiles and PSF components (in cases where fitting of nearby stars is needed) were used in the context of this thesis.

The Sérsic profile.

The Sérsic profile is described by the mathematical law given in equation 2.1. It is important to note that GALFIT uses a parametrization of $\kappa(n) \approx 2n - 0.331$ [49].

On GALFIT, each Sérsic model has potentially seven free parameters: the position of the center, given by x_c and y_c, the total magnitude of the model, m_{tot}, the effective radius, r_e, the Sérsic index, n, the axis ratio of the ellipse, b/a and the position angle, θ_{PA}, which refers to the angle between the major axis of the ellipse and the vertical axis and has the sole purpose of rotating the model to match the galaxy's image.

The conversion between Σ_e and total magnitude (m_{tot}) is performed through the integration of the Sérsic profile out to $r = \infty$ for a set of fixed parameters (n,b/a and r_e)

$$F_{tot} = \int_0^\infty \Sigma(r) = 2\pi r_e^2 \Sigma_e e^\kappa n \kappa^{-2n} \Gamma(2n)(b/a) \tag{3.3}$$

where $\Gamma(2n)$ is the Gamma function at $2n$. The integrated total magnitude is then calculated by:

$$m_{tot} = -2.5log_{10}\left(\frac{F_{tot}}{t_{exp}}\right) + m_{zpt} \tag{3.4}$$

where t_{exp} is the exposure time given in the image header and m_{zpt} is the magnitude photometric zeropoint, also provided in the header of the image.

Smaller m_{tot} means greater model flux. Higher values of n mean steeper profiles for $r < r_e$ whereas lower values mean flatter, less centrally concentrated profiles. An axis ratio of $b/a = 1$ means the model is a perfect circle and moves towards 0 with increasing ellipticity (the case of $b/a = 0$ corresponds to an infinitely thin disk). A value of $\theta_{PA} = 0°$ means that the major axis is vertically aligned, a positive value (with $\theta_{PA} < 90°$) means an angle between the major axis of the ellipse and the vertical axis measured in the counter-clockwise direction and a negative value (with $\theta_{PA} > -90°$) means that this angle is measured in the opposite direction.

3.1.2 Original images

Since we are mostly interested in fitting the underlying global stellar component of the galaxies, all modeling was performed using r-band images from SDSS DR7 [3] [1] which are also the highest quality ones. All necessary images were downloaded from the SDSS Data Archive Server[4] (DAS): these are the corrected image frames, that have been bias subtracted, flat-fielded, purged of bright stars, and the header updated with the latest calibrations.

Each field of view has 2048×1489 pixels of coverage which correspond to $13.5' \times 9.8'$ in the sky.

3.1.3 Testing for variations of the input point-spread function (PSF)

Convolution with a PSF image is important for the modeling of a galaxy. However, since we are not interested in small, unresolved sources, a perfect model of the PSF

[3] http://cas.sdss.org/dr7/en/
[4] http://das.sdss.org/www/html/

is not needed. With that in mind, the input PSF image to be given for GALFIT modeling of the galaxies was chosen as a bright, isolated and non-saturated star from the same field of view of each galaxy. This has the advantage (relatively to a model PSF) of sharing the same observing conditions as the galaxy being modeled, and consists in a more realistic choice.

To assess the impact of the chosen PSF on the structural parameters retrieved from GALFIT, I randomly selected three different galaxies (their SDSS r-band images can be seen on Figure 3.1) on which GALFIT was performed using, for each galaxy, three different isolated stars from the corresponding field, located at different distances from the galaxy. The results concerning the Sérsic index are summarized in table 3.1, and in Figures 3.2, 3.3 and 3.4 one can see the GALFIT visual outputs where no differences between the different models are noted.

All the parameters show some variation resulting from different PSF input images but the amplitude of that variation is always below the 8% level and does not change significantly the Sérsic index that is derived, i.e., the galaxy class, determined according to n does not change when different stars are used to model the PSF.

Despite noting that the retrieved parameters depend on the input PSF image, this is a minor dependence, and the resulting values give me confidence that this variation will not affect the conclusions regarding the bulgeless nature of these objects nor any result from this thesis. Although a generalization to the other fields is not possible (due to the different observing conditions), the variation of the PSF (on the untested cases), expected to be small (due to the reasonable degree of uniformity of the survey dataset), will not affect, in principle, the conclusions.

3.1.4 Models used in the image decomposition

It is important to point out that the main aim of this study is to assess the significance of the bulge on the light profiles and does not concern other morphological features such as spiral arms, clumps of light, rings, etc. With that in mind, the selection of bulgeless galaxies is a very sensitive subject because the automatized treatment of large data sets such as the SDSS can lead to morphological misclassifications due to galaxy substructure, asymmetrical features or misclassification of a merger as a single galaxy. This work follows the selection criterion of [6] which indicates a cut in Sérsic index of $n < 1.5$ to define a galaxy with little or no contribution of a bulge-like component (hereafter pseudo-bulge) to its morphological profile. However, in the

Table 3.1: Summary of the results for the PSF variation test. The presence of two Sérsic indexes means the model has two components. The mean value refers to the mean of the three output values for each input PSF.

Name	Parameter	Mean Value	Standard deviation
SDSS J154408.74+012541.8	FWHM[a]	2.54	0.01
	n	1.17	0.05
SDSS J020251.99-080136.1	FWHM[a]	3.20	0.13
	n_1	0.91	0.06
	n_2	1.00	0.02
SDSS J221917.33-011113.7	FWHM[a]	2.56	0.10
	n_1	0.84	0.00[b]
	n_2	0.50	0.04

[a] Full Width at Half Maximum (in pixels) retrieved from IRAF routine imexamine for the PSF.

[b] All three cases have the same index.

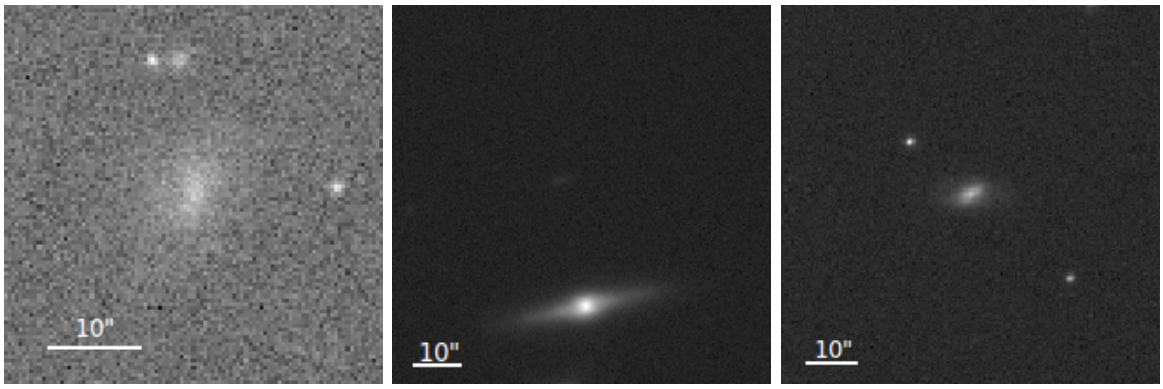

Figure 3.1: SDSS r-band images for the three galaxies used for the PSF test. From left to right: SDSS J154408.74+012541.8, SDSS J020251.99-080136.1 and SDSS J221917.33-011113.7. The offset in the middle image has been applied in order to mask out a saturated star.

Figure 3.2: GALFIT output residuals for the modeling of SDSS J154408.74+012541.8 using three different input PSF images. The distance of the PSF to the galaxy increases from left to right.

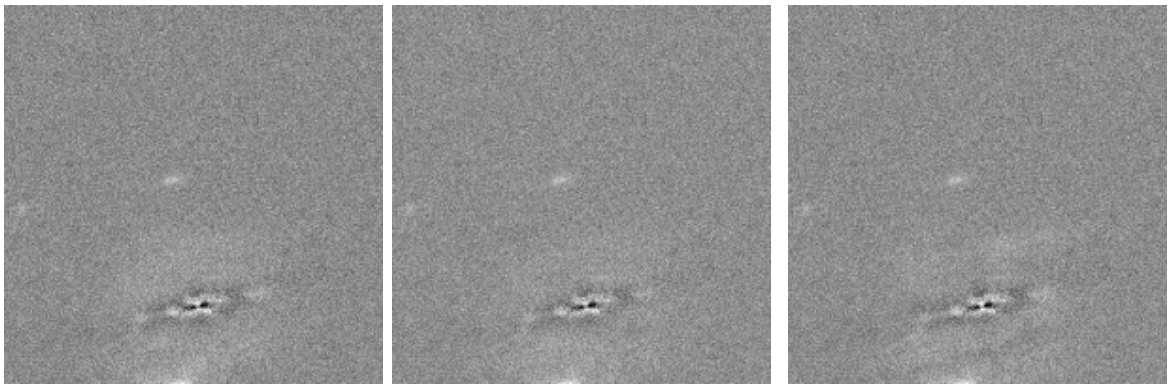

Figure 3.3: Same as figure 3.2 for SDSS J020251.99-080136.1

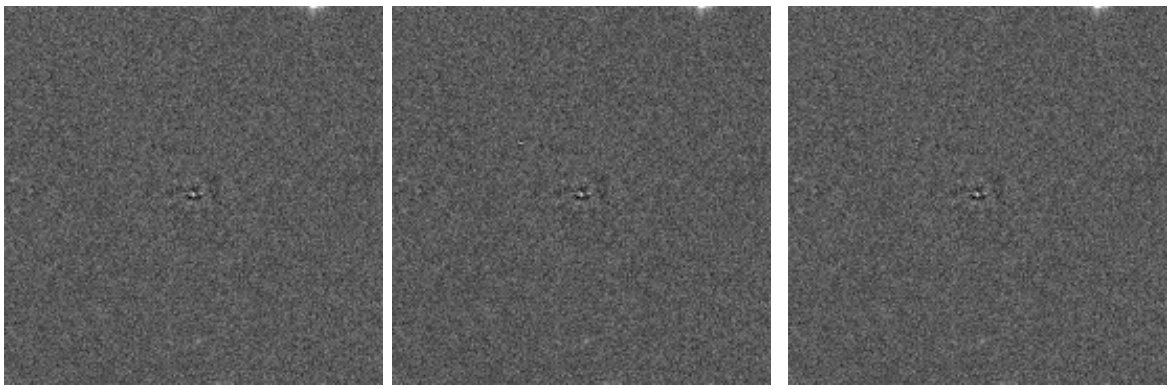

Figure 3.4: Same as figure 3.2 for SDSS J221917.33-011113.7

work of Gadotti (2009) and others ([30], [5]), where a similar method was applied, the selection cut on the index was a little higher ($n \leq 2$). Since the value of n varies continuously from a Gaussian profile ($n = 0.5$) to an exponential disk ($n = 1$) and to a classical bulge ($n = 4$) it is not easy to set a limit to separate bulgy galaxies from those with no bulges or with pseudo-bulges. But $n < 1.5$ should be conservatively safe.

In this work I designed two strategies to study the global structure of these galaxies and tackle the problem of their morphological classification. Firstly, a n-free Sérsic profile was fitted to all galaxies and a second n-free Sérsic component was added whenever the residuals indicated some remaining coherent structure. Secondly, and in alternative, a fixed Sérsic profile with $n = 1$ (exponential disk) was fitted to all galaxies and a second n-free Sérsic profile was added only when necessary. Despite knowing that no two galaxies are alike and that restricting the value of one of the Sérsic indices leads to a bias in the distribution of the free n of the second component,, there is degeneracy of the profile due to variations in the other parameters, namely the effective radius, r_e, which may cause two profiles with different Sérsic indices to adjust equally well the same galaxy. I have tested and I am confident that the second strategy is more robust against possible variations in the parameters and leads to more physically meaningful results. Thus, the classification of galaxies obtained in this way is more reliable and, therefore, the second model shall be preferentially adopted in this work.

The final classification scheme for these galaxies divides them in three main groups:

- **Bulgeless Galaxies** - well adjusted by a single exponential disk;
- **Pseudo-bulge Galaxies** - galaxies which require a second component with $n < 1.5$
- **Bulgy galaxies** - galaxies which are best modeled with a n-free Sérsic profile with $n > 2$

3.1.5 Input files and parameters

In order to model a galaxy, GALFIT needs a set of input images and values to produce reliable results.

The input image is, by default, a section of the field centered on the galaxy to fit (whenever not possible - because some galaxies are close to the CCD edge or have

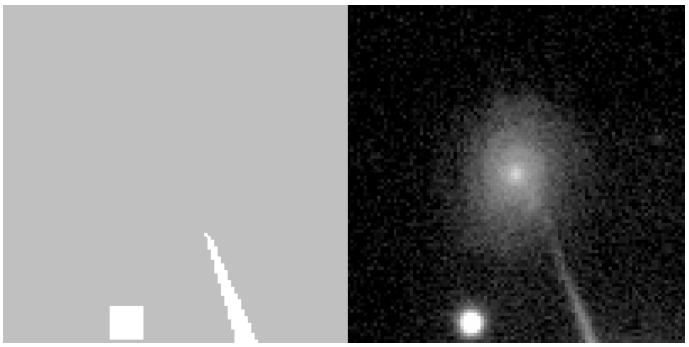

Figure 3.5: Mask applied to SDSS J161159.399+300251.7 image on the left and SDSS r-band image on the right. The white pixels represent the bad pixels which GALFIT will not take into account.

saturated objects nearby - an offset was applied provided that all the galaxy's emission was still contained in the region and any problematic object excluded). The limits of the region were defined so that it can have a significant portion of sky in it while minimizing the number of objects present there.

Whenever a saturated star nearby could not be excluded from the region to fit, a mask file preventing GALFIT to account for the saturated pixels was provided. The mask is a polygon region surrounding a problematic object defined using ds9 [35] regions tools and then converted to a bad pixel list using the algorithms provided in the help pages of GALFIT [5] . One can see an actual mask used for galaxy SDSS J161159.399+300251.7 in figure 3.5.

The PSF input image is an isolated, bright and non-saturated star from the field as close to the galaxy as possible, from which the sky value present in the image header was subtracted.

The magnitude photometric zero point and the sky level were retrieved from the image header of each field. The plate scale of the CCD can be found in [62].

Despite being somewhat insensible to the initial set of parameters for the Sérsic function in the case of simple modeling by one component, one must not provide unrealistic values since that compromises convergence. In that sense, rough estimates of x_c, y_c, r_e, b/a and θ_{PA} were retrieved with the help of ds9 tools. The initial value for n was taken from the NYU-VAGC and m_{tot} was taken from the SDSS navigate tool information [6] .

[5] http://users.obs.carnegiescience.edu/peng/work/galfit/MASKING.html
[6] http://cas.sdss.org/dr7/en/tools/chart/navi.asp

In the case of adding a second component, and because the first component usually fits the extended emission of the galaxy, the initial parameters were set as follows: x_c, y_C ,θ_{PA} and m_{tot} were the same; b/a was set to a higher value close to 1 to reflect the possible existence of a spheroidal component; n was set to a higher value to reflect the steeper central profile characteristic of a spheroidal component and r_e was set to a lower value as we expect the spheroidal component of the galaxy to be more concentrated than the disk. In the particular case when a first component was fixed to be an exponential disk ($n = 1$), the second component was set to have an initial value of $n = 4$, that of a classical bulge.

Also, since in some cases there are nearby galaxies and stars that are included in the region to fit, I enabled GALFIT to model these objects too (as indicated in section 3.1.1), to minimize contamination from light of other objects other than the galaxy we are studying.

An example of an input file is given in Appendix B.

3.1.6 GALFIT based exclusion

The GALFIT results enable us to re-assess more confidently the structure of the galaxies in the departure sample of 77 objects. Based on those results, we further narrowed the sample as justified below.

Three objects, SDSS J154408.74+012541.8, SDSS J230751.49+142333.5 and SDSS J074600.04+214323.2, were excluded since they are very faint sources. Consistently, their SDSS spectra are very noisy.

Three other objects, SDSS J162534.52+285129.0, SDSS J110810.87+385717.0 and SDSS J112534.58+523247.0, were excluded because they present dust lane features in the r-band images that are also evident in GALFIT residuals, as can be seen in Figure 3.6.

Finally, four objects,SDSS J113303.66+354656.7, SDSS J091703.88+264552.3, SDSS J160217.56+162156.6 and SDSS J081931.52+183325.2, were excluded due to the high values of the Sérsic index retrieved from GALFIT modeling using a single n-free Sérsic model ($n > 4$ for all of them) as the best fit. These were also confirmed when trying a combination of disk+Sérsic models where the second component turned out to dominate the fit (exponential disk would become too faint in the presence of the second n-free Sérsic component) and presented a Sérsic index always greater than 3.

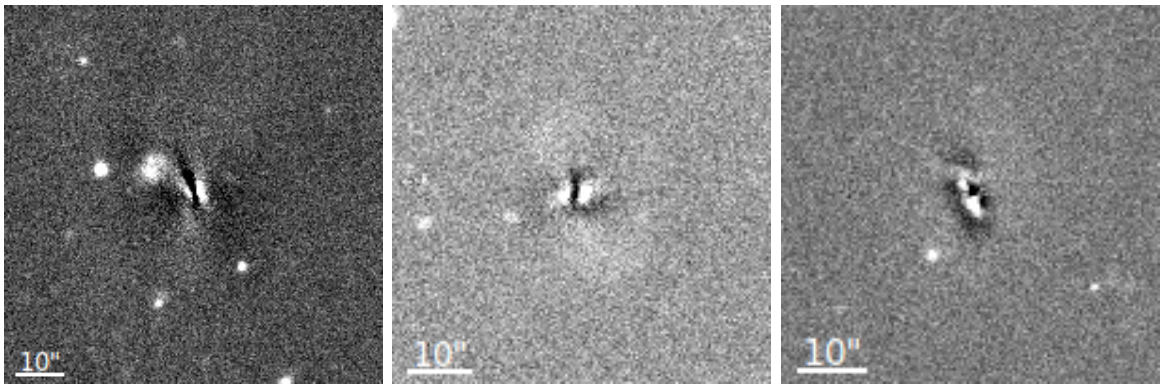

Figure 3.6: GALFIT residuals for the three galaxies presenting dust lane features. From left to right: SDSS J112534.58+523247.0, SDSS J162534.52+285129.0 and SDSS J110810.87+385717.0.

After this re-assessment, 67 galaxies were selected as the bulgeless and pseudo-bulge candidates on which this thesis results are based on.

3.2 Construction of surface brightness profiles

As described in the beginning of this chapter, one of the ways to quantify the structure of a galaxy is to adjust a function to its one-dimensional light profile. In this work one-dimensional light profiles of the galaxies were computed, though no fitting was performed, and compared with that of the models to provide a better visual inspection of the profiles.

The reason behind not simply using the GALFIT output parameters to describe the models is because the models are convolved with a PSF for comparison with the original galaxy image. If one wishes to reproduce the same results in a one-dimensional fashion using directly the GALFIT output parameters, the Sérsic function must be convolved with the correspondent one dimensional PSF model, or a deconvolution of the galaxy's image has to be performed. Since deconvolution of the galaxy's image depends on high S/N and one-dimensional convolution is mathematically different than the two-dimension convolution performed by GALFIT I chose to extract the one-dimensional profiles directly from the output image models provided with the GALFIT results.

This was made using the *ellipse* routine designed for the Image Reduction and Analysis

Facility [7] (IRAF) and part of the Space Telescope Science Data Analysis System [8] (STSDAS) package.

3.2.1 STSDAS *ellipse* routine

This routine, described in detail in [34], is used to produce one-dimensional surface brightness profiles from two-dimensional images. I will next describe briefly how the isophote fitting is performed by this task.

All my work was performed in interactive mode so visual inspection of the fitting, especially in the outer regions of the galaxy, could be done to control the performance of the algorithm and its results.

The fitting starts with a set of four initial parameters: the center of the isophote, given by x_c and y_c, the ellipticity, defined as $\epsilon = 1 - b/a$, and position angle, θ. Then it proceeds to a least-squares minimization of the fitting function (a Fourier transform of $I(r)$)

$$I(\theta) = I_0 + \sum_{n=1}^{4} A_n sin(n\theta) + B_n cos(n\theta) \tag{3.5}$$

where I_0 is the intensity of the isophote, and the parameters A_1, A_2, B_1 and B_2 are the amplitude of the harmonics whose value is a measure of how much the input parameters of the ellipse (each one relates to a specific parameter) are wrong, i.e. small values of this amplitudes mean that the input parameters are correct and the larger the values the greater the error of the parameter in relation to that which represents the isophote we are considering. Parameters with $n = 3, 4$ give information on how much the isophote deviates from a true ellipse. The correction factors of the ellipse parameters for a specific isophote are computed as follows:

$$\begin{aligned} \Delta x_c &= -\tfrac{B_1}{I'} \\ \Delta y_c &= -\tfrac{A_1(1-\epsilon)}{I'} \\ \Delta \epsilon &= -\tfrac{2B_2(1-\epsilon)}{a_0 I'} \\ \Delta \theta &= \tfrac{2A_2(1-\epsilon)}{a_0 I'[(1-\epsilon)^2-1]} \end{aligned} \tag{3.6}$$

[7] http://iraf.noao.edu/

[8] STSDAS is a product of the Space Telescope Science Institute, which is operated by AURA for NASA and available through http://www.stsci.edu/institute/software_hardware/stsdas

where I' is the derivative of the intensity along the major axis evaluated at the semi-major axis length of the isophote being considered, a_0. The parameter with the greatest deviation is changed according to equations 3.6 and a new minimization is calculated until convergence is reached. For a good fit the value of $I(\theta)$ should be constant for all values of θ. Then it proceeds to the next value of semi-major axis, a_0, length by an increment step indicated in the input file. Once the outer regions of the galaxy are reached, i.e. the mean isophotal intensity approaches 0, I reverse the isophote fitting to start calculating the isophotes in the inner regions (with $a_0 < a_i$ where, for most cases, $a_i = 10$pixels). Then the process continues automatically (but still visually inspected) since for the inner regions the intensity values are high enough to perform consistent calculations. To exclude light excess in the outer regions of the profiles due to contamination by nearby bright stars the same mask used in GALFIT modeling was applied in the ellipse routine.

There are other output parameters that are not described here because they were not used as I am only interested in obtaining the brightness profiles of the galaxies.

The output, $I(r)$, was then converted to represent a surface brightness profile by

$$\mu(r) = -2.5log_{10}\left(\frac{I(r)}{s^2 t_{exp}}\right) + m_{zpt} \tag{3.7}$$

Where s represents the scale factor for conversion between pixel and arcseconds. This procedure was done for sky-subtracted galaxy images and GALFIT output models (for separate components whenever necessary).

3.3 Structure Results

The final GALFIT best model for each galaxy was chosen based mainly on two criteria. The first imposing that $\Delta n/n < 15\%$ (where Δn is the associated error resulting from GALFIT) and the second based on the appearance of the output surface brightness profiles. The results are summarized in table 3.2. Since one cannot expect that simple Sérsic laws will model every detail of every galaxy, most of them present noticeable residuals. There are cases where residual light is over 10% of its original value. However these pixels refer either to galaxies substructures (mainly spiral arms and sometimes small clumps) and to small central sources whose extent is typically that of the size of the PSF image and therefore refer to an emission that is not adjustable

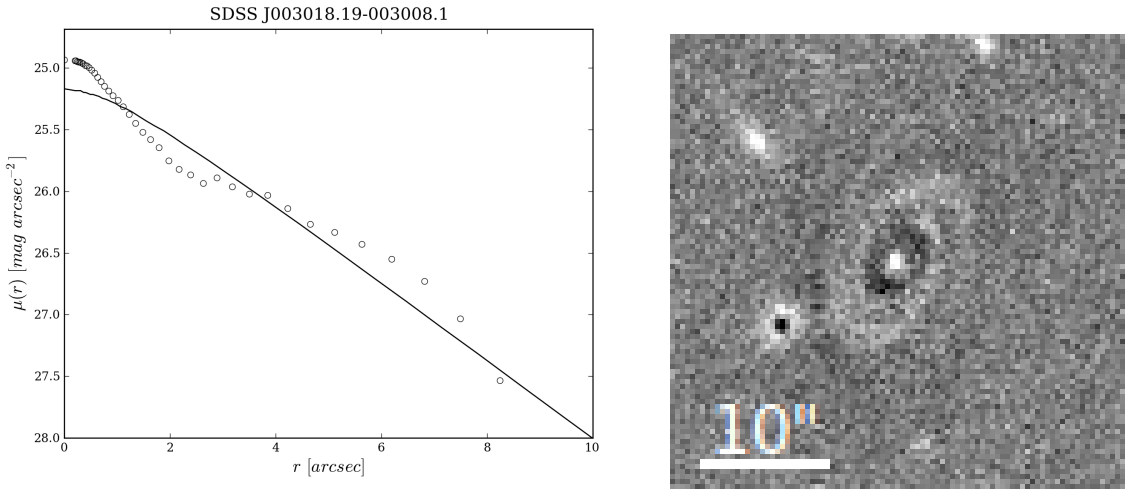

Figure 3.7: Surface brightness profile (left) and residual image from GALFIT (right) for galaxy SDSS J003018.19-003008.1. The solid line represents the exponential disk model and the open circles are the galaxy data. The scale of the residual image was set to *zscale* in ds9 so that the pixels around the median intensity of the image clearly stand out and we can have a better view of the distribution of the residuals. However they are actually quite faint. In this case the differences between the model and the actual profile reflect the spiral pattern of this galaxy.

by a Sérsic profile. I further stress that in the brightest central area of the galaxies such residuals are always below the 10% level.

Another key aspect to keep in mind when selecting the final model is that galaxies do not naturally fall into the single exponential disk category, i.e. some deviations from this analytical model should be expected and are reflected in the actual results. In other words, few galaxies are matched exactly by an exponential disk. One example is presented in Figure 3.7 where the spiral pattern produces a wobbly disk profile where the zones where the model counts are below the galaxy flux locate the spiral arms and the zones where the model counts are above the galaxy flux pinpoint the regions in-between arms. Asymmetrical features, ring-like features, inner disks, bars and spiral patterns, which are commonly observed in this sample, will affect the shape of the surface brightness profiles. Thus, the choice between a simple exponential disk model (hereafter model 1) and an exponential disk plus a n-free Sérsic model (hereafter model 2) is not trivial. My choice is based on the visual inspection and physical meaning of the parameters of the two models used (with both of them having $\Delta n/n < 15\%$). Whenever the difference between model 1 and 2 did not show significant improvement (mainly because one of the components would become too faint or its effective radius

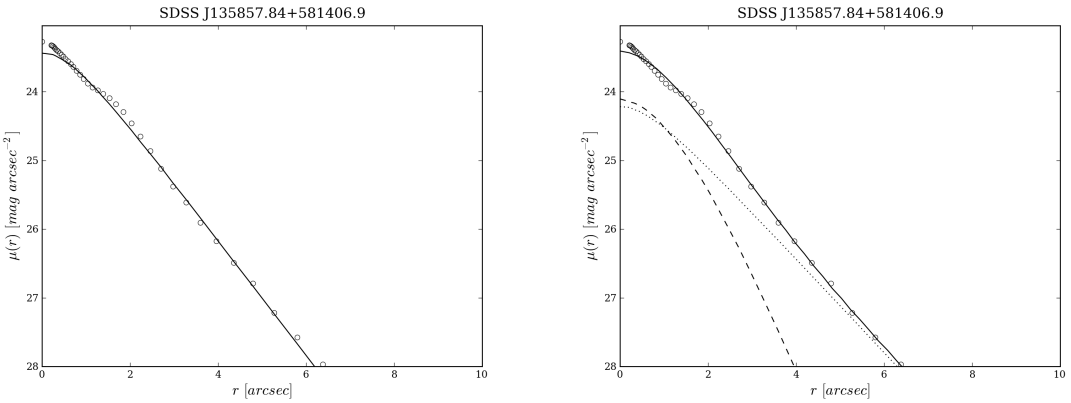

Figure 3.8: Surface brightness profiles of models 1 (left) and 2 (right) for SDSS J135857.84+581406.9. In this case the differences between models 1 and 2 are negligible.

was greater than that of the exponential disk) model 1 was chosen.

There are also the special cases (23 out of 67 galaxies) on which GALFIT could not converge for model 2, meaning that the residuals after exponential disk subtraction have no structure coherent with an extra Sérsic model. Of the other 44 galaxies, 15 show no considerable difference between model 1 and 2 (see Figure 3.8 for an example).

Finally, there are two particular cases in which an exponential disk plus a n-free Sérsic profile completely failed to model the galaxy.

SDSS J111554.17+204438.4 (see Figure 3.9) is better modeled by the combination of an exponential central component with a faint, low Sérsic index ($n = 0.12 \pm 0.01$) extended disk. It still remains on the sample because, despite having no exponential large scale disk component, its central region its far from being a classical bulge and so it falls into the category of a galaxy with a pseudo-bulge.

SDSS J170630.27+220003.9 (see Figure 3.10) has a double n-free Sérsic profiles to describe its structure with a bulge component having a value of $n = 1.97 \pm 0.18$. Despite being over the imposed $n < 1.5$ limit of the selection criteria, I chose to keep this galaxy in the sample because its n value still remains below 2.

I found a galaxy with a truncated profile, SDSS J131659.28+074326.4 (Figure 3.11). The break in the light profile is visible in the GALFIT output residuals just outside the spiral arms where a darker annular region stands out. Other galaxies present in the same field were also modeled by GALFIT and no similar features were found giving indication that this is a real feature of the galaxy light profile and not some artifact

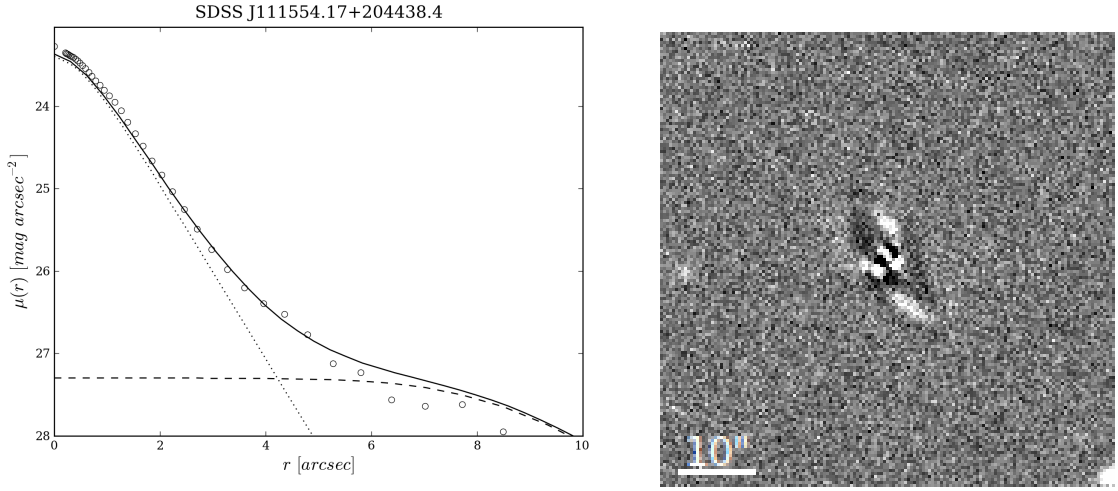

Figure 3.9: Same as Figure 3.10 but for SDSS J111554.17+204438.4. Here, the dotted line represents the exponential disk component, the dashed line the n-free Sérsic component, the solid line the sum of the two components and the open circles are the galaxy data

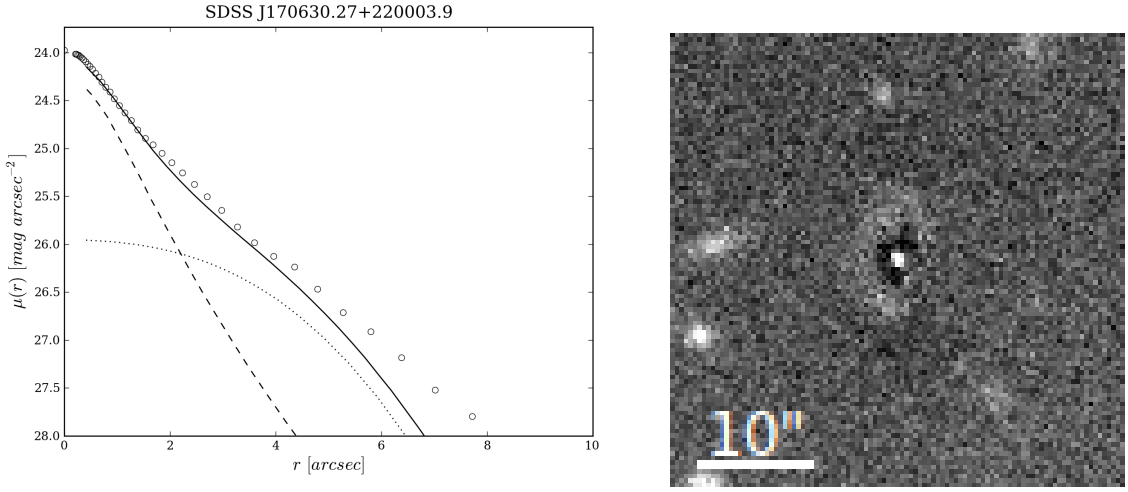

Figure 3.10: Same as Figure 3.9 but for SDSS J170630.27+220003.9. Here, the dotted line represents the n-free disk component, the dashed line the n-free bulge component.

of the original image nor is it due to the PSF model used.

Such breaks in the light profiles of spiral galaxies have been previously reported [59]. Using the Pohlen & Trujillo (2006) [51] classification scheme, this galaxy is a Type II - CT, i.e. a classically truncated downbending profile where a marked break in the light profile is seen outside the spiral arms region. This truncation occurs because the gas density falls below the required density to allow star-formation in these regions [43]. This break does not appear such evidently in all galaxies possibly due to the redistribution of stellar mass by secular processes [54].

Regarding its light profile (see Figure 3.11, left panel), it is important to stress that the presence of strong spiral arms compromises the concordance between the galaxy's and the model's surface brightness profiles. In addition to that issue there is an additional amount of light that corresponds to the center of the galaxy which GALFIT fails to model (a second Sérsic profile leads both the Sérsic index and the effective radius to unrealistic values - $n = 0.08 \pm 2.11$ and $r_e = 0.78 \pm 0.17$). The outer truncation of the galaxy's light profile has also an effect on the derived profile which is not so significant since it refers to low counts pixels. The n-free Sérsic profile (with $n = 1.21 \pm 0.02$) does not improve greatly the overall profile (see Figure 3.12) and has the same problems of convergence as state above.

The excess of light concentrated in the center of the galaxy revealed in the residuals, also observed in other galaxies, suggests that other central component (e.g. AGN type) may co-exist.

For the bulgy control sample only an n-free Sérsic profile was needed to correctly model each galaxy. The corresponding results are summarized in table 3.3. An example of this galaxy type is displayed in Figure 3.13. GALFIT results seem consistent with the selection criteria except for galaxies SDSSJ155933.09-010556.1 and SDSSJ112805.92+000755.9 which present $n < 4$ but are still bulgy galaxies with $n = 3.68 \pm 0.06$ and $n = 3.34 \pm 0.07$ respectively.

Considering this, we arrive at a sample composed of 38 bulgeless galaxies, 29 pseudo-bulge galaxies and 20 bulgy galaxies.

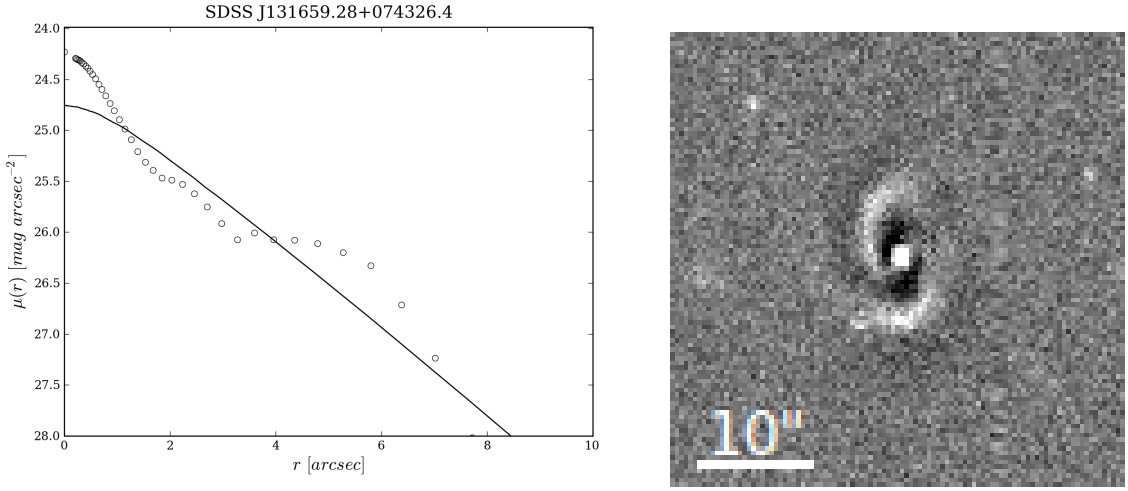

Figure 3.11: Same as Figure 3.7 but for galaxy SDSS J131659.28+074326.4. There is a slight overestimate of the model in the outer part of the galaxy which appears in the residuals image as a darker region surrounding the galaxy's spiral structure. The central structure is slightly larger than the PSF extent but GALFIT fails to converge in a solution for this case.

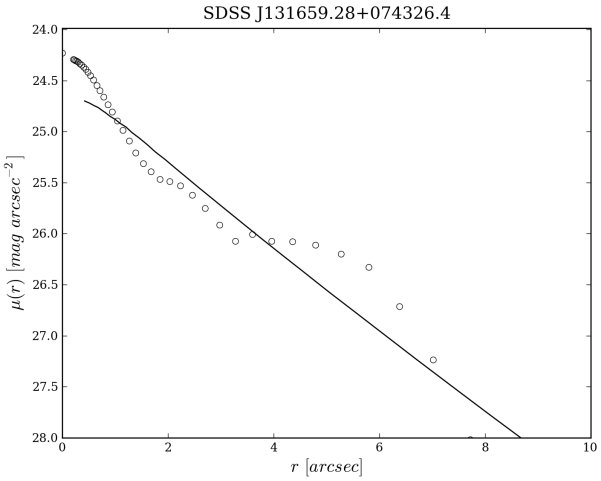

Figure 3.12: Same as Figure 3.11, left panel, but for the n-free Sérsic profile.

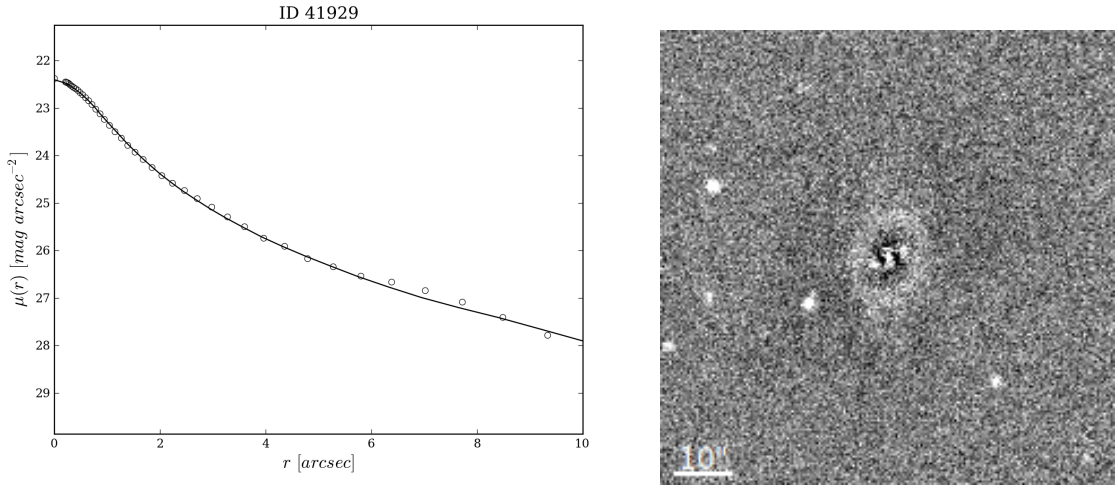

Figure 3.13: Same as Figure 3.7 but for galaxy SDSSJ140553.92-004443.5.

3.4 Comparison between galaxies with and without a significant bulge component

In this section I compare some of the parameters issued from GALFIT for the galaxies grouped according their structure.

First, the distinction between bulgeless and pseudo-bulge galaxies using only one Sérsic profile in one-dimensional fitting is not clear at all (see Figure 3.14). In addition, the finding of 4 galaxies modeled with $n > 4$ profiles by GALFIT stresses that contamination by bulgy galaxies is possible though probably minimal.

When looking at the histogram of axis ratio values (Figure 3.15), one can see that the bulgy galaxies have a more concentrated distribution at $b/a > 0.5$ while disks (referring to the bulgeless galaxies and to the exponential disk component for the galaxies with a pseudo-bulge) have a wider distribution with a peak at $b/a \sim 0.5$. The presence of values $b/a < 0.5$ (31 galaxies) indicates that the inclination parameter selection did not work correctly to retrieve galaxies compatible with the criterion used,for example , by [6]. The majority of the galaxies which fall below $b/a = 0.5$ are those modeled with two components (see Figure 3.16). Thus, a conclusion is that one-dimensional modeling of galaxies tends to overestimate the inclination parameter ($(b/a)_{1D}$ and especially q_{am}) for galaxies with more than one morphological component and q_{am} is, in fact, a poorer selection criteria for this sample. The other conclusion one may take from the data is that bulgy galaxies axis ratio is greater than those presented by the disks. This is expected and is due to the intrinsic shapes of galaxies with different

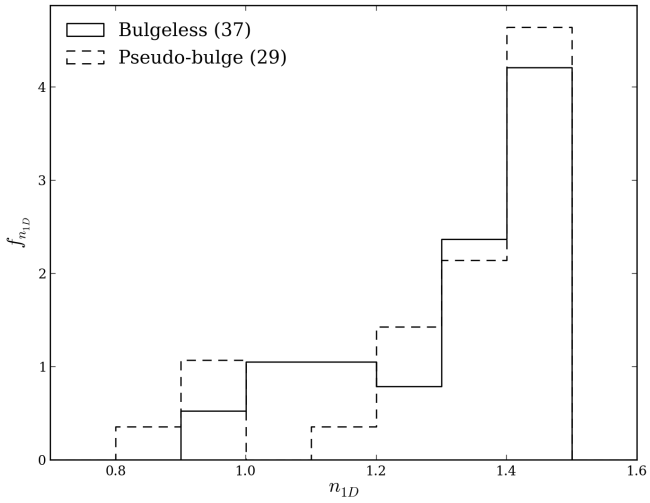

Figure 3.14: Normalized histogram of 1D Sérsic index values from NYU-VAGC for the bulgeless galaxies (solid line) and for the pseudo-bulge galaxies (dashed line).

morphologies. Because of the spheroidal like distribution characteristic of ellipsoids, the value of the axis ratio does not vary significantly with the inclination of the galaxy (i.e., if we rotate a perfect sphere in the sky its apparent axis ratio will always be 1 whereas for the case of a circular disk, the apparent axis ratio depends drastically on the inclination, and can assume extreme values - 1 for a face-on circular disk and ~ 0 for a edge-on circular disk).

There also seems to be a difference is size when we compare pure disk galaxies (bulgeless) and the exponential disks of the pseudo-bulge galaxies. From Figure 3.17 we can see that galaxies that require two components to correctly model their large-scale structure are in general larger than those that are modeled using a single component. This can mean that bulgeless galaxies are intrinsically smaller (since the same model with a fixed Sérsic index was used in both cases, greater effective radius means a greater extent). If so, it might also be that the smearing of the PSF of the images of these galaxies would not allow GALFIT to distinguish a second component in the smaller galaxies. But, if existing, would always be quite insignificant and unable to yield a change of classification (from bulgeless to pseudo-bulge galaxy). A fact that contributes to the observed difference in disk size is that whenever a second component is added, the exponential disk radius generally increases since the center pixels, that weigh more in the fitting, are adjusted by a separate component and thus the disk model, adjusting rather the fainter parts, extends its radius to better enclose the outer, fainter regions. This increase is larger when we consider the galaxies for which the best

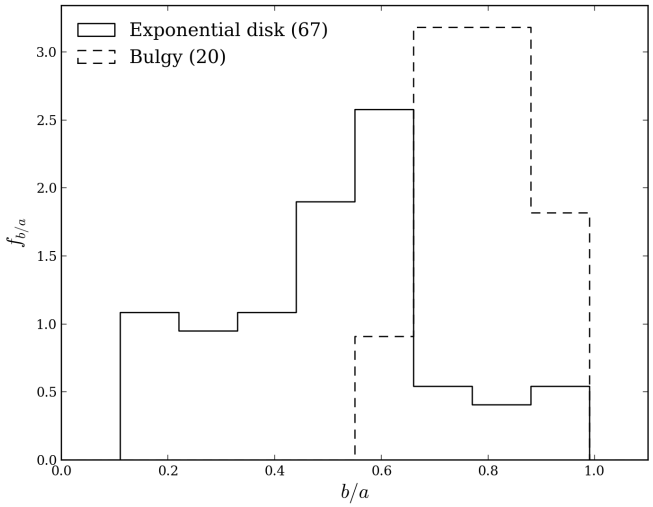

Figure 3.15: Normalized histogram of axis ratio values for the exponential disks (bulgeless + exponential disk components of pseudo-bulge galaxies) in my sample (solid line) and for the bulgy control sample (dashed line).

model is model 2 (pseudo-bulge galaxies): $< \delta r > \approx 3.7$ kpc for these galaxies against $< \delta r > \approx 1.5$ kpc for galaxies which are fit by model 1, but on which a second n-free Sérsic component is added as a test (thus applying model 2 to this class as well), where $\delta r = re_2 - re_1$ with re_2 being the effective radius of the exponential disk component of model 2 and re_1 the effective radius of the single exponential disk profile. This seems to indicate that the difference in size is indeed real.

It is interesting to note that this difference in size does is not accompanied by a corresponding difference in absolute magnitude (see Figure 3.18) meaning that the exponential disks of pseudo-bulge galaxies have lower surface brightness that the disks of bulgeless galaxies.

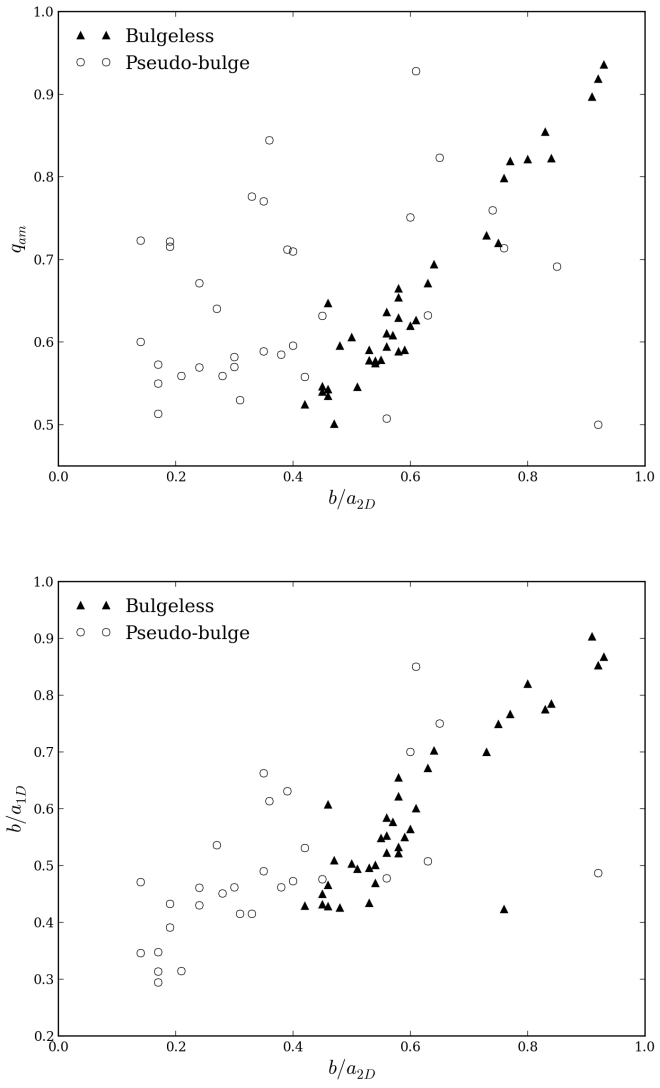

Figure 3.16: Comparison between the GALFIT based axis ratio and (1) the inclination parameter q_{am} (top panel): (2) the axis ratio from NYU-VAGC (bottom panel). Galaxies modeled with only one component are represented by triangles and the exponential disks of galaxies with two components are represented by open circles.

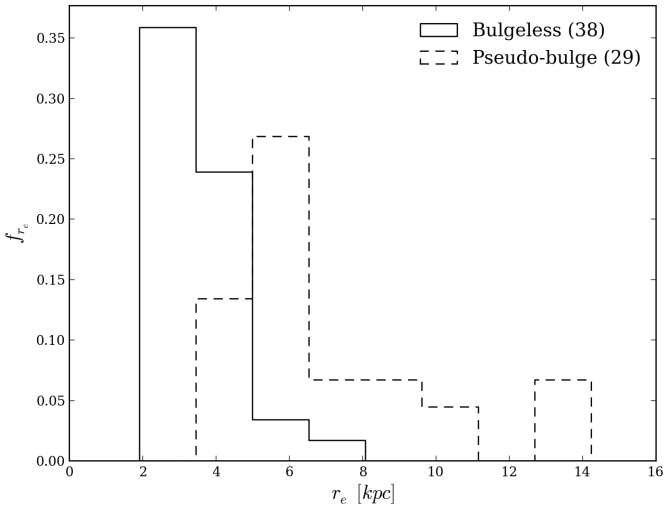

Figure 3.17: Normalized histogram of effective radius values for the bulgeless exponential disks (solid line) and for the exponential disks of pseudo-bulge galaxies (dashed line).

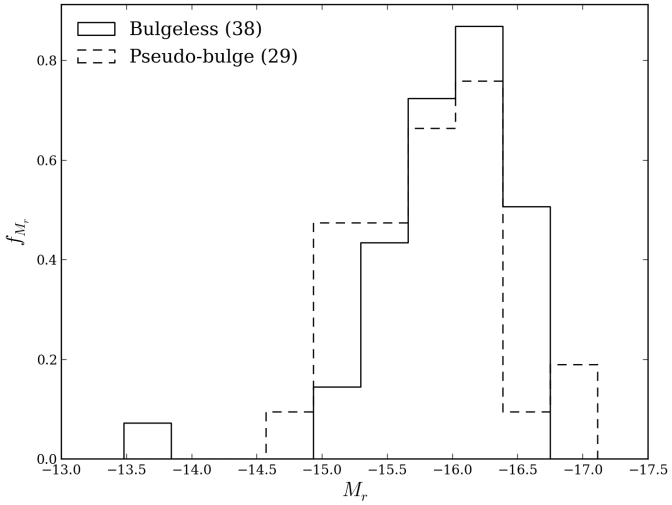

Figure 3.18: Normalized histogram of the absolute r-band magnitude for the bulgeless exponential disks (solid line) and for the exponential disks of pseudo-bulge galaxies (dashed line).

Table 3.2: Results of the structural analysis done with GALFIT for the 67 galaxies. (re_d) Effective radius of the single/disk component. (n_d) Sérsic index of the single/disk component. (b/a_d) Axis ration of the single /disk component. (re_b) Effective radius of the pseudo-bulge component. (n_b) Sérsic index of the pseudo-bulge component. (b/a_b) Axis ratio of the pseudo-bulge component.(χ^2_ν) Reduced χ^2 value of the fit.

Name	re_d [kpc]	n_d	b/a_d	re_b [kpc]	n_b	b/a_b	χ^2_ν
SDSS J003018.19-003008.1	6.32 ± 0.06	1.00	0.59 ± 0.005				1.039
SDSS J010303.55+132950.3	3.35 ± 0.02	1.00	0.58 ± 0.005				1.063
SDSS J011500.27+000151.3	5.22 ± 0.09	1.00	0.36 ± 0.005	0.96 ± 0.01	0.86 ± 0.02	0.90 ± 0.01	1.05
SDSS J011834.14-001341.7	5.90 ± 0.05	1.00	0.42 ± 0.005	1.38 ± 0.01	0.35 ± 0.01	0.57 ± 0.005	1.16
SDSS J014338.61+133139.6	14.12 ± 0.23	1.00	0.14 ± 0.005	1.62 ± 0.01	0.46 ± 0.02	0.96 ± 0.01	1.33
SDSS J020251.99-080136.1	5.98 ± 0.04	1.00	0.17 ± 0.005	1.11 ± 0.01	0.95 ± 0.01	0.82 ± 0.01	1.10
SDSS J033021.75+001547.1	4.14 ± 0.02	1.00	0.64 ± 0.005				1.185
SDSS J072403.09+404833.5	4.39 ± 0.06	1.00	0.84 ± 0.01				1.221
SDSS J075117.08+324425.1	5.16 ± 0.06	1.00	0.38 ± 0.005	1.39 ± 0.02	0.34 ± 0.04	0.76 ± 0.02	1.12
SDSS J080217.94+112535.0	2.00 ± 0.01	1.00	0.93 ± 0.01				1.085
SDSS J080441.34+454715.6	3.66 ± 0.02	1.00	0.73 ± 0.005				1.089
SDSS J082919.82+061744.8	2.97 ± 0.01	1.00	0.54 ± 0.005				1.247
SDSS J083639.67+471515.3	3.27 ± 0.03	1.00	0.46 ± 0.005				1.024
SDSS J084251.31+525530.0	6.22 ± 0.12	1.00	0.45 ± 0.005	1.70 ± 0.03	0.62 ± 0.04	0.70 ± 0.01	0.90
SDSS J084434.40+465214.0	7.68 ± 0.30	1.00	0.24 ± 0.01	2.13 ± 0.04	0.74 ± 0.02	0.61 ± 0.01	1.08
SDSS J085640.72+055235.4	3.93 ± 0.05	1.00	0.53 ± 0.01				1.033
SDSS J090222.84+143130.8	14.23 ± 0.15	1.00	0.28 ± 0.005	2.66 ± 0.01	0.82 ± 0.005	0.53 ± 0.005	1.42
SDSS J093159.95+512254.0	3.91 ± 0.07	1.00	0.65 ± 0.01	1.28 ± 0.03	1.09 ± 0.02	0.85 ± 0.01	1.01
SDSS J094058.94+400211.3	5.40 ± 0.06	1.00	0.19 ± 0.005	0.81 ± 0.01	0.33 ± 0.02	0.85 ± 0.01	1.05

Table 3.2 (continued)

Name	re_d [kpc]	n_d	b/a_d	re_b [kpc]	n_b	b/a_b	χ^2_ν
SDSS J094208.40+094355.5	3.26 ± 0.02	1.00	0.45 ± 0.005				1.096
SDSS J095146.53+273245.8	2.24 ± 0.01	1.00	0.83 ± 0.005				1.569
SDSS J095517.41+174114.7	2.47 ± 0.01	1.00	0.51 ± 0.005				1.171
SDSS J100441.71+282124.0	7.58 ± 0.06	1.00	0.21 ± 0.005	0.88 ± 0.01	0.54 ± 0.03	0.90 ± 0.01	1.05
SDSS J101422.68+182650.6	2.17 ± 0.01	1.00	0.61 ± 0.005				1.070
SDSS J102034.04+075106.5	5.47 ± 0.08	1.00	0.19 ± 0.005	1.04 ± 0.01	0.81 ± 0.02	0.90 ± 0.01	1.02
SDSS J103422.30+442349.1	2.09 ± 0.01	1.00	0.58 ± 0.005				1.098
SDSS J103543.35+121518.1	8.84 ± 0.15	1.00	0.30 ± 0.005	1.96 ± 0.02	0.73 ± 0.02	0.58 ± 0.005	1.03
SDSS J103856.94+254521.9	4.81 ± 0.05	1.00	0.80 ± 0.01				0.891
SDSS J103957.42+174019.5	4.05 ± 0.03	1.00	0.60 ± 0.005				1.266
SDSS J105153.17+085147.5	7.20 ± 0.12	1.00	0.39 ± 0.005	1.86 ± 0.03	0.80 ± 0.03	0.66 ± 0.01	1.37
SDSS J110313.24+074253.7	3.35 ± 0.02	1.00	0.77 ± 0.005				1.211
SDSS J110635.18+440248.7	2.25 ± 0.01	1.00	0.46 ± 0.005				2.066
SDSS J111554.17+204438.4	8.71 ± 0.10	0.12 ± 0.01	0.35 ± 0.005	1.97 ± 0.01	1.00	0.70 ± 0.005	1.21
SDSS J112723.89+193849.3	2.22 ± 0.01	1.00	0.42 ± 0.005				1.084
SDSS J113751.63+215827.1	12.86 ± 0.13	1.00	0.61 ± 0.005	1.71 ± 0.005	1.31 ± 0.005	0.93 ± 0.005	0.41
SDSS J115759.73+250931.4	2.00 ± 0.01	1.00	0.48 ± 0.005				1.021
SDSS J120547.65+335021.9	3.74 ± 0.05	1.00	0.46 ± 0.01				1.296
SDSS J123524.35+474120.6	4.58 ± 0.07	1.00	0.24 ± 0.005	0.92 ± 0.01	0.86 ± 0.02	0.92 ± 0.01	1.09
SDSS J125558.86+302149.2	4.28 ± 0.02	1.00	0.58 ± 0.005				1.333
SDSS J125830.33+634234.2	5.28 ± 0.08	1.00	0.17 ± 0.005	0.97 ± 0.01	0.62 ± 0.04	0.89 ± 0.01	1.45
SDSS J130643.54+093911.4	2.29 ± 0.01	1.00	0.92 ± 0.01				1.068

Table 3.2 (continued)

Name	re_d [kpc]	n_d	b/a_d	re_b [kpc]	n_b	b/a_b	χ^2_ν
SDSS J130830.79+503832.0	2.13 ± 0.005	1.00	0.56 ± 0.005				1.436
SDSS J131138.97+343811.2	5.35 ± 0.04	1.00	0.27 ± 0.01	5.49 ± 0.06	1.21 ± 0.01	0.92 ± 0.01	0.99
SDSS J131659.28+074326.4	4.07 ± 0.03	1.00	0.75 ± 0.005				1.222
SDSS J133600.37+063133.9	2.80 ± 0.01	1.00	0.63 ± 0.005				1.308
SDSS J133700.57+432532.1	7.24 ± 0.05	1.00	0.58 ± 0.005				1.058
SDSS J135857.84+581406.9	2.33 ± 0.01	1.00	0.91 ± 0.005				1.062
SDSS J140547.28+151138.3	3.17 ± 0.03	1.00	0.56 ± 0.005				1.085
SDSS J140929.47+000837.2	3.59 ± 0.02	1.00	0.57 ± 0.005				1.023
SDSS J141145.48-005415.4	9.93 ± 0.20	1.00	0.17 ± 0.005	1.79 ± 0.02	0.68 ± 0.02	0.77 ± 0.01	0.99
SDSS J144322.25+010553.2	4.53 ± 0.03	1.00	0.60 ± 0.005	1.54 ± 0.02	0.58 ± 0.02	0.59 ± 0.01	1.09
SDSS J144718.19+581333.3	3.64 ± 0.02	1.00	0.56 ± 0.005	1.70 ± 0.01	0.42 ± 0.02	0.22 ± 0.005	1.12
SDSS J145403.72+182401.5	5.12 ± 0.06	1.00	0.40 ± 0.005	1.65 ± 0.02	0.73 ± 0.03	0.55 ± 0.01	0.95
SDSS J152557.84+481744.8	4.42 ± 0.03	1.00	0.92 ± 0.01	2.22 ± 0.03	1.46 ± 0.03	0.20 ± 0.005	1.19
SDSS J153235.75+492302.8	2.89 ± 0.02	1.00	0.45 ± 0.005				1.217
SDSS J155153.04+271433.6	6.11 ± 0.09	1.00	0.35 ± 0.005	1.43 ± 0.01	0.42 ± 0.02	0.58 ± 0.01	1.49
SDSS J160813.06+440910.2	4.79 ± 0.04	1.00	0.56 ± 0.005				1.017
SDSS J161159.99+300251.8	5.30 ± 0.04	1.00	0.76 ± 0.005				0.766
SDSS J161705.55+112506.4	3.46 ± 0.01	1.00	0.55 ± 0.005				2.376
SDSS J163855.82+132327.0	3.83 ± 0.03	1.00	0.54 ± 0.005				1.311
SDSS J165529.67+232307.5	10.46 ± 0.07	1.00	0.33 ± 0.005	1.12 ± 0.02	0.70 ± 0.06	0.59 ± 0.01	0.99
SDSS J165741.87+335509.7	9.36 ± 0.18	1.00	0.14 ± 0.005	1.57 ± 0.02	1.01 ± 0.03	0.77 ± 0.01	1.95
SDSS J170630.27+220003.9	4.19 ± 0.08	0.37 ± 0.03	0.63 ± 0.01	1.75 ± 0.25	1.97 ± 0.18	0.47 ± 0.01	1.08

Table 3.2 (continued)

Name	re_d [kpc]	n_d	b/a_d	re_b [kpc]	n_b	b/a_b	χ^2_ν
SDSS J170714.43+652200.2	3.20 ± 0.02	1.00	0.50 ± 0.005				1.076
SDSS J170842.02+283118.1	4.61 ± 0.01	1.00	0.47 ± 0.005				1.210
SDSS J213058.11-070507.8	6.23 ± 0.04	1.00	0.31 ± 0.005	1.16 ± 0.01	0.74 ± 0.01	0.60 ± 0.005	1.78
SDSS J221917.33-011113.7	2.58 ± 0.03	1.00	0.53 ± 0.005				1.767

Table 3.3: Results of the structural analysis done with GALFIT for the bulgy control sample.

Name	re [kpc]	n	b/a	χ^2_ν
SDSS J034357.48+002616	4.16 ± 0.06	5.22 ± 0.06	0.55 ± 0.01	1.002
SDSS J035041.93+010226.7	3.62 ± 0.06	5.56 ± 0.06	0.80 ± 0.01	1.080
SDSS J101345.16-005238	4.67 ± 0.22	5.36 ± 0.14	0.93 ± 0.01	1.071
SDSS J112805.92+000755.9	1.75 ± 0.02	3.34 ± 0.07	0.72 ± 0.01	1.027
SDSS J113029.32+002939.4	6.26 ± 0.15	5.62 ± 0.07	0.82 ± 0.01	1.043
SDSS J121104.06+005820.2	22.11 ± 0.44	6.10 ± 0.04	0.92 ± 0.01	1.031
SDSS J124601.38-010423.5	3.64 ± 0.11	5.56 ± 0.11	0.88 ± 0.01	1.084
SDSS J133708+002707.6	3.83 ± 0.07	5.22 ± 0.06	0.96 ± 0.01	1.120
SDSS J140553.92-004443.5	4.44 ± 0.08	5.07 ± 0.07	0.69 ± 0.01	0.920
SDSS J142959.62+001201.2	2.20 ± 0.05	4.81 ± 0.10	0.89 ± 0.01	0.933
SDSS J145002.16+003443.5	4.99 ± 0.13	7.84 ± 0.10	0.86 ± 0.01	1.034
SDSS J145349.06+000522.7	3.60 ± 0.08	6.52 ± 0.09	0.76 ± 0.01	1.146
SDSS J150444.18-002107.1	7.30 ± 0.13	4.83 ± 0.05	0.70 ± 0.01	1.236
SDSS J155627.54+000333.3	4.58 ± 0.17	5.92 ± 0.12	0.64 ± 0.01	1.015
SDSS J155933.09-010556.1	2.72 ± 0.05	3.68 ± 0.06	0.71 ± 0.01	1.030
SDSS J160453.4-000250.8	2.69 ± 0.06	4.80 ± 0.09	0.69 ± 0.01	0.926
SDSS J160553.82-003301.6	3.35 ± 0.07	5.05 ± 0.08	0.84 ± 0.01	1.100
SDSS J161220.57+004817.5	6.99 ± 0.33	6.16 ± 0.15	0.81 ± 0.01	1.108
SDSS J161757.04-002253.2	4.05 ± 0.15	6.41 ± 0.14	0.84 ± 0.01	0.820
SDSS J163019.13+0011060	3.29 ± 0.10	5.11 ± 0.13	0.76 ± 0.01	1.076

Chapter 4

Stellar content of central regions

The spectrum of a galaxy in the optical is composed of photons from every galactic component, mainly star light, which convey information about its general properties. The fraction of blue and red stars, the mass of stars needed to produce such output, the fraction of metals in those stars and many other properties can be deduced by a thorough study. And from that information we can gain insight about its past history such as star-formation or chemical evolution.

Turning an observed spectrum into a set of physical properties is not a trivial process. There are two different approaches to solve this problem. One relies on models that reproduce the evolution in time of a composite stellar system with combinations of a stellar evolution prescription with a stellar spectra library [9], the other uses empirical information of individual stars or chemically homogeneous groups of stars of different ages and tries to mimic the observed spectrum using a linear combination of those simpler systems [13].

During this thesis a collaboration was initiated with J. M. Gomes who applied the code STARLIGHT [1] [12] - a model of the second type - to the SDSS spectra of the galaxies in the samples analyzed in the previous chapter: galaxies with only disk, with pseudo-bulges and bulgy ones. This chapter summarizes the results from STARLIGT and the analysis that I performed on those results that aim at giving hints on the different properties and evolutionary path of the central regions of bulgeless and pseudo-bulge galaxies and to compare to those of bulgy galaxies.

Note that all quantities derived from STARLIGHT refer only to the central 3" of the

[1] http://www.starlight.ufsc.br/

galaxy (ranging from 1.20 kpc for the closer sources to 3.43 kpc for the farther ones).

4.1 STARLIGHT

The basic performance of STARLIGHT is to fit an observed spectrum, O_λ, with a linear combination of $N_\star$ simple stellar populations (SSP) from evolutionary synthesis models. In this work we used the Bruzual & Charlot (2003) [9] models. Extinction is modeled as due to intervening dust contained in the observed galaxy, and is parametrized by the V-band extinction, A_V, using the Galactic extinction law proposed by Cardelli, Clayton & Mathis (1989) [10] with $R_V \equiv A_V/E(B-V) = 3.1$ (where E(B-V) is the color excess between the B-band and the V-band). Kinematic motions in the line of sight are modeled by a Gaussian function, G, centered at velocity $v_\star$ and with dispersion $\sigma_\star$. With these assumptions, the model spectrum is given by:

$$M_\lambda = M_{\lambda_0} \left(\sum_{i=1}^{N_\star} x_i b_{\lambda,i} r_\lambda \right) \otimes G(v_\star, \sigma_\star) \tag{4.1}$$

where M_{λ_0} is the synthetic flux at the normalization wavelength $\lambda_0 = 4020$ Å(in this work), x_i is the fractional contribution of the SSP with age t_i and metallicity Z_i to the model flux at λ_0, $b_{\lambda,i}$ is the spectrum of the ith SSP normalized at λ_0, $\log_{10} r_\lambda \equiv -0.4(A_\lambda - A_{\lambda_0})$ is the term for extinction and $\otimes$ is the convolution operator. The base component x_i can also be denoted by its mass fraction μ_i.

The best fit is chosen by minimizing the χ^2, defined as:

$$\chi^2 = \sum_\lambda [(O_\lambda - M_\lambda)\omega_\lambda]^2 \tag{4.2}$$

where ω_λ is the inverse of the error of the observed spectrum at λ. This definition becomes useful to mask out regions around emission lines, bad pixels and sky residuals by simply setting $\omega_\lambda = 0$.

For this study the code ran with a library composed of 25 stellar ages ranging from 10^6 to 1.8×10^{10} years and with six different metallicities - $Z_i = \{0.0001, 0.0004, 0.004, 0.008, 0.02, 0.05\}$ with $Z_\odot = 0.02$. This generates a total of $N_\star = 150$ different stellar populations from which the synthetic spectra will be constructed.

4.2 Inferred physical properties

From the fitted spectrum (see Figure 4.1 for two examples) one can infer some physical properties of the underlying stellar population of the galaxies. Some of these properties are rather straightforward to obtain since they play a role in the process of finding the best combination to reproduce the observed spectrum. Extinction and velocity dispersion are parameters directly retrieved from the best model. Stellar mass is not explicitly given but is calculated using the mass fraction, μ, of all components combined with the mass-to-light ratio ($M_\star/L_{\lambda_0}$) characteristic of each SSP.

To better quantify the stellar content of the observed regions, the SSPs have been divided in three groups according to their age,

- Young population stars with ages $t_\star < 9 \times 10^7$ years;
- Intermediate population stars with $9 \times 10^7 < t_\star < 10^9$ years;
- Old population stars with $t_\star > 10^9$ years;

From this, one can construct six quantities (light fraction and mass fraction of the three defined populations) which quantify the contribution of stars with different ages to the observed spectrum.

The mean stellar age is computed as a linear combination of the different SSP's ages causing the final result to be in the range of ages provided by the library. The light-weighted age is given by

$$\log\langle t_\star\rangle_L = \sum_{i=1}^{N_\star} x_i \log t_i \tag{4.3}$$

or alternatively, the mass-weighted age,

$$\log\langle t_\star\rangle_M = \sum_{i=1}^{N_\star} \mu_i \log t_i \tag{4.4}$$

The light-weighted stellar age is affected by any recent star-formation history, as young, blue stars emit strongly in the blue optical part and that will bias the mean age towards lower values. On the other and, the mass-weighted stellar age is biased towards higher mean ages as the older stellar population contributes the most for the

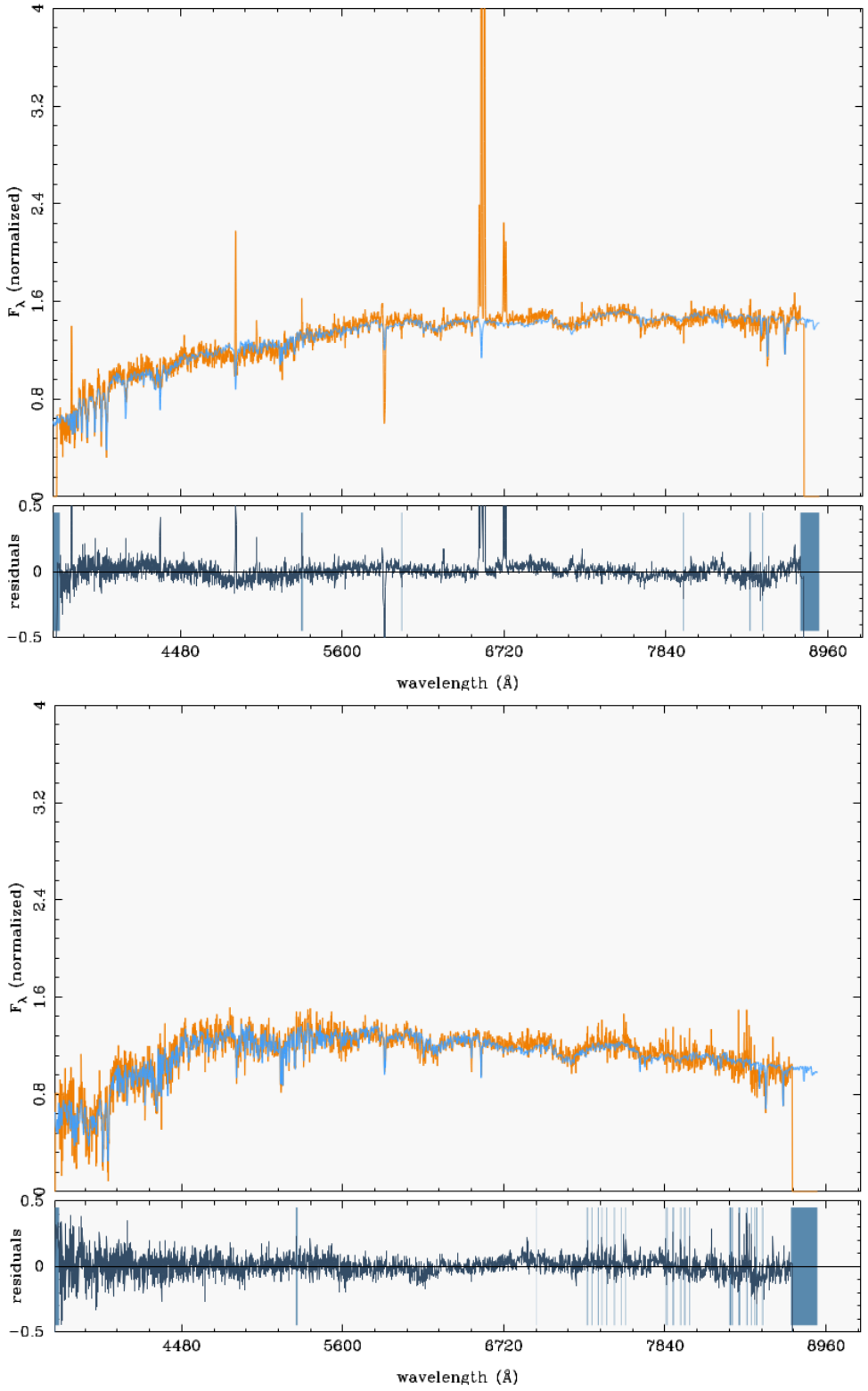

Figure 4.1: SDSS spectra (orange) and STARLIGHT fit (blue) for galaxies SDSS J082919.82+061744.8 (top) and SDSS J130643.54+093911.4 (bottom). The residuals are shown in the lower panel of each figure. The shadowed regions in the residuals are the masked regions, excluded from the fit. Figures provided by J. M. Gomes.

total mass. We assumed the light-weighted mean stellar age as the fit of the spectra was done in light, which is more robust as reflects the properties of the data.

In a similar way one can derive the stellar metallicity (the metal abundance of the stars, Z, defined as the mass fraction of all elements heavier than Helium), from the combination of the different SSP's metallicities. Again there are two different possibilities, light-weighted and mass-weighted, and again, the first one is used in this study and is defined as:

$$\langle Z_\star \rangle = \sum_{i=1}^{N_\star} x_i Z_i \tag{4.5}$$

The mean values for different properties can now be used to study differences between different groups of galaxies and explore some correlations between the parameters.

4.3 Results

In the next few paragraphs I will summarize the results issued from STARLIGHT which will be later discussed in chapter 5.

Stellar Mass

One interesting fact that comes out of the distribution of stellar mass for the different samples (see Figure 4.2) is that pseudo-bulge galaxies statistically have larger central masses than that of bulgeless galaxies and both of them tend to have lower stellar masses than the bulgy ones. I.e. , there is a dependence of the central stellar mass on the morphology of the host galaxy. Quantitatively, the bulgeless galaxies have values in the range $9.13 < \log(M_\star/M_\odot) < 10.48$ with a mean value of $10^{9.92} M_\odot$; pseudo-bulge galaxies range from $9.19 < \log(M_\star/M_\odot) < 10.64$ with a mean value of $10^{10.19} M_\odot$ and the bulgy galaxies present values in the interval $9.89 < \log(M_\star/M_\odot) < 10.67$ with a mean value of $10^{10.34} M_\odot$.

Stellar populations' mean age

In what concerns the mean stellar population age of the central region (see Figure 4.3), the pseudo-bulge galaxies have a wider distribution of mean stellar age (in the range $7.98 < \log\langle t_\star \rangle < 9.86$ Gyrs) , peaking at a higher value (the mean value for the pseudo-bulge sample is $10^{9.19}$ Gyrs) when comparing with the bulgeless sample (in

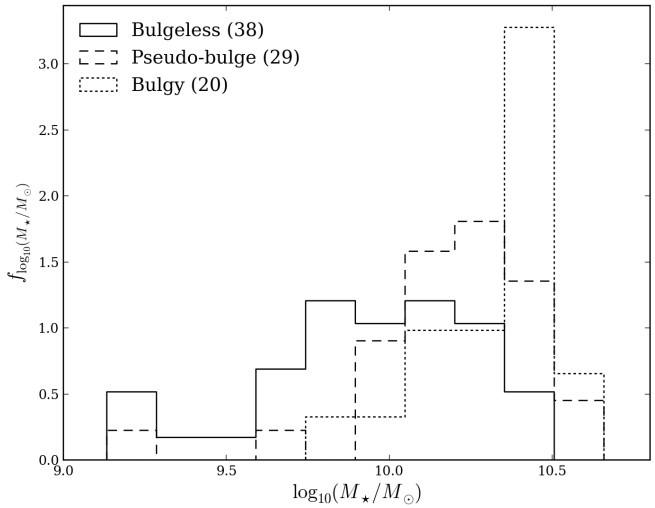

Figure 4.2: Normalized stellar mass histogram for the central regions of bulgeless (solid line), pseudo-bulge (dashed line) and bulgy (dotted line) galaxies.

the range $8.26 < \log\langle t_\star \rangle < 9.63$ Gyrs and with a mean value for the sample of $10^{9.06}$ Gyrs). The bulgy galaxies tend to be older and with small dispersion in the ages (in the range $9.26 < \log\langle t_\star \rangle < 9.93$ Gyrs and with a mean value for the sample of $10^{9.74}$ Gyrs).

Since the selection criterion limited galaxies to red colors it is natural that they present high values of mean stellar ages and that most of their stars formed at earlier epochs. When looking at the mass fraction of stars formed in the past 5 Gyrs (see Figure 4.4) it becomes clear that most of the stellar population observed in the bulgy galaxies were formed before that, at earlier stages of the universe: they have older stellar populations. As for bulgeless galaxies they tend to have higher mass fractions of stars formed in that time relatively to that of the pseudo-bulge galaxies.

Recent episodes of star formation in two galaxies explain the lower bin (in Figure 4.3) of the pseudo-bulge galaxies observed in the mean stellar age distribution. SDSS J152557.84+481744.8 and SDSS J131138.97+343811.2 with a mean stellar age of $\langle t_\star \rangle = 10^{8.08}, 10^{7.99}$ Gyrs respectively, have the highest observed mass fraction of stars formed in the past 100 Myrs of all galaxies in the sample (2.0% and 0.8%, respectively) .

Metal content

As for the metallicity of the stars in the central part of the galaxies (see Figure 4.5,

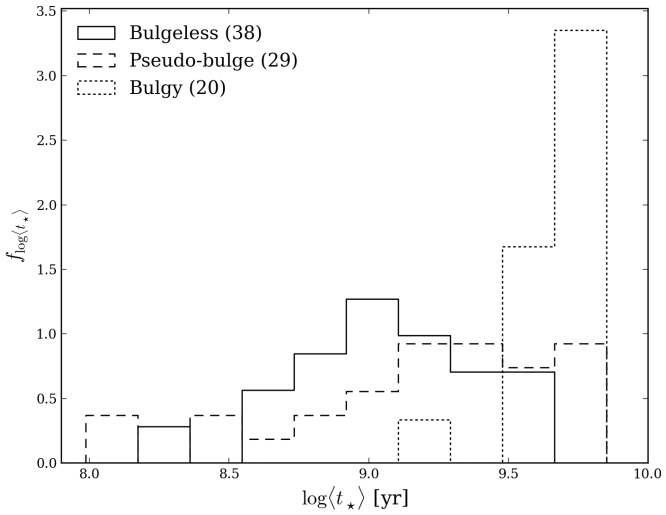

Figure 4.3: Normalized age histogram for the stellar population of the central regions of bulgeless (solid line), pseudo-bulge (dashed line) and bulgy (dotted line) galaxies.

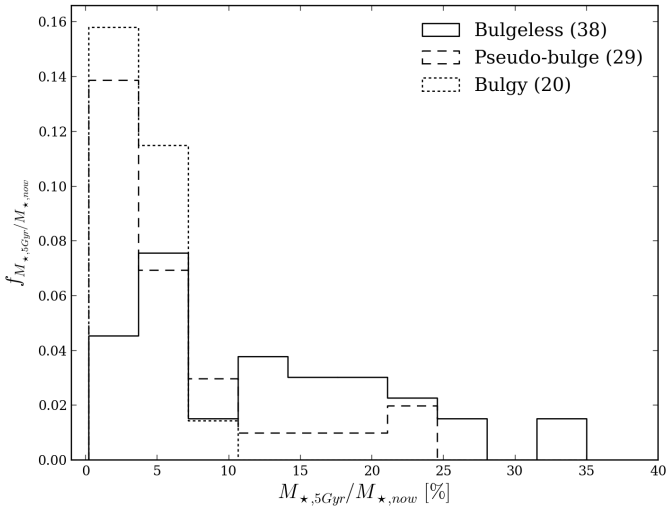

Figure 4.4: Normalized histogram of the mass fraction of stars formed in the past 5 Gyr,$M_{\star,5Gyr}$, compared with the current stellar mass, $M_{\star,now}$, for the central regions of bulgeless (solid line), pseudo-bulge (dashed line) and bulgy (dotted line) galaxies.

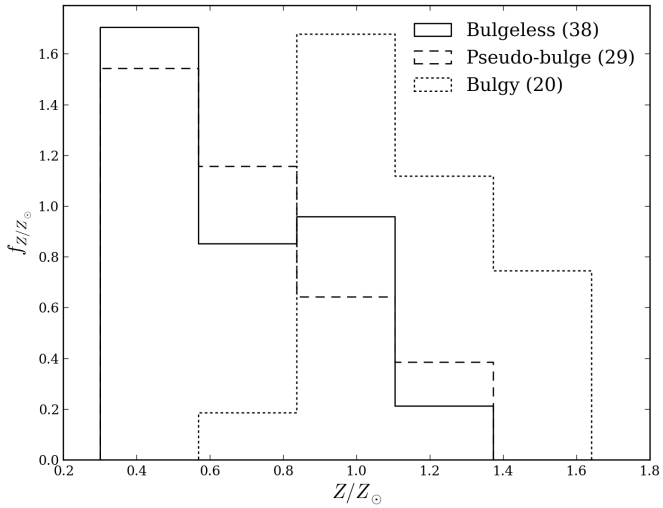

Figure 4.5: Normalized histogram of the metal fraction of the stars in the central regions of bulgeless (solid line), pseudo-bulge (dashed line) and bulgy (dotted line) galaxies.

there is not much of a difference when considering bulgeless and pseudo-bulge galaxies. But the metal content of the stars of central regions of bulgy galaxies is larger. This yields a distribution for the bulgeless galaxies in the interval $0.21 < Z/Z_\odot < 1.15$ with a mean value of $0.64Z_\odot$; the pseudo-bulge galaxies in the range $0.30 < Z/Z_\odot < 1.20$ with a mean value of $0.68Z_\odot$ and the bulgy galaxies have values in the range $0.68 < Z/Z_\odot < 1.64$ with a mean value of $1.17Z_\odot$.

It is important to note that the metallicity derived from STARLIGHT is related to all elements heavier than Helium. Iron, a common indicator of the metallicity, is released to the interstellar medium by type Ia supernovae (destruction of white dwarfs that exceed a mass limit when accreting mass from their binary companions [11, Section 18.5]) which usually explode at ages of 1Gyr or more, the more common Type IIa supernovae (that occur at the time of core collapse of red supergiant stars [11, Section 15.3]) reach these stages in 100Myr or less enriching the interstellar medium more rapidly with elements like oxygen or carbon [56, Section 6.3].

Velocity dispersion

In what regards the velocity dispersion of the central regions of the galaxies (see Figure 4.6, the three classes present distinct behaviors. As the bulge significance grows, so does the velocity dispersion, i.e. bulgeless galaxies have lower velocity dispersions than pseudo-bulge galaxies which, in turn, present lower values than the bulgy galaxies.

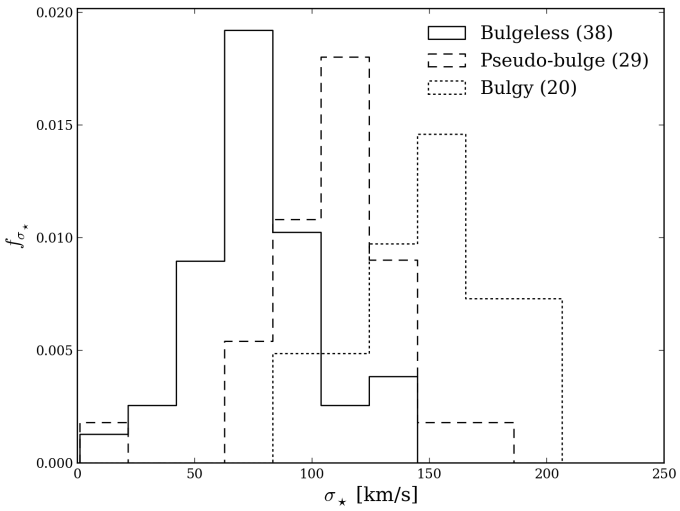

Figure 4.6: Normalized histogram for the velocity dispersion of central regions of the bulgeless (solid line), pseudo-bulge (dashed line) and bulgy (dotted line) galaxies.

This separation is a consequence of the mass difference for the three classes (see Figure 4.7) as galaxies with higher central stellar mass tend to have higher velocity dispersion values. The mean values of the three distributions are 77, 118 and 151 km/s for the bulgeless, pseudo-bulge and bulgy galaxies respectively.

Extinction

Since the extinction is related to the column density of dust, one expects that the higher the value of the extinction the higher the dust content of the galaxy (since the SDSS spectra were previously corrected for the extinction of our galaxy). As expected (see figure 4.8), bulgy galaxies show minimal values for the intrinsic extinction, reflecting the lower dust content in that class of galaxies, and bulgeless and pseudo-bulge galaxies show typical values substantially larger for this parameter. The observed range for the values of A_V is the same for the bulgeless and pseudo-bulge galaxies and present mean values of 0.66 and 0.76, respectively.

It is important to note that the inclination parameter, q_{am}, used in the selection of our sample does not work well on pseudo-bulge galaxies (see Figure 3.16). The inclusion of some inclined pseudo-bulge galaxies might bias their distribution of A_V towards higher values (as stated in chapter 2 edge-on galaxies have higher column densities of dust). If that is the case, the extinction distribution of bulgeless and pseudo-bulge galaxies may become distinguishable, if one introduces an inclination correction.

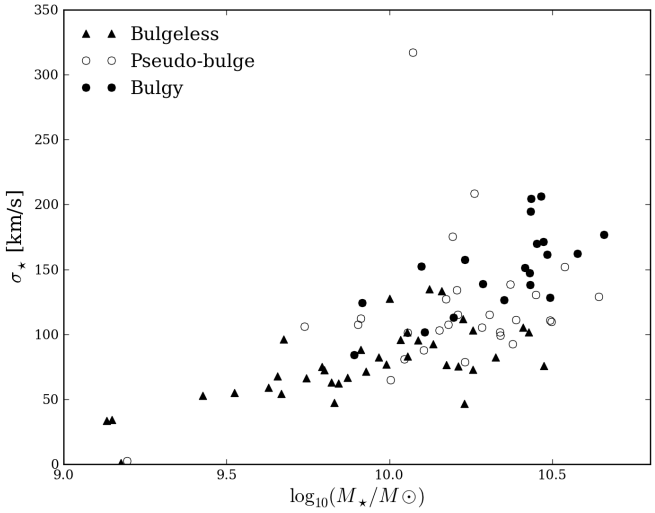

Figure 4.7: Stellar mass and velocity dispersion for the central regions of the galaxies in the sample. Bulgeless - triangles, pseudo-bulge - open circles, bulgy - filled circles.

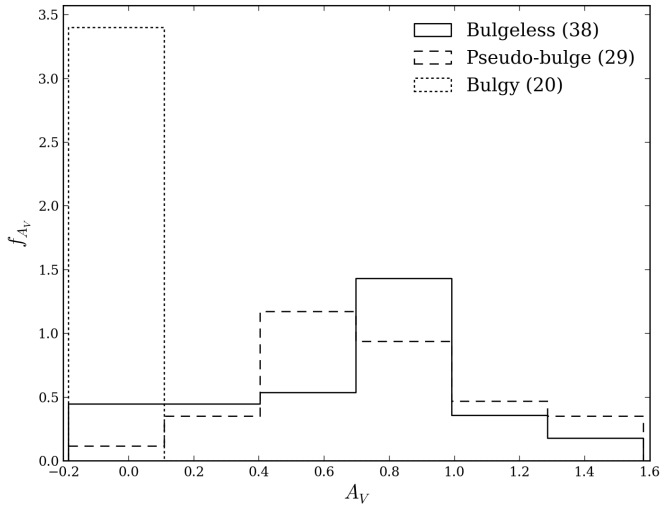

Figure 4.8: Normalized histogram for the V-band extinction of the central regions of bulgeless (solid line), pseudo-bulge (dashed line) and bulgy (dotted line) galaxies.

Chapter 5

Summary, Discussion & Conclusions

From an original sample of 77 galaxies issued from the SDSS DR7 through a particular selection scheme I performed a case-by-case structural analysis using GALFIT. 67 galaxies were retained based on their structural properties, and divided in two groups: 38 bulgeless galaxies and 29 pseudo-bulge galaxies. An additional set of 20 bulgy galaxies was also selected to be analyzed in the same way and thus serve as a control sample.

The results from a fit to the observed SDSS optical spectrum done with the STARLIGHT spectral synthesis code were further used. These consisted in parameters describing some physical properties such as mean stellar age, stellar mass, metallicity, dust extinction and velocity dispersion issued from the central 3 arcseconds of each galaxy. Then I established comparisons between the derived structure of the galaxies and the parameters computed by STARLIGHT to look for hints on the evolution scenarios for the central regions of these galaxies.

5.1 Discussion & Conclusions

In the aftermath of this work one may conclude that:

- Distinction between bulgeless and pseudo-bulge galaxies is not trivial but two-dimensional structural modeling of galaxies images yields better, more robust, results than fitting of their 1-D surface brightness profiles.

- One simple Sérsic profile, when applied on the 1-D surface brightness profile, does not allow us to clearly distinguish between bulgeless and pseudo-bulge galaxies.

- The inclination parameter, q_{am}, is not a good probe for galaxy inclination and $(b/a)_{1D}$ is slightly overestimated when considering pseudo-bulge galaxies.

- The exponential disks of pseudo-bulge galaxies seem to be larger than those of bulgeless galaxies despite having similar absolute magnitudes which indicates a lower surface brightness for the first ones.

- Bulgy galaxies have different physical properties in the central regions when compared with bulgeless and pseudo-bulge galaxies, having higher stellar masses and higher velocity dispersions, having higher mean metallicities and older mean stellar ages and finally by showing almost no star formation in the past 5Gyrs and displaying lower values for dust extinction.

- Pseudo-bulge galaxies have higher central stellar masses, higher central velocity dispersions, slightly older mean stellar population ages and lower mass fractions of stars formed in the past 5 Gyrs when compared to the bulgeless sample galaxies. As for metallicity and extinction both these two populations show similar results.

Regarding the stellar masses of the central regions of these galaxies one could say that the observed trends are a consequence of the distribution of the mass, as galaxies with a bulge component have their mass more concentrated than bulgeless ones and so, when analyzing this result, one only sees the effect of that concentration. The higher central stellar mass of bulgy galaxies is reasonably explained by mass concentration alone. However, pseudo-bulge galaxies have their disks more extended than the disks of bulgeless galaxies, implying a lower surface brightness of the disk. Assuming that pseudo-bulges are the result of the build up of the central mass on a bulgeless galaxy, either by secular evolution or merger processes, we may ask if the lower surface brightness is related to this build up of mass. If so, this scenario may favor the models of pseudo-bulge growth via satellite accretion. Numerical studies by Eliche-Moral et al. (2006) [23] and Aguerri et al. (2001) [2] show that these events lead to an increase of the disk scale length that depends on the mass of the satellite. This occurs due to the outward transport of disk material in the outer regions, combined with inward transport to the bulge in the inner regions.

The broadening of the observed spectral lines is due to random motions and/or a coherent rotation. Since our sample galaxies are close to face-on, even if rotation dominates in the observed regions, the contribution to this broadening should not

be significant, so we are mainly assessing the magnitude of stellar random motions. Additionally galaxies supported by rotation (disks) tend to have smaller values of thus velocity dispersion than galaxies supported by random motion (ellipticals) [7]. And bulges were found to correlate well with elliptical galaxies as the motion of their stars are mainly random. Thus, as bulges components grow so does the central stellar mass and the corresponding velocity dispersion.

The difference in metallicity may be explained also by the observed mass difference as a possible explanation is that since bulgy galaxies in this sample are typically more massive than the disk-dominated galaxies, their gravitational potential should be more effective in retaining the metals expelled in the explosions of Supernovae. These metals thus remain available in the surrounding inter stellar medium to enrich the next (local) generation of stars. If so, even though bulgy galaxies present older stellar populations in average, their mean metallicity can be larger because a significant fraction of their stars incorporated metals that in shallower potentials would have been lost to the disk, halo or even removed from the galaxy. Another possibility is related to the typical environments in which these galaxies have evolved. Works have shown that the metallicity of the galaxies is higher in denser regions when compared to that of the same morphological type but located in low density regions [24] due to tidally triggered star-formation (that enriches more rapidly the inter stellar medium of the galaxies involved). And bulge-dominated galaxies are more characteristic of dense environments such as cluster whereas disk-dominated galaxies tend to live in the field or in the outer regions of clusters [48].

As for the results concerning the observed mean stellar age, taken together with the values obtained for the mass fraction of stars formed in the last 5 Gyrs, the distributions presented in chapter 4 seem to favor the hypothesis that massive bulges form essentially through major merger processes [63] while minor mergers and accretion of satellites are an alternative preferable explanation to the secular formation of pseudo-bulges [47, Chapter 13]. As for bulgeless galaxies, my results on this parameters seem to support an evolution that is thought to be rather dominated by secular processes (since mergers, even from small satellites, cause a build up of the central mass [23]).

The distributions for bulgy galaxies could be explained if major merger processes (or even minor dry mergers) occurred in the early stages of their evolution, depleting the galaxies of their gas and preventing further star formation (or by adding an old stellar population to the galaxy from the accreted satellite, at any time of the galaxy's life, in the case of dry mergers) leaving the galaxy with an old stellar population.

A slow, secular-like evolution scenario in the case of bulgeless galaxies would correspond to a star formation history more extended in time, maintaining significant levels of star formation recently, and a lower mean stellar age. The slightly different distributions observed for the pseudo-bulge galaxies might be explained by the occurrence of minor, gas-rich mergers at a given epoch that locally, and in a shor period of time, accelerated the star formation rate, contributing to the formation of the pseudo-bulge and leaving less gas for later stage star formation. However, the difference between bulgeless and pseudo-bulge stars is not so significant that allows us to distinguish between the two possible scenarios for the formation of pseudo-bulges. Moreover, we are dealing with small numbers so the observed trends can only give indications. If lower extinction values were observed in pseudo-bulges (see section 4.3), this could further favor the hypothesis of pseudo-bulge formation via minor mergers (in detriment of the hypothesis of formation over secular evolution), as this type of interactions can more likely deplete the galaxies of some of their gas and dust.

All this results seem to point to the formation of the pseudo-bulges of our sample via minor mergers though one cannot exclude the secular evolution hypothesis.

5.2 Future work

Following the purpose of the original study, [15], in the future, higher resolution spectroscopy would allow estimates of the masses of possible central super massive black holes which allow to test whether bulgeless galaxies have these objects in their centers and also to check if the properties of the pseudo-bulges correlate with the black hole mass as happens with classical bulges, contributing to the work of Kormendy et al. (2011) [40]. Additionally, spectroscopic information of the galactic disks of the pseudo-bulge galaxies would allow us to compare the stellar populations of the two components of the galaxy giving further hints on the possible formation scenario of the pseudo-bulge.

Appendix A

Excluded objects and bulgy sample

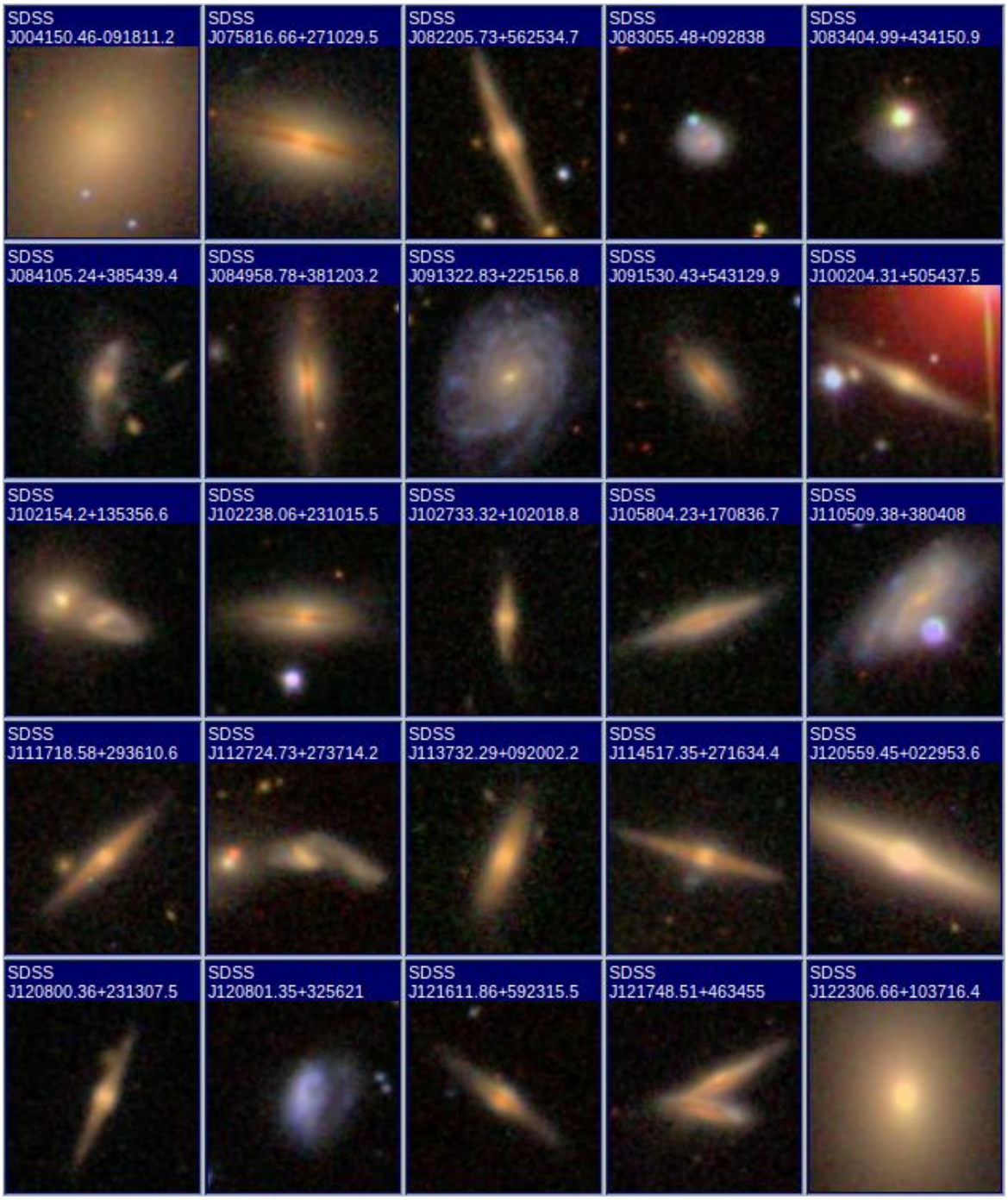

Figure A.1: Color (gri bands) images of the 36 galaxies excluded from the original sample.

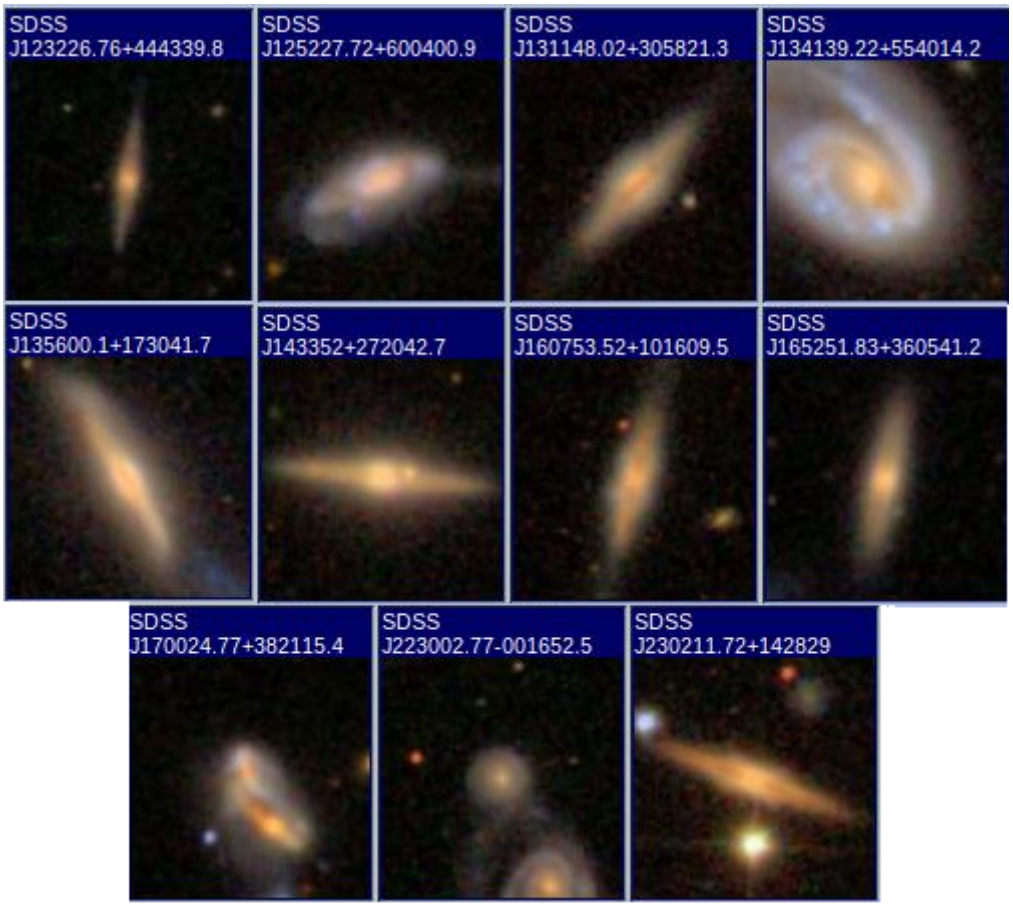

Color (gri bands) images of the 36 galaxies excluded from the original sample. (continued)

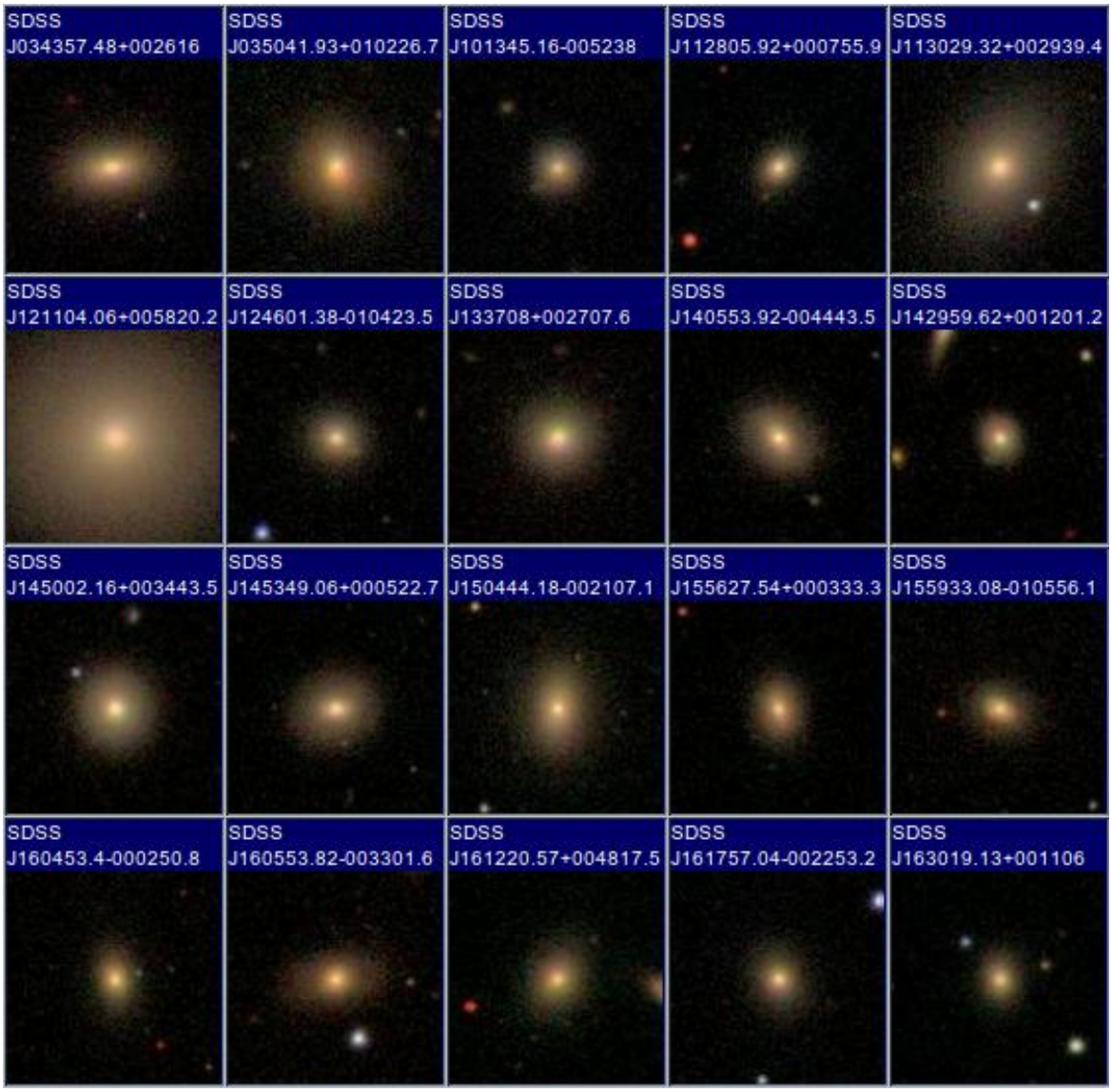

Figure A.2: Color (gri bands) images of the 20 bulgy galaxies.

Appendix B

GALFIT input file

```
================================================================================
# IMAGE and GALFIT CONTROL PARAMETERS
A) galaxy.fits         # Input data image (FITS file)
B) attempt_1.fits      # Output data image block
C) none                # Sigma image name (made from data if blank or "none")
D) psf_nosky.fits      #       # Input PSF image and (optional) diffusion kernel
E) 1                   # PSF fine sampling factor relative to data
F) none                # Bad pixel mask (FITS image or ASCII coord list)
G) none                # File with parameter constraints (ASCII file)
H) 1    101   1    101 # Image region to fit (xmin xmax ymin ymax)
I) 100    100          # Size of the convolution box (x y)
J) 28.3185087530691    # Magnitude photometric zeropoint
K) 0.396 0.396         # Plate scale (dx dy)   [arcsec per pixel]
O) regular             # Display type (regular, curses, both)
P) 0                   # Options: 0=normal run; 1,2=make model/imgblock & quit

# INITIAL FITTING PARAMETERS
#
#For object type, the allowed functions are:
#nuker, sersic, expdisk, devauc, king, psf, gaussian, moffat,
#ferrer, and sky.
#
#Hidden parameters will only appear when they're specified:
#C0 (diskyness/boxyness),
#Fn (n=integer, Azimuthal Fourier Modes).
#R0-R10 (PA rotation, for creating spiral structures).
#
# ------------------------------------------------------------------------------
#         par)    par value(s)    fit toggle(s)    parameter description
# ------------------------------------------------------------------------------

# Object number: 1
 0) sersic             # Object type
 1) 51.  51.     1 1  # position x, y        [pixel]
 3) 20.0000    1      # total magnitude
 4) 10.        1      #     R_e              [Pixels]
 5) 1.0000     0      # Sersic exponent (deVauc=4, expdisk=1)
 9) 0.5        1      # axis ratio (b/a)
10) 45.0       1      # position angle (PA)  [Degrees: Up=0, Left=90]
 Z) 0                 #  Skip this model in output image?  (yes=1, no=0)

# Object number: 2
 0) sky                #  object type
 1) 1151.0     1       #  sky background at center of fitting region [ADUs]
 2) 0.0000     0       #  dsky/dx (sky gradient in x)
 3) 0.0000     0       #  dsky/dy (sky gradient in y)
 Z) 0                  #  output option (0 = resid., 1 = Don't subtract)
```

Example input file for GALFIT for galaxy SDSS J010303.55+132950.3 with a Sérsic model with fixed Sérsic index $n = 1$ (exponential disk).

Appendix C

GALFIT residuals and surface brightness profiles

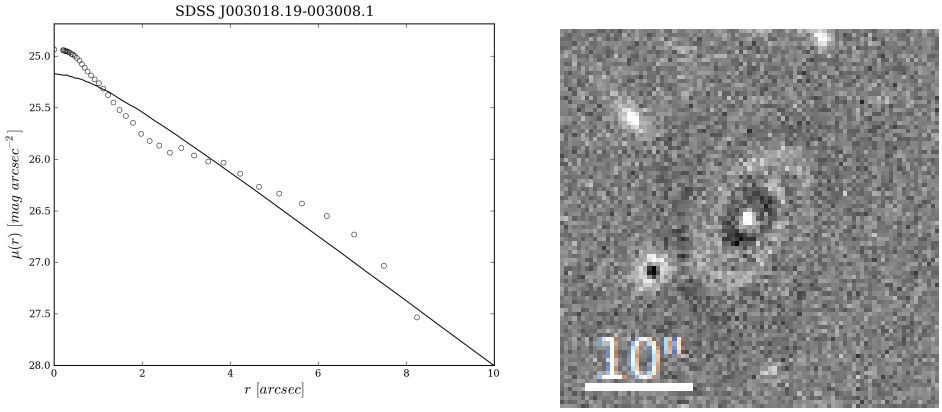

Same as Figure 3.7 but for galaxy SDSS J003018.19-003008.1.

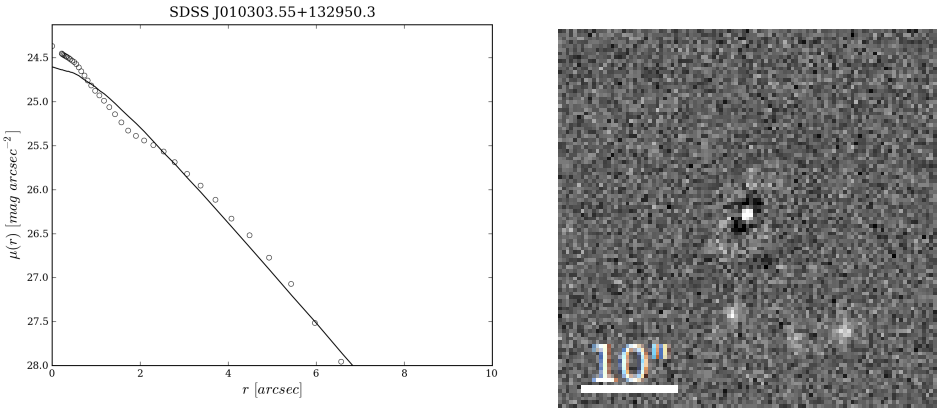

Same as Figure 3.7 but for galaxy SDSS J010303.55+132950.3.

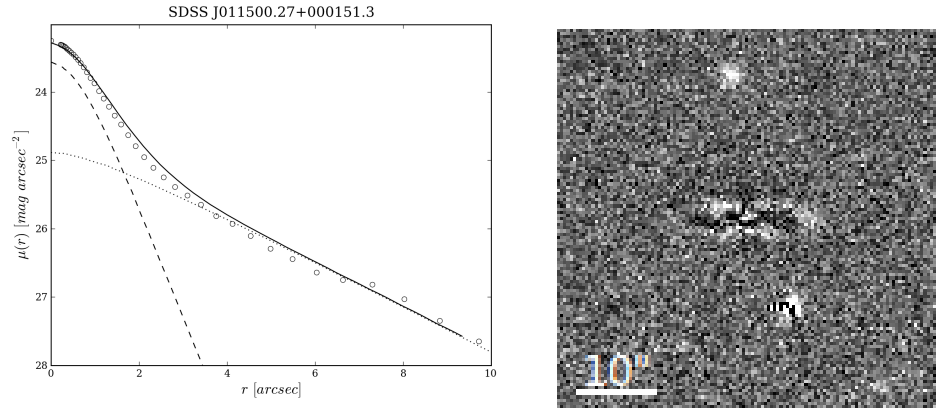

Same as Figure 3.9 but for galaxy SDSS J011500.27+000151.3.

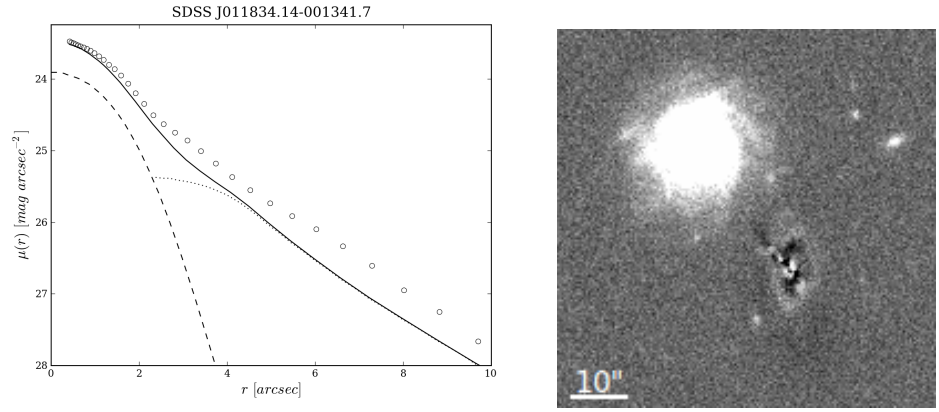

Same as Figure 3.9 but for galaxy SDSS J011834.14-001341.7.

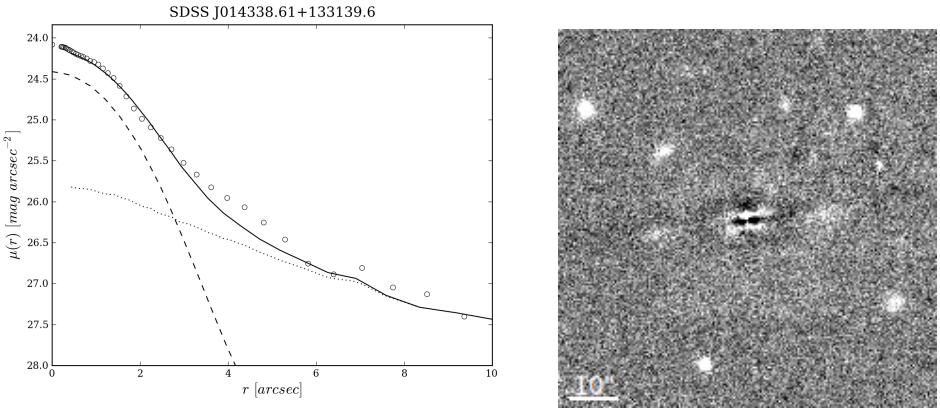

Same as Figure 3.9 but for galaxy SDSS J014338.61+133139.6.

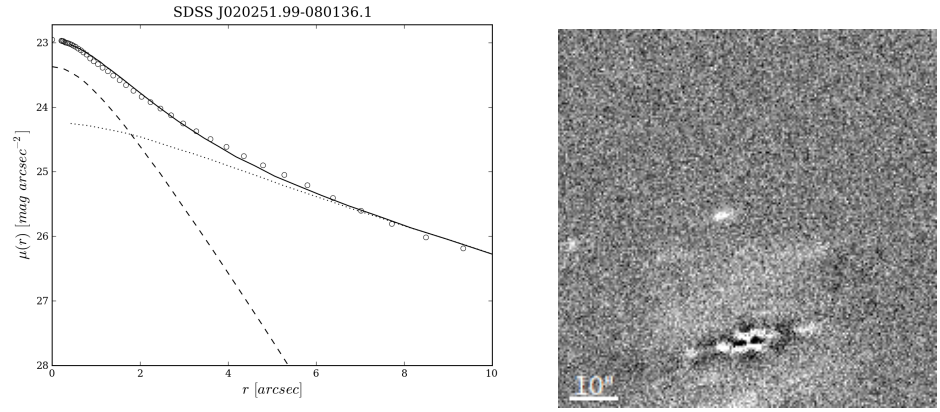

Same as Figure 3.9 but for galaxy SDSS J020251.99-080136.1.

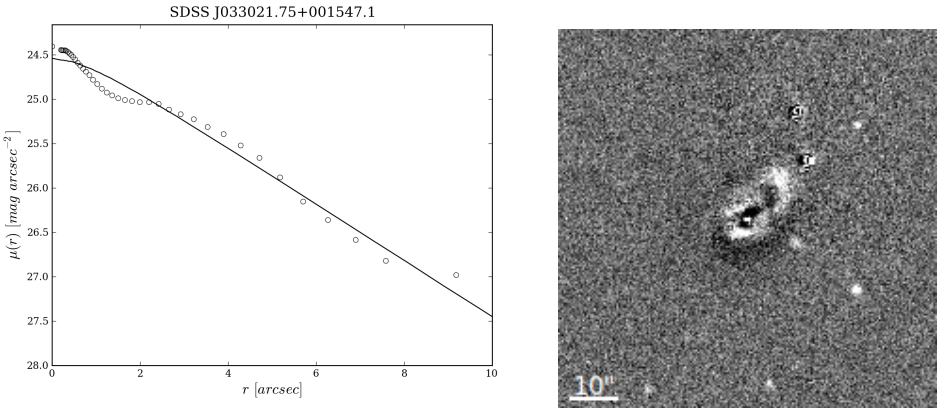

Same as Figure 3.7 but for galaxy SDSS J033021.75+001547.1.

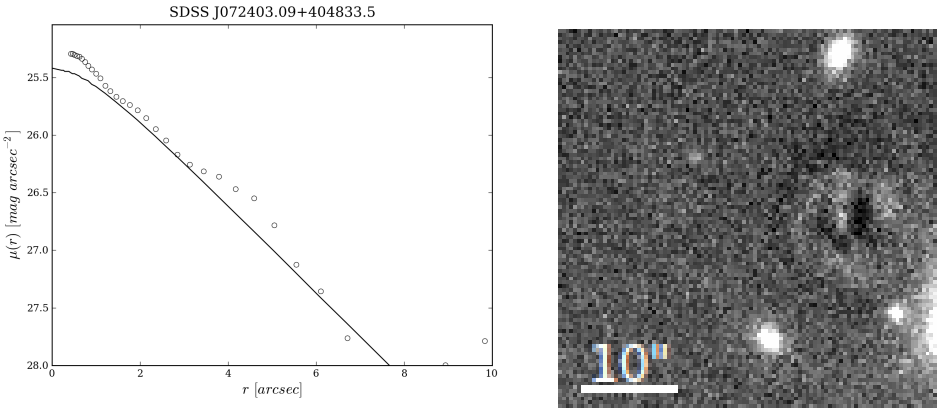

Same as Figure 3.7 but for galaxy SDSS J072403.09+404833.5.

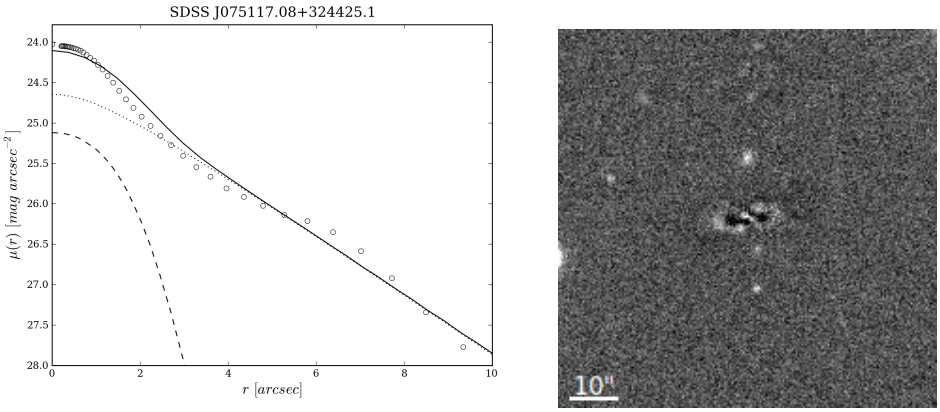

Same as Figure 3.9 but for galaxy SDSS J075117.08+324425.1.

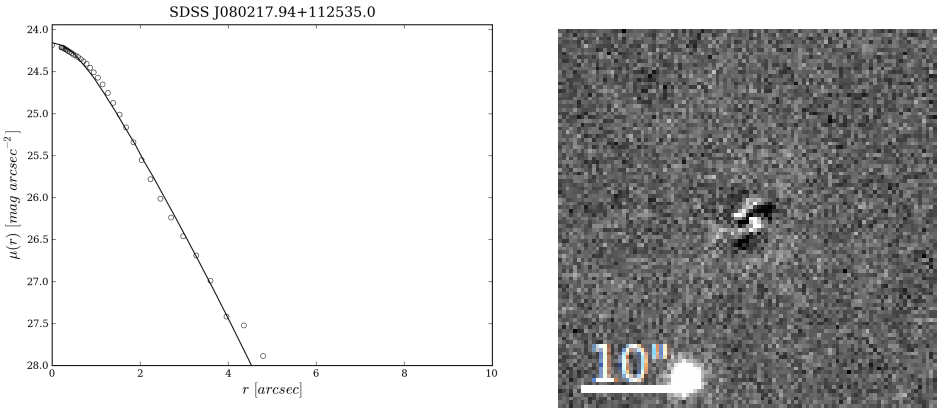

Same as Figure 3.7 but for galaxy SDSS J080217.94+112535.0.

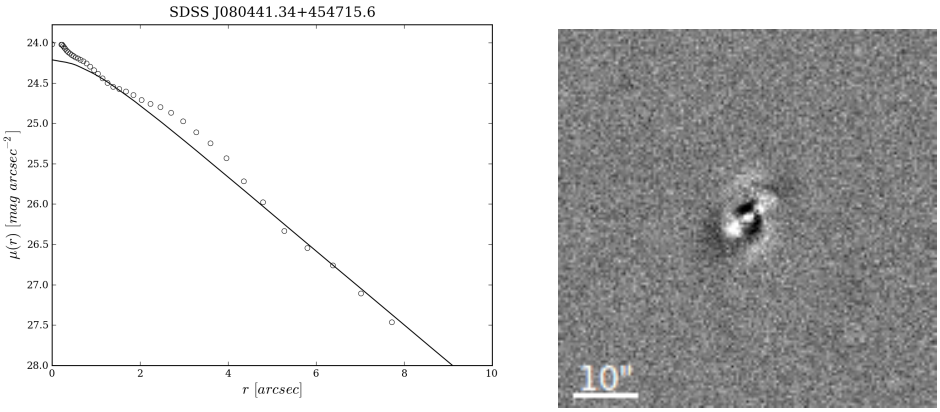

Same as Figure 3.7 but for galaxy SDSS J080441.34+454715.6.

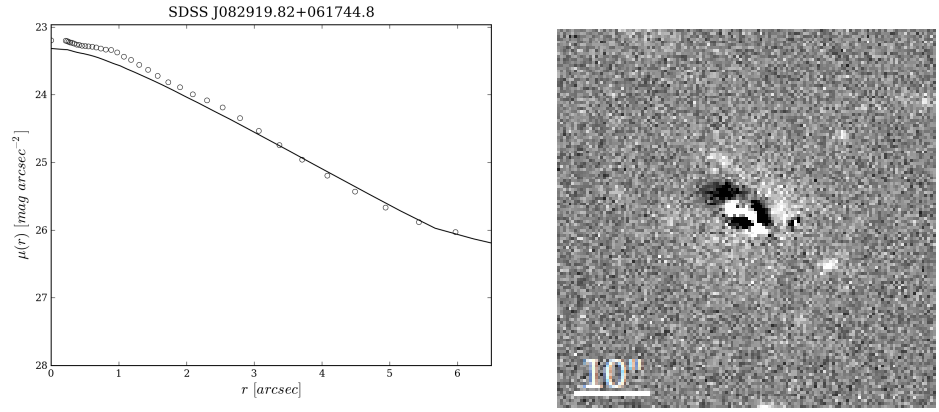

Same as Figure 3.7 but for galaxy SDSS J082919.82+061744.8.

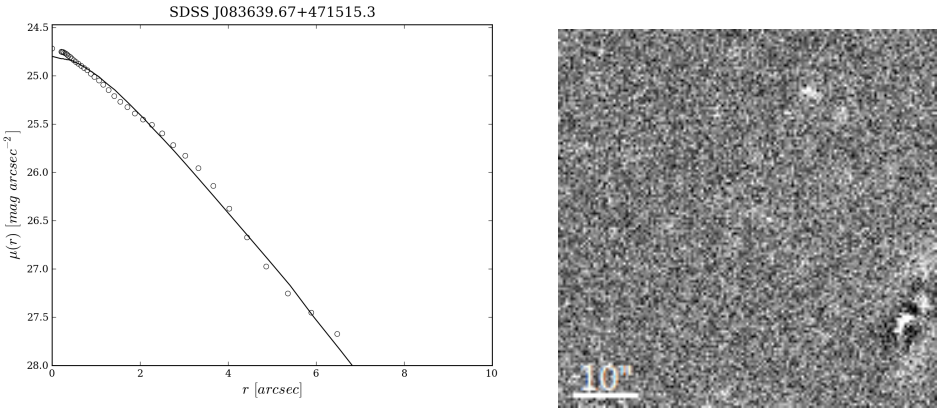

Same as Figure 3.7 but for galaxy SDSS J083639.67+471515.3.

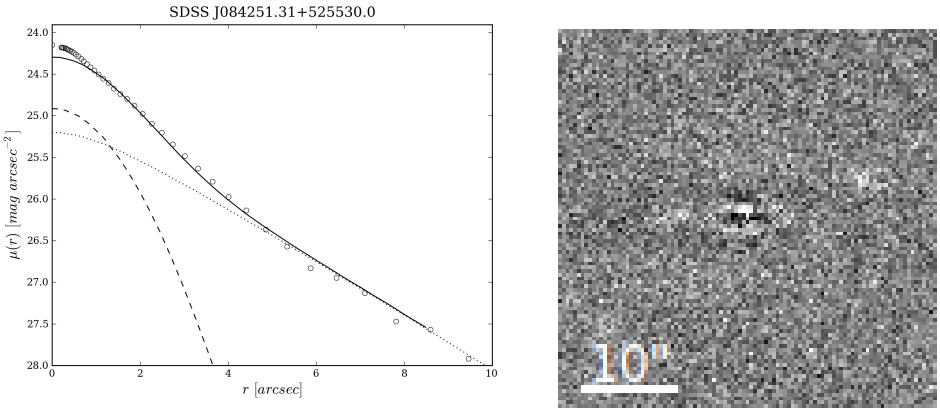

Same as Figure 3.9 but for galaxy SDSS J084251.31+525530.0.

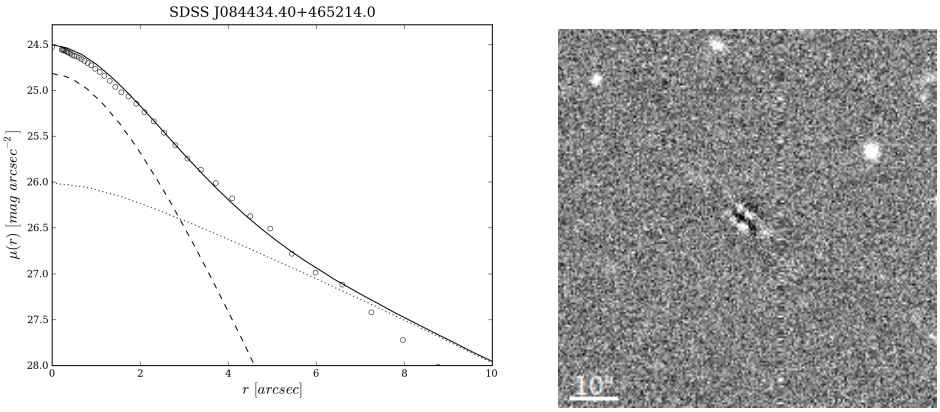

Same as Figure 3.9 but for galaxy SDSS J084434.40+465214.0.

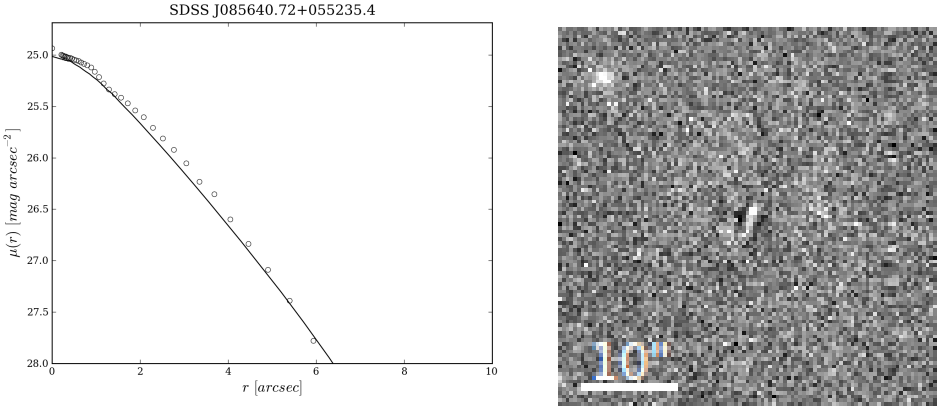

Same as Figure 3.7 but for galaxy SDSS J085640.72+055235.4.

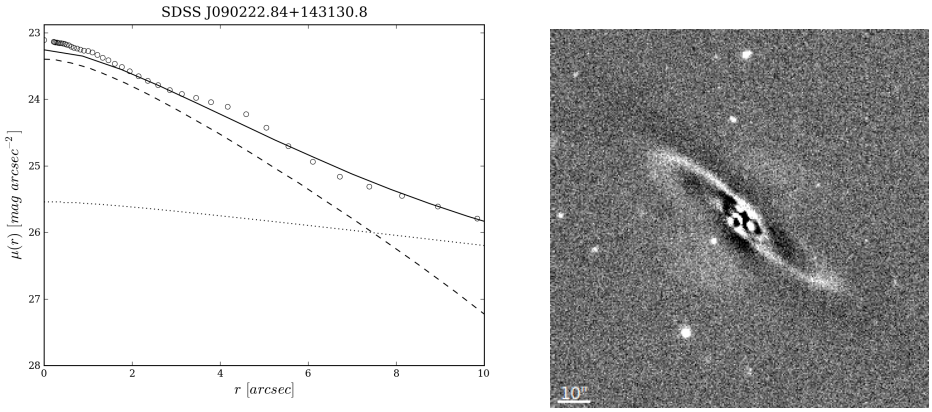

Same as Figure 3.9 but for galaxy SDSS J090222.84+143130.8.

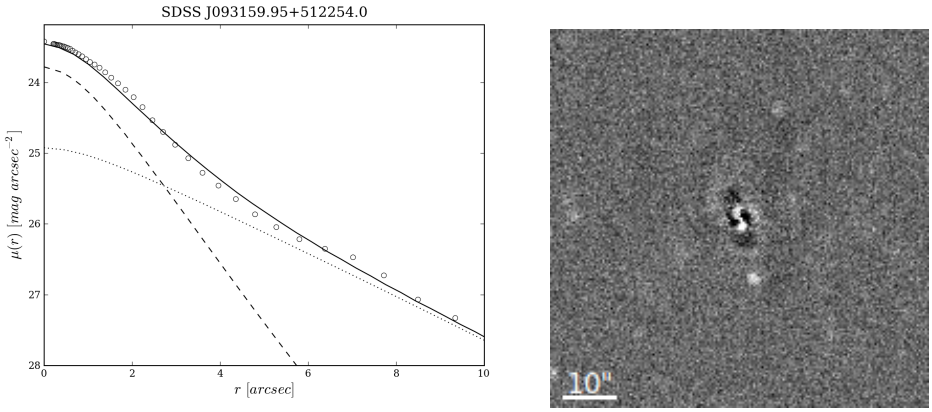

Same as Figure 3.9 but for galaxy SDSS J093159.95+512254.0.

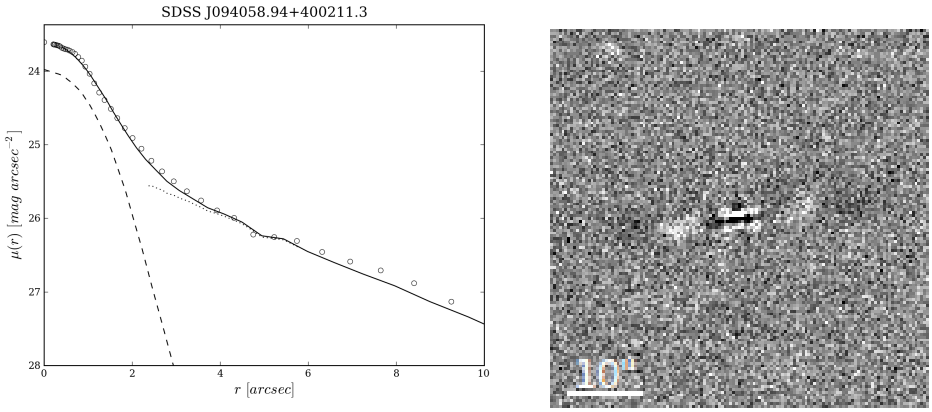

Same as Figure 3.9 but for galaxy SDSS J094058.94+400211.3.

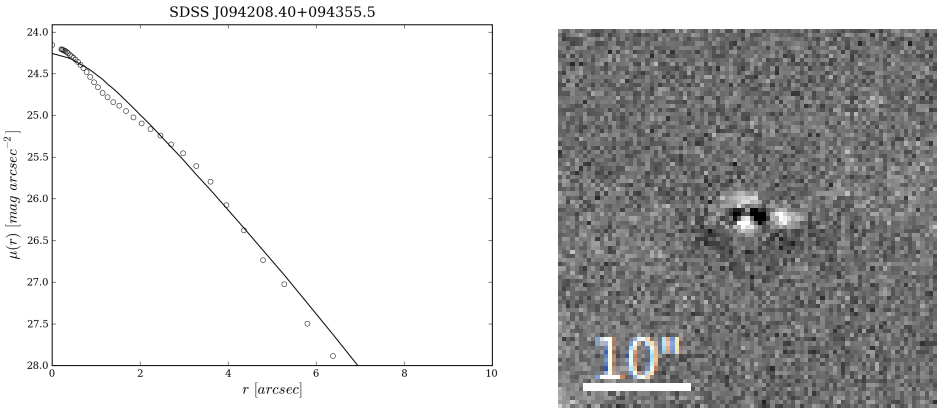

Same as Figure 3.7 but for galaxy SDSS J094208.40+094355.5.

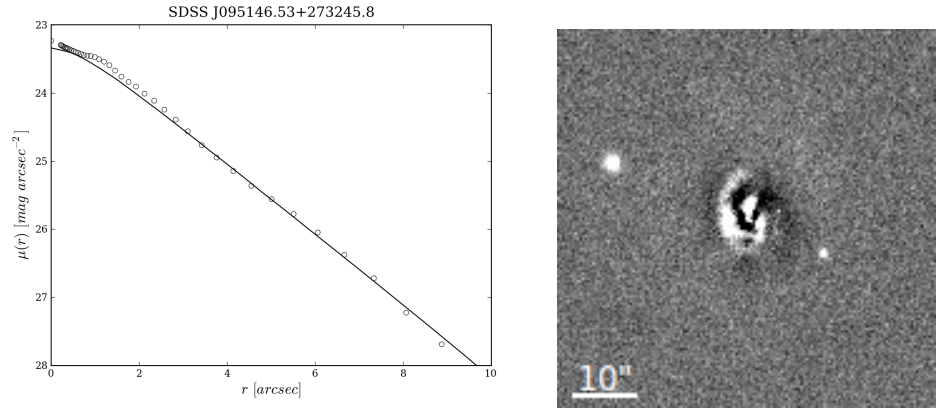

Same as Figure 3.7 but for galaxy SDSS J095146.53+273245.8.

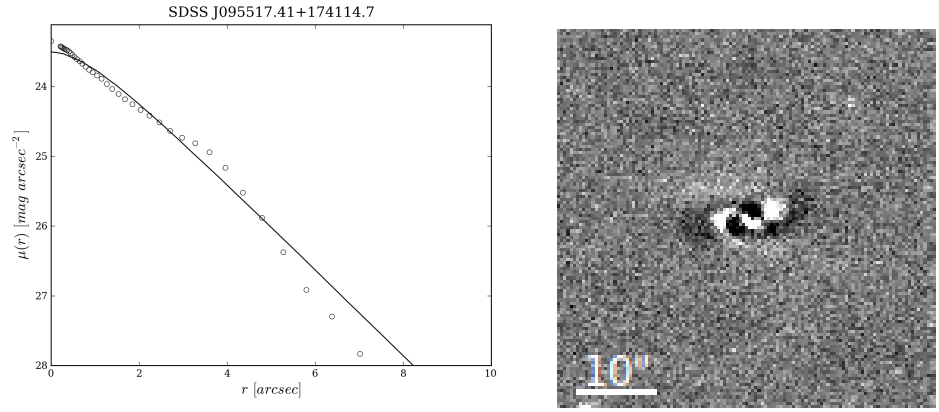

Same as Figure 3.7 but for galaxy SDSS J095517.41+174114.7.

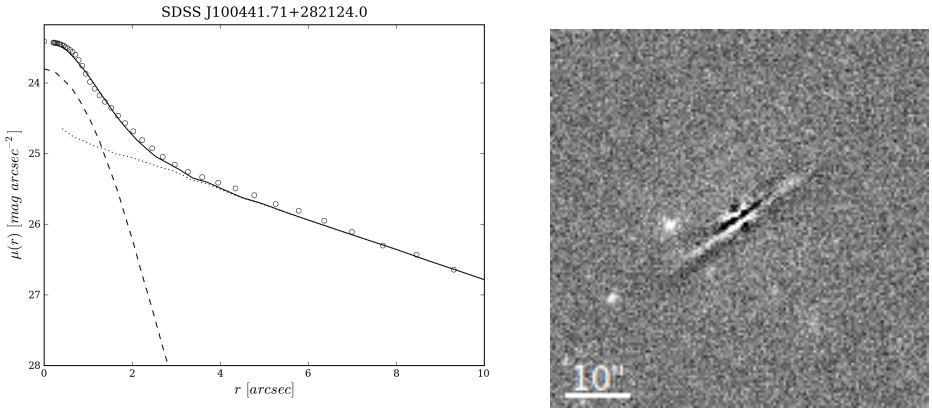

Same as Figure 3.9 but for galaxy SDSS J100441.71+282124.0.

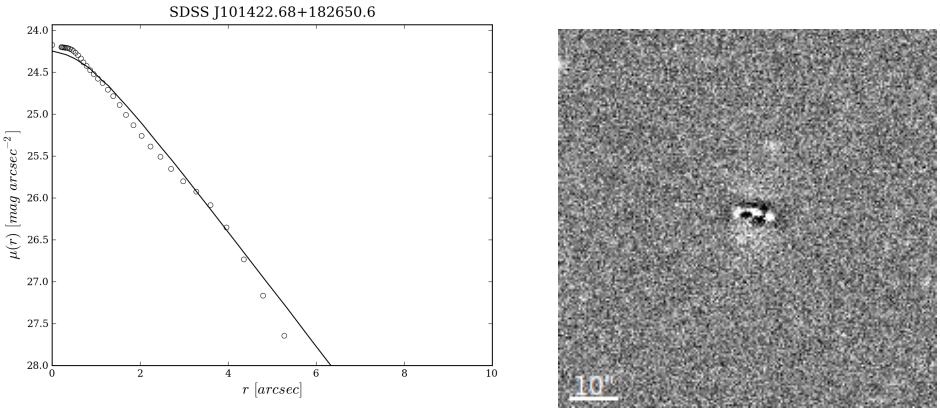

Same as Figure 3.7 but for galaxy SDSS J101422.68+182650.6.

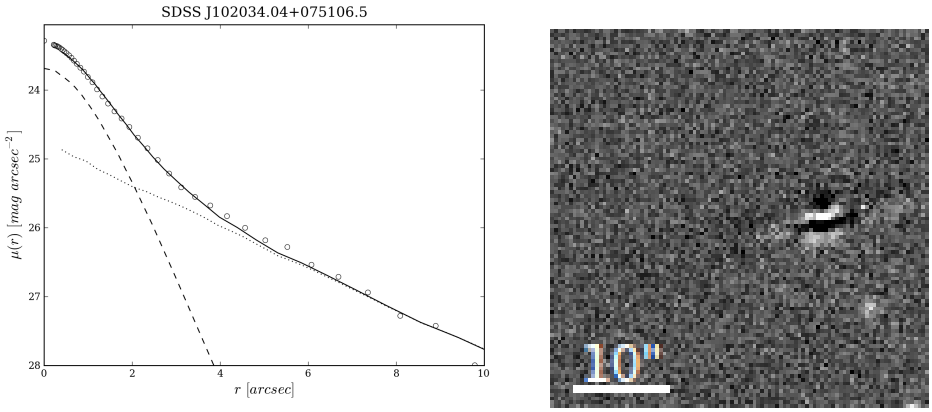

Same as Figure 3.9 but for galaxy SDSS J102034.04+075106.5.

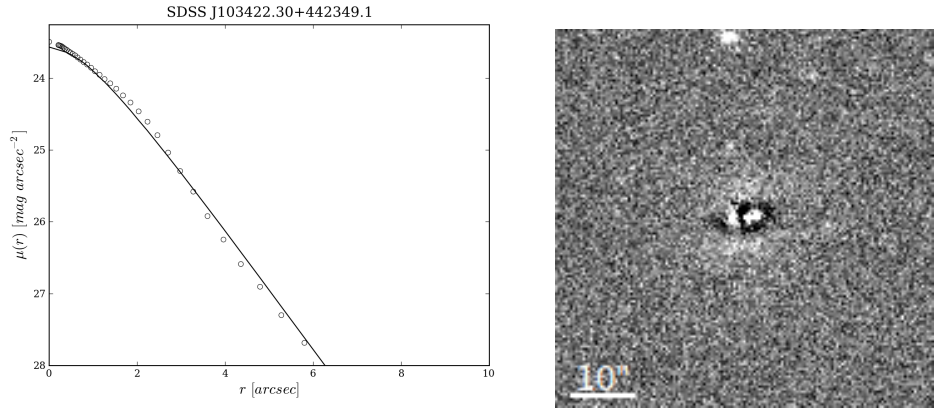

Same as Figure 3.7 but for galaxy SDSS J103422.30+442349.1.

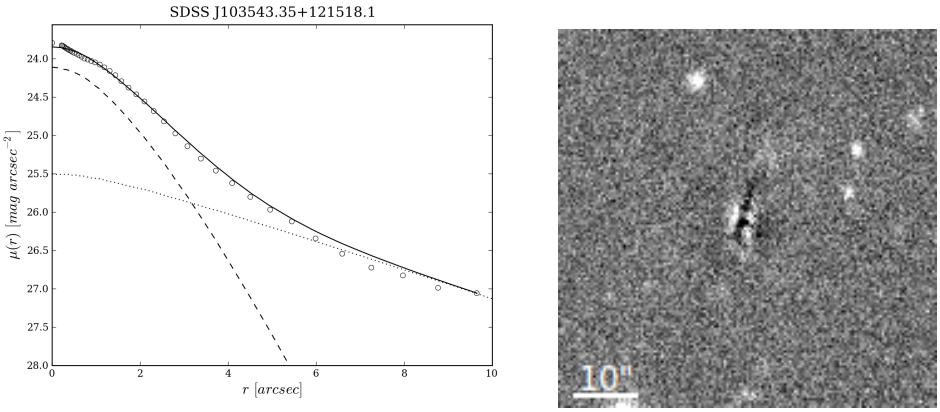

Same as Figure 3.9 but for galaxy SDSS J103543.35+121518.1.

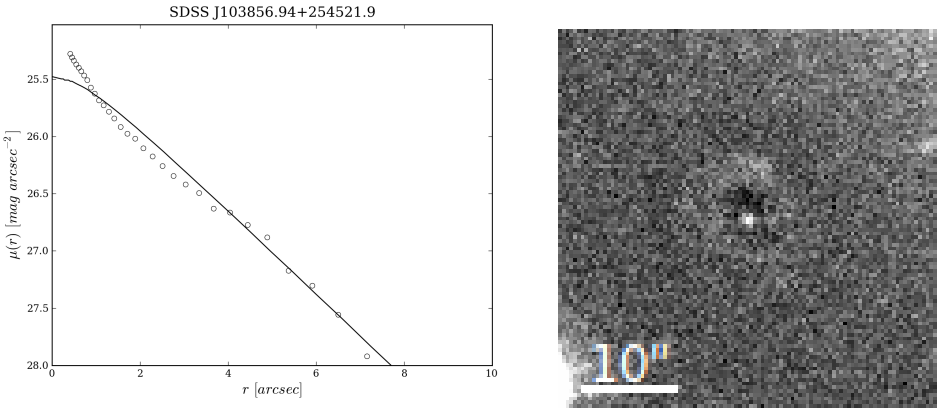

Same as Figure 3.7 but for galaxy SDSS J103856.94+254521.9.

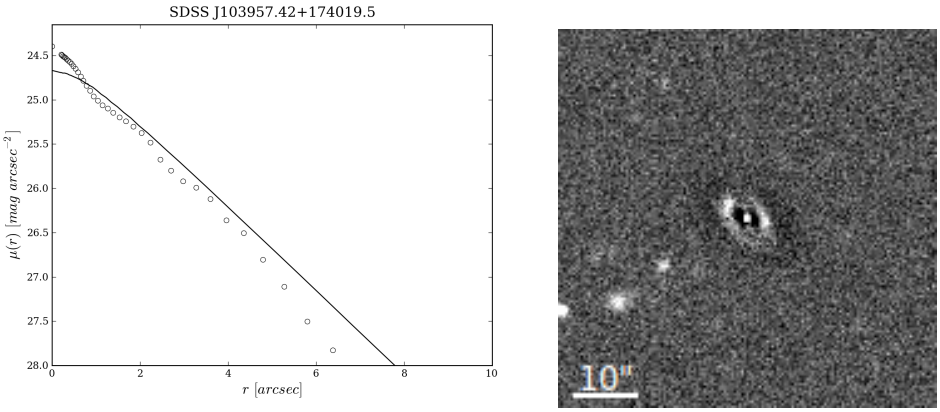

Same as Figure 3.7 but for galaxy SDSS J103957.42+174019.5.

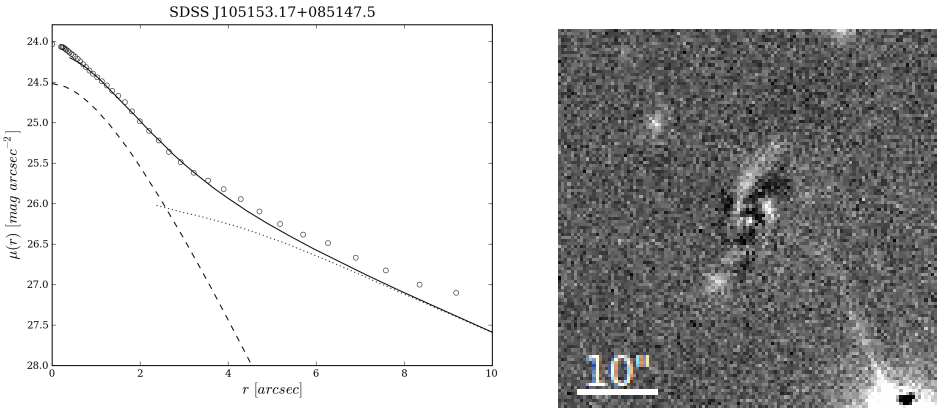

Same as Figure 3.9 but for galaxy SDSS J105153.17+085147.5.

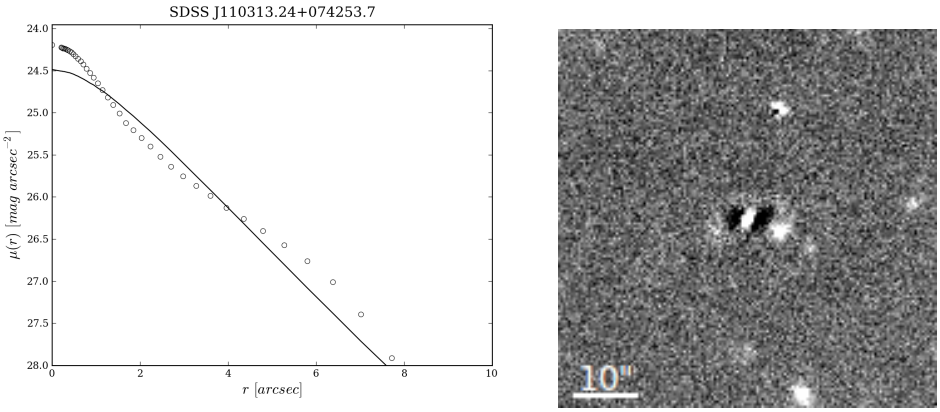

Same as Figure 3.7 but for galaxy SDSS J110313.24+074253.7.

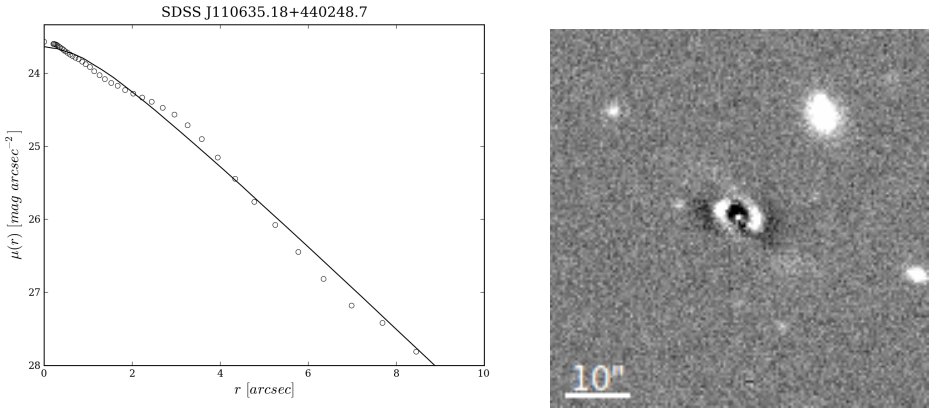

Same as Figure 3.7 but for galaxy SDSS J110635.18+440248.7.

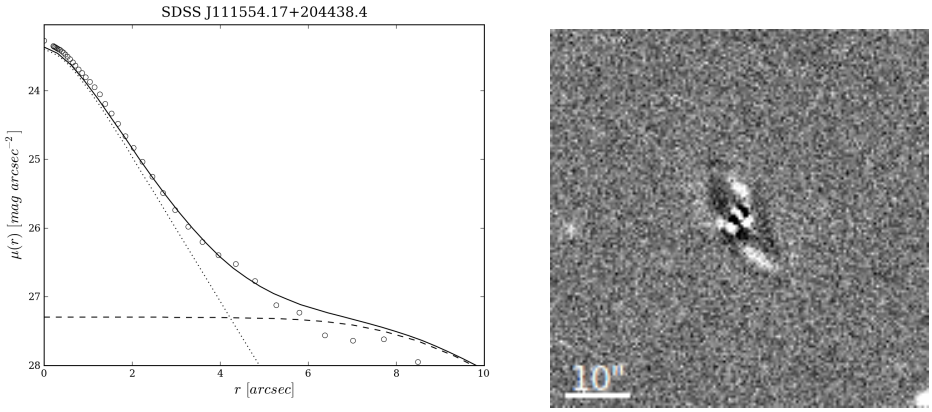

Same as Figure 3.9 but for galaxy SDSS J111554.17+204438.4.

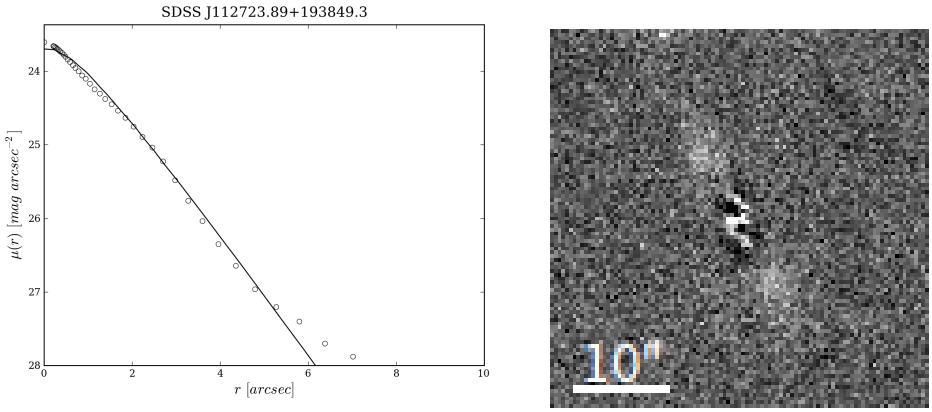

Same as Figure 3.7 but for galaxy SDSS J112723.89+193849.3.

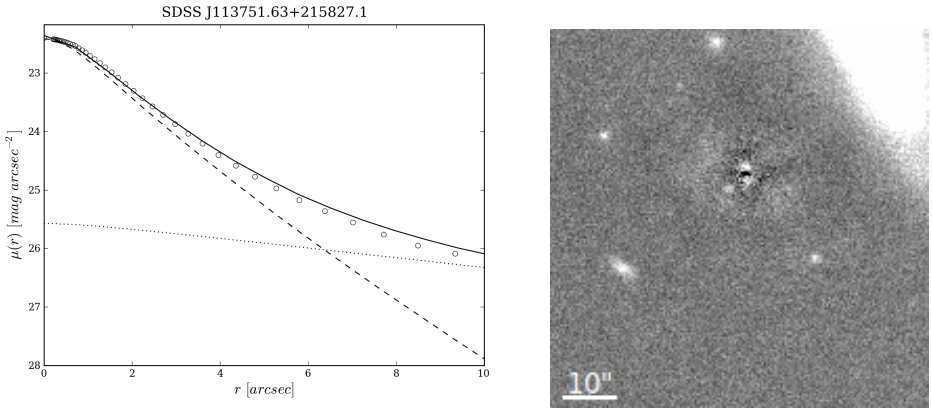

Same as Figure 3.9 but for galaxy SDSS J113751.63+215827.1.

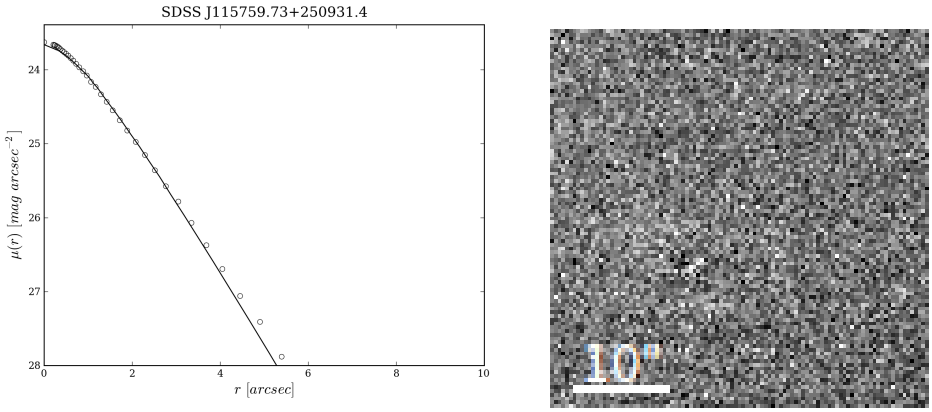

Same as Figure 3.7 but for galaxy SDSS J115759.73+250931.4.

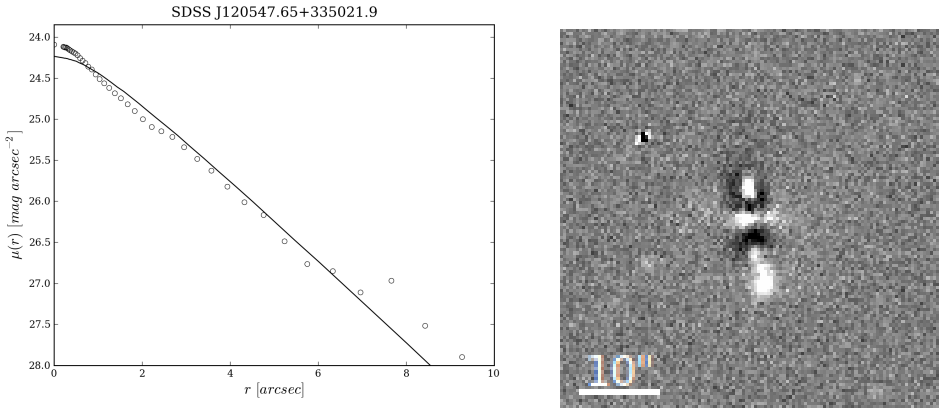

Same as Figure 3.7 but for galaxy SDSS J120547.65+335021.9.

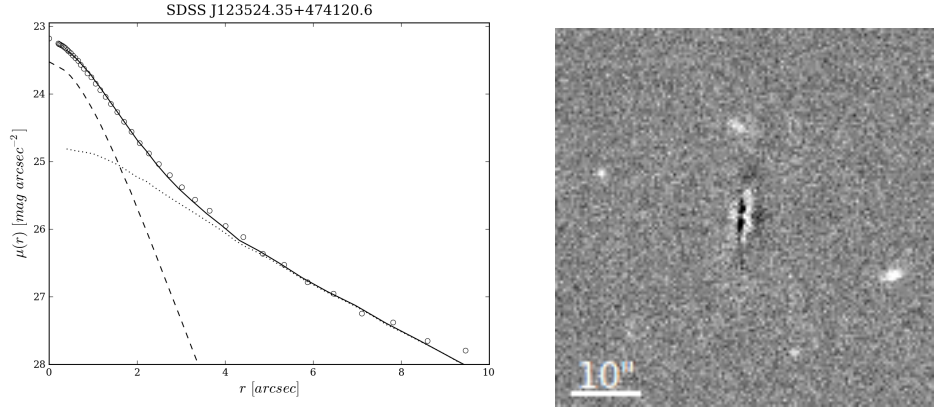

Same as Figure 3.9 but for galaxy SDSS J123524.35+474120.6.

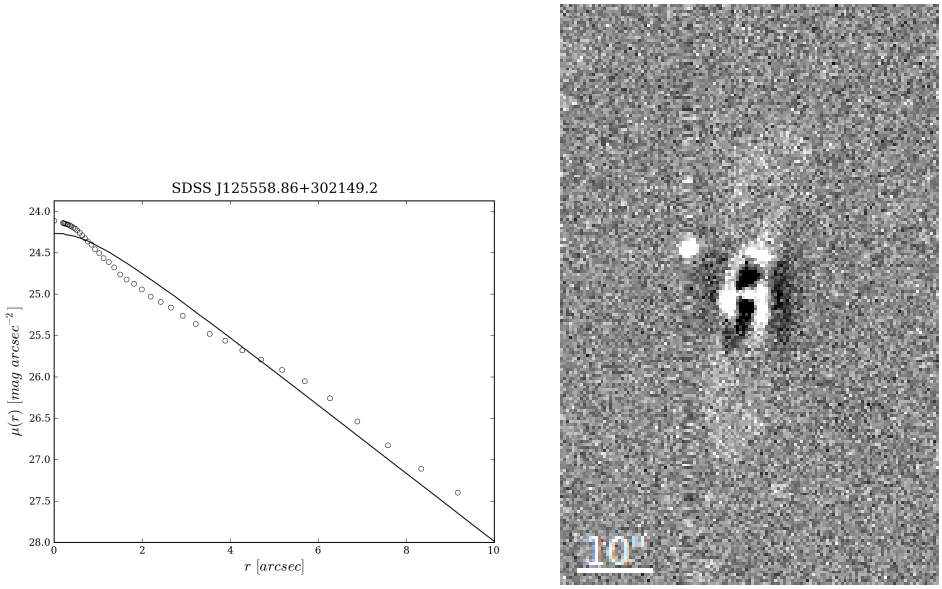

Same as Figure 3.7 but for galaxy SDSS J125558.86+302149.2.

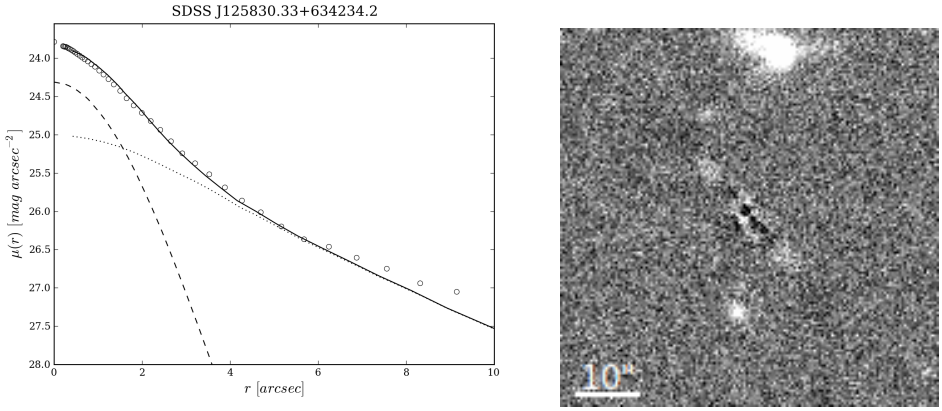

Same as Figure 3.9 but for galaxy SDSS J125830.33+634234.2.

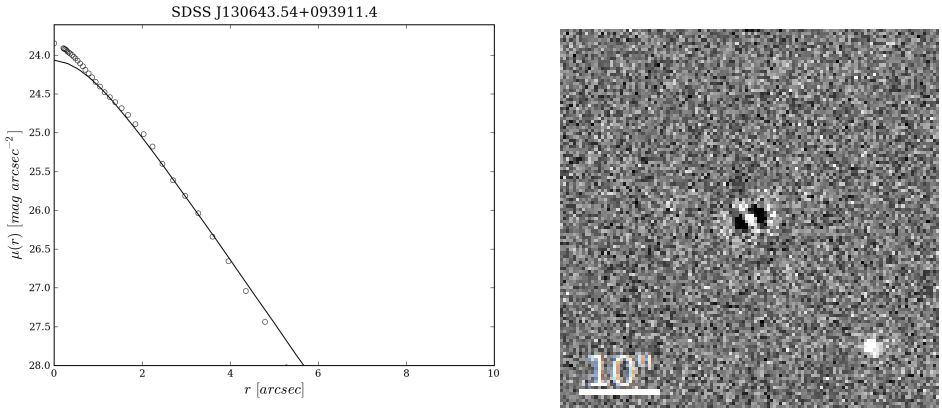

Same as Figure 3.7 but for galaxy SDSS J130643.54+093911.4.

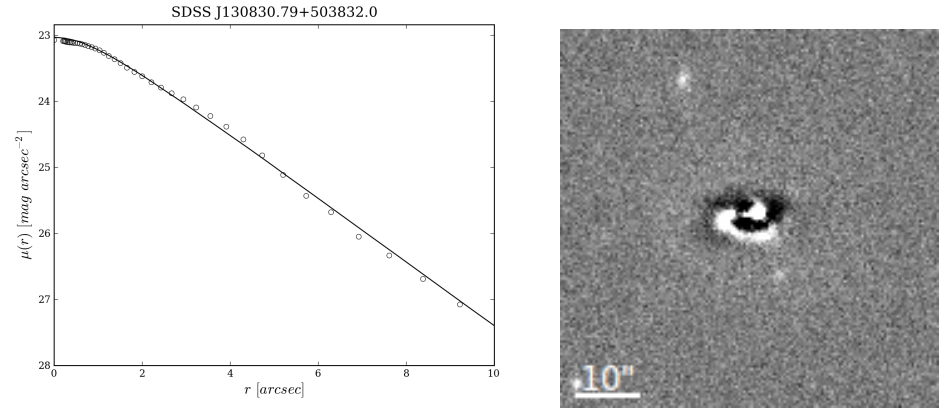

Same as Figure 3.7 but for galaxy SDSS J130830.79+503832.0.

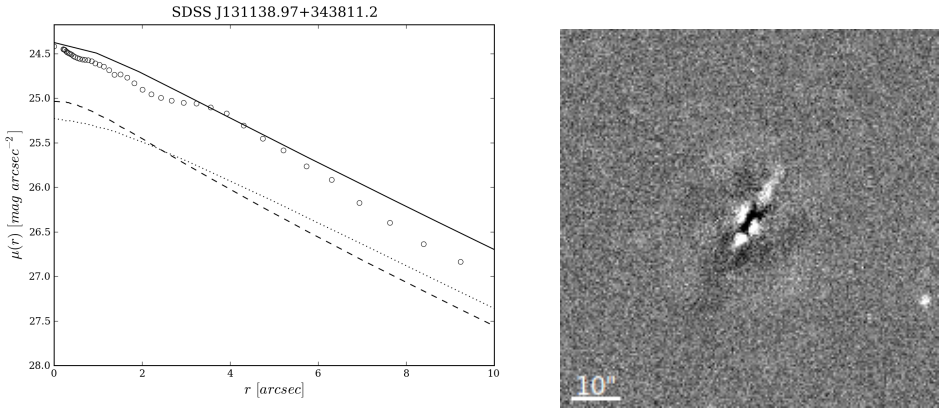

Same as Figure 3.9 but for galaxy SDSS J131138.97+343811.2.

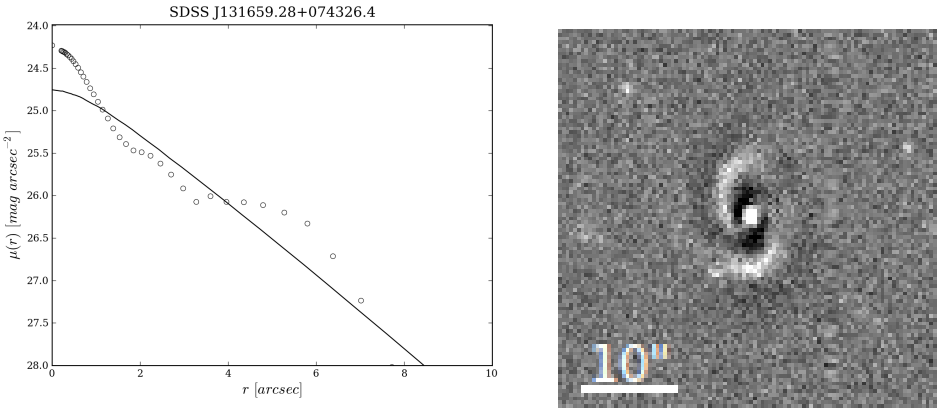

Same as Figure 3.7 but for galaxy SDSS J131659.28+074326.4.

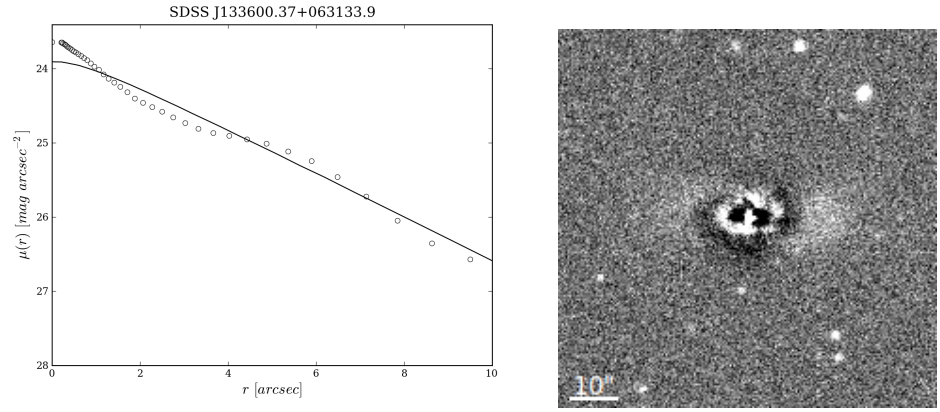

Same as Figure 3.7 but for galaxy SDSS J133600.37+063133.9.

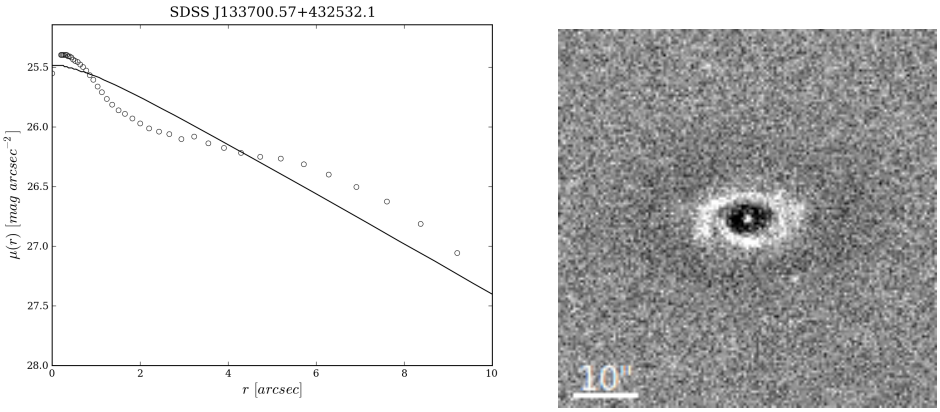

Same as Figure 3.7 but for galaxy SDSS J133700.57+432532.1.

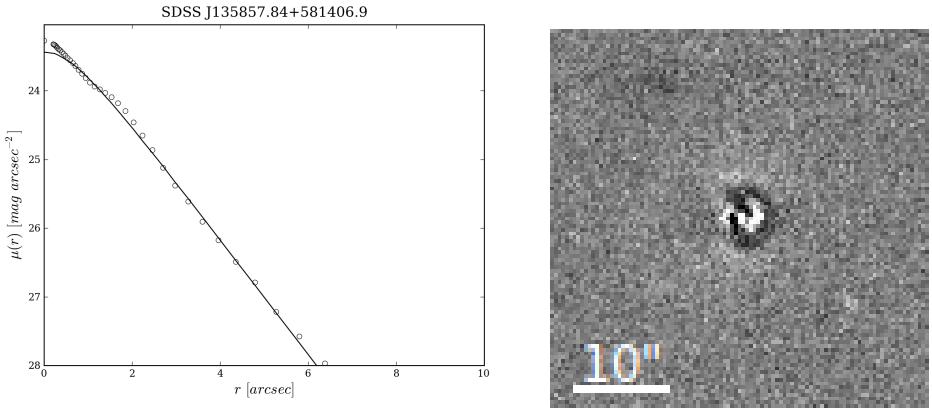

Same as Figure 3.7 but for galaxy SDSS J135857.84+581406.9.

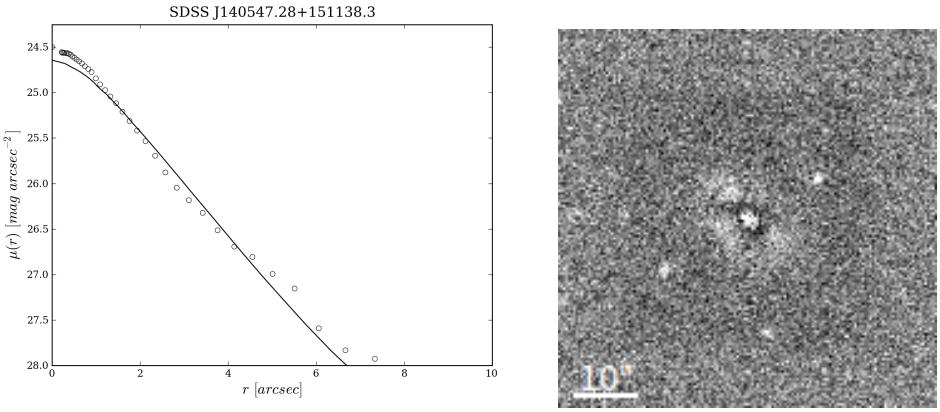

Same as Figure 3.7 but for galaxy SDSS J140547.28+151138.3.

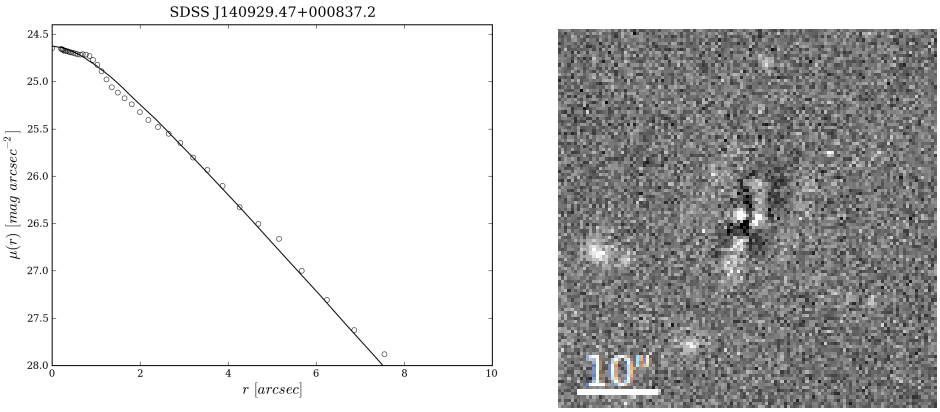

Same as Figure 3.7 but for galaxy SDSS J140929.47+000837.2.

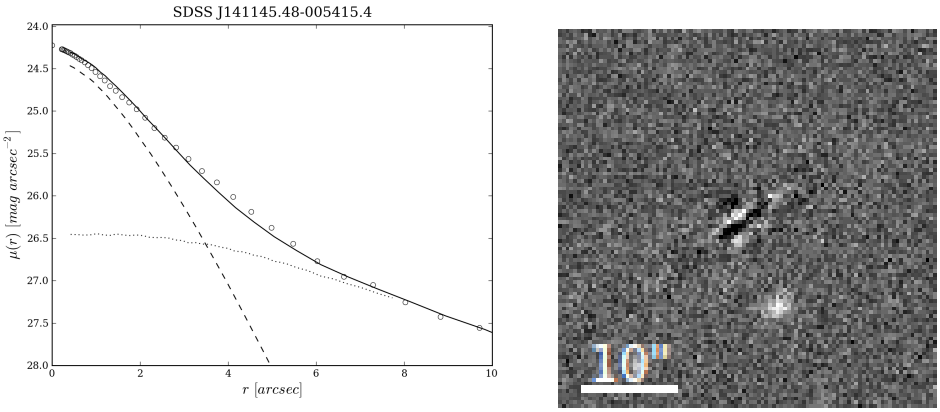

Same as Figure 3.9 but for galaxy SDSS J141145.48-005415.4.

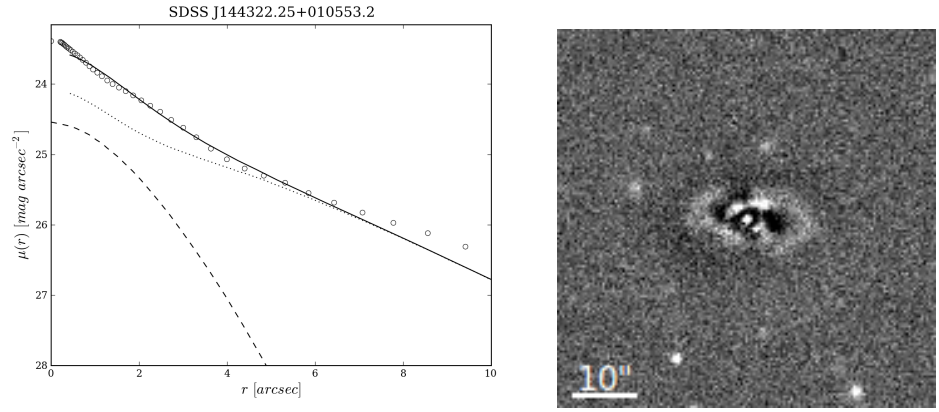

Same as Figure 3.9 but for galaxy SDSS J144322.25+010553.2.

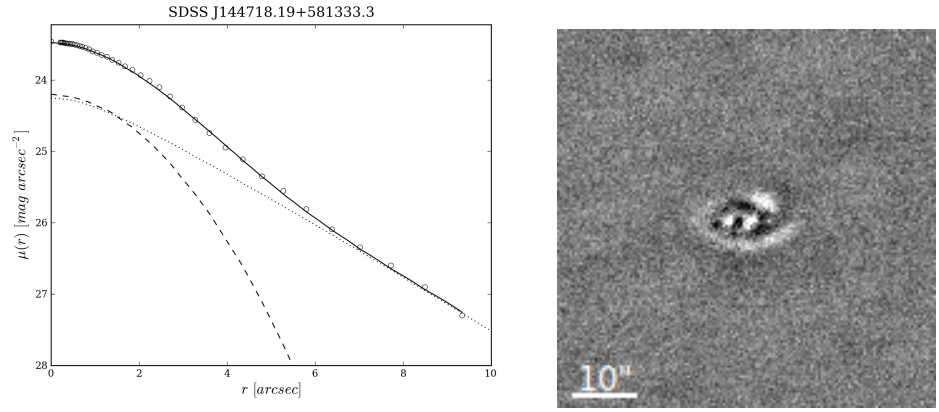

Same as Figure 3.9 but for galaxy SDSS J144718.19+581333.3.

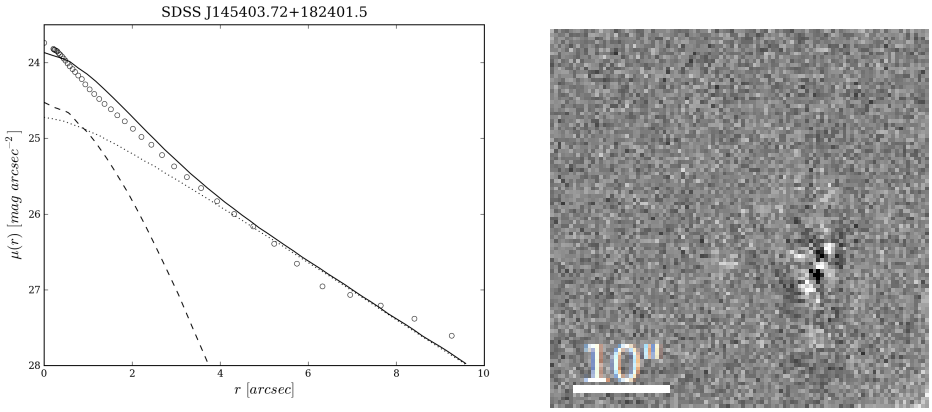

Same as Figure 3.9 but for galaxy SDSS J145403.72+182401.5.

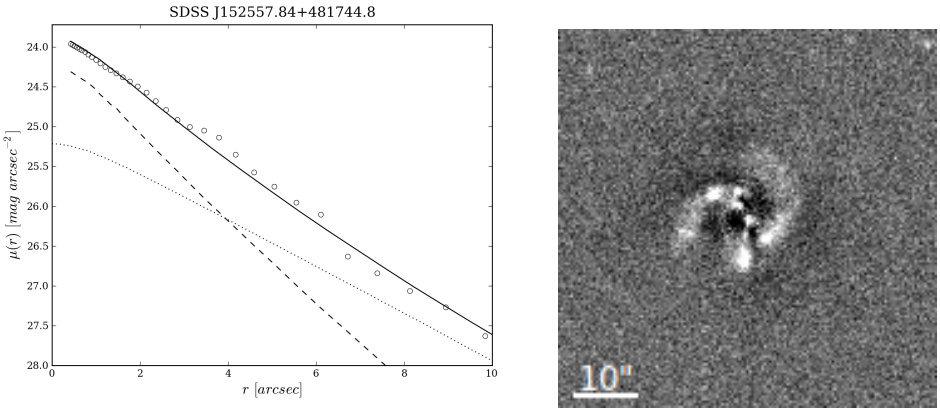

Same as Figure 3.9 but for galaxy SDSS J152557.84+481744.8.

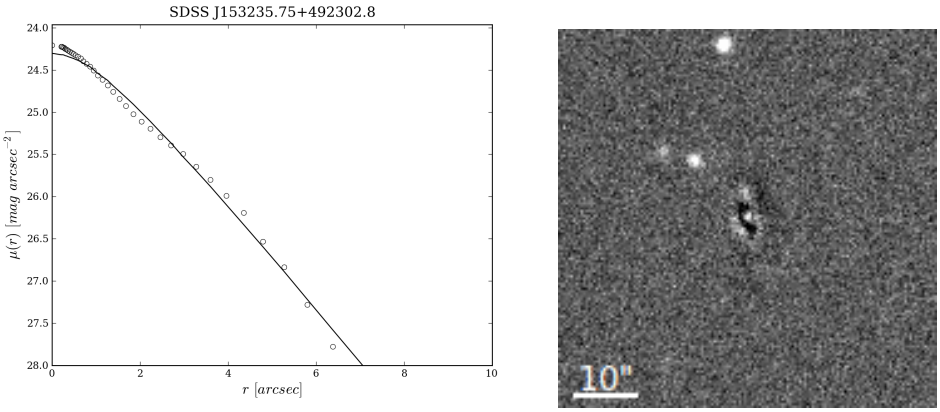

Same as Figure 3.7 but for galaxy SDSS J153235.75+492302.8.

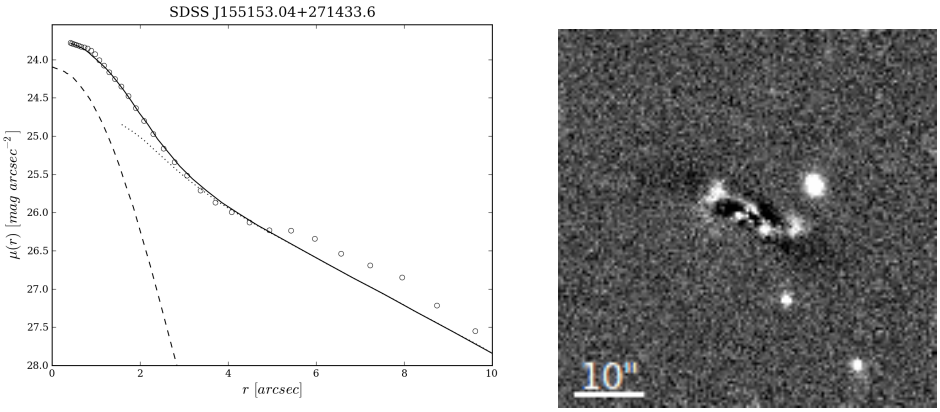

Same as Figure 3.9 but for galaxy SDSS J155153.04+271433.6.

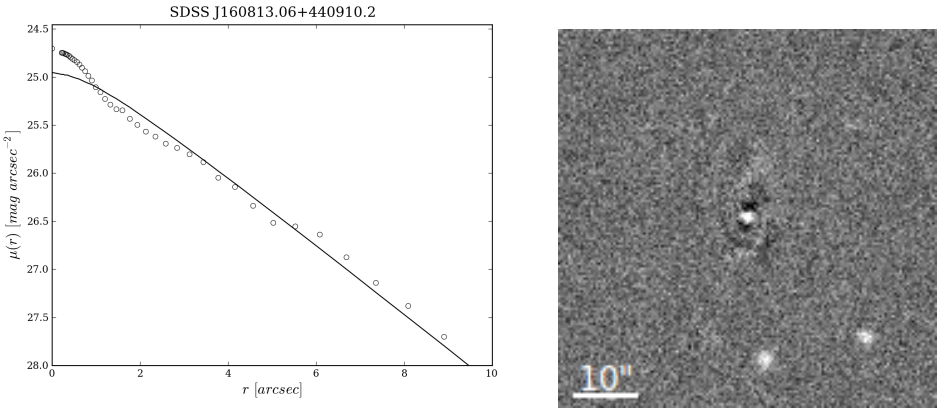

Same as Figure 3.7 but for galaxy SDSS J160813.06+440910.2.

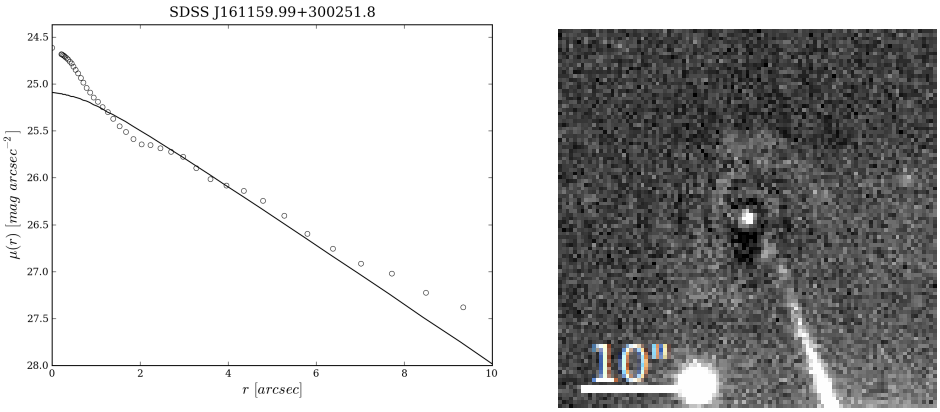

Same as Figure 3.7 but for galaxy SDSS J161159.99+300251.8.

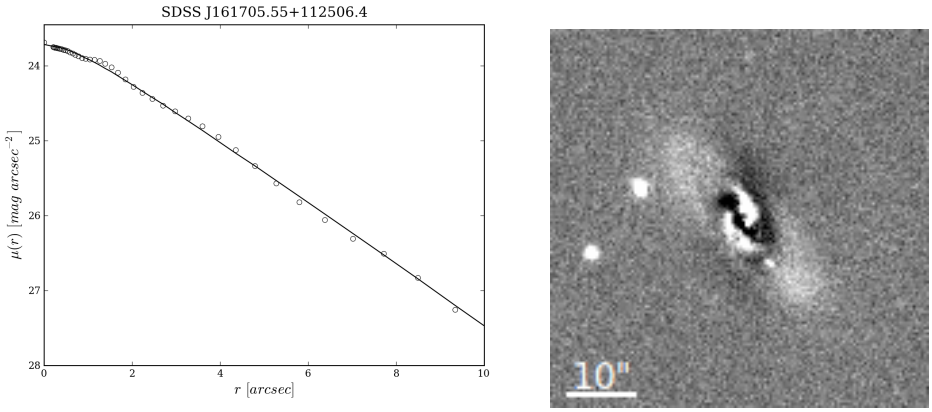

Same as Figure 3.7 but for galaxy SDSS J161705.55+112506.4.

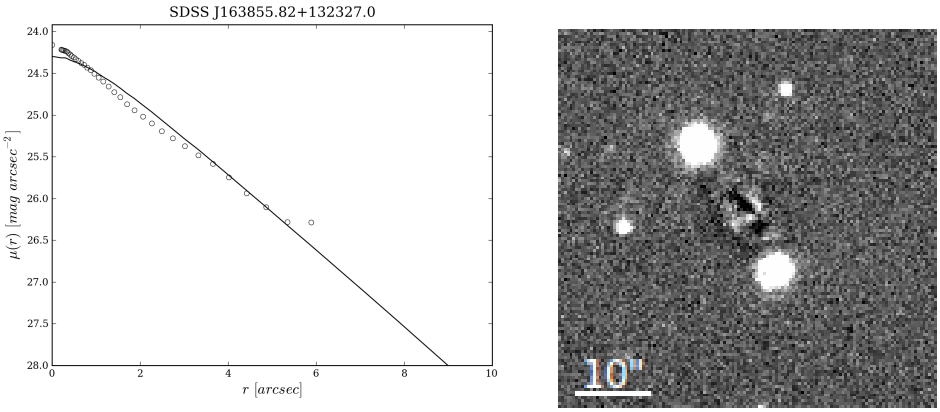

Same as Figure 3.7 but for galaxy SDSS J163855.82+132327.0.

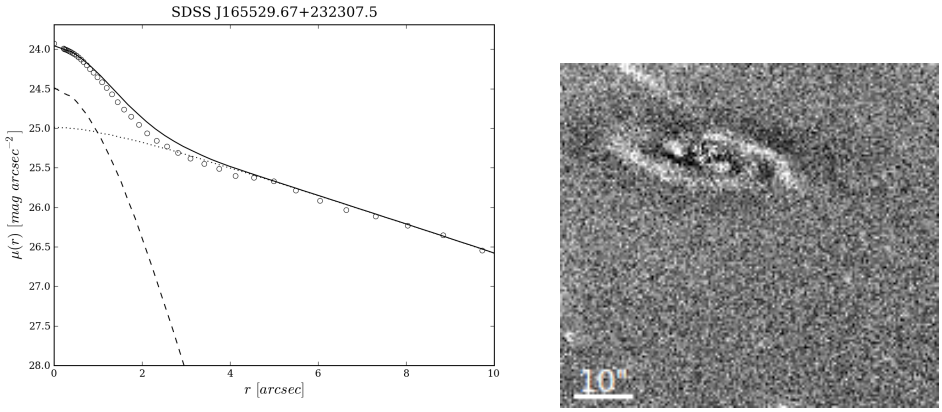

Same as Figure 3.9 but for galaxy SDSS J165529.67+232307.5.

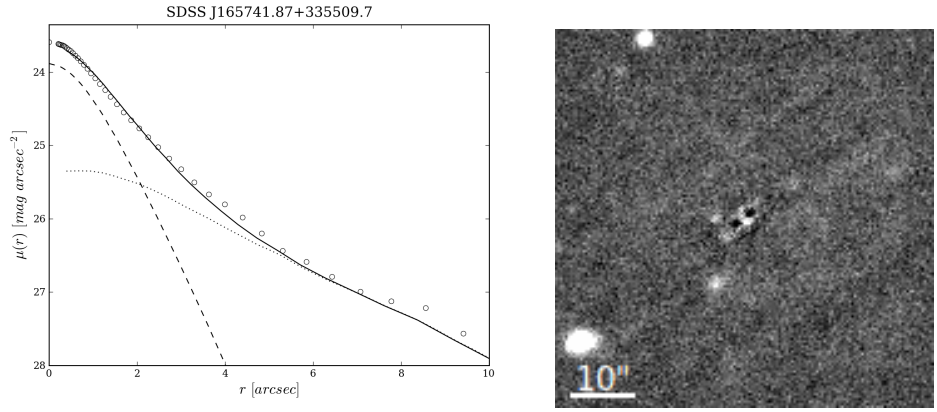

Same as Figure 3.9 but for galaxy SDSS J165741.87+335509.7.

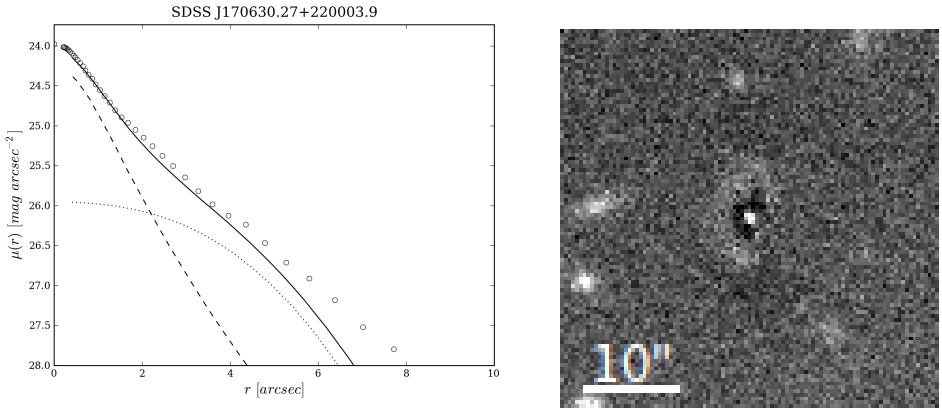

Same as Figure 3.9 but for galaxy SDSS J170630.27+220003.9.

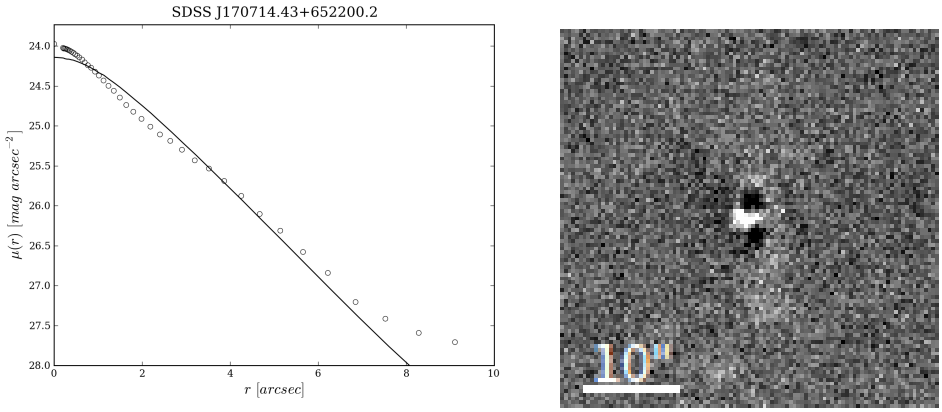

Same as Figure 3.7 but for galaxy SDSS J170714.43+652200.2.

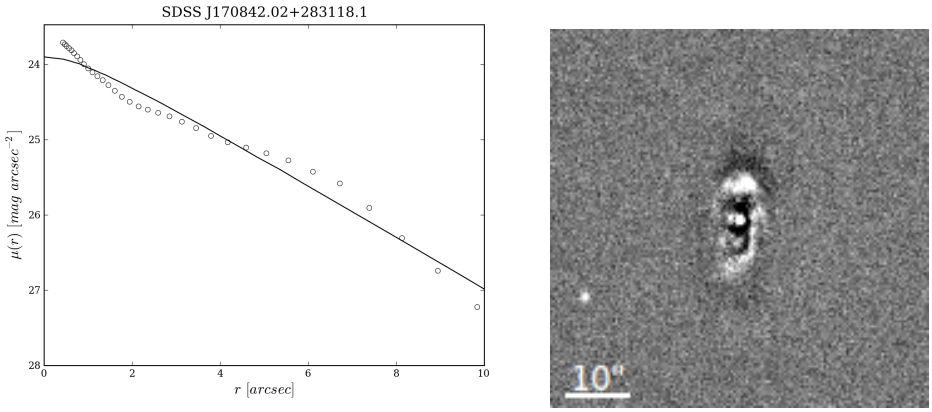

Same as Figure 3.7 but for galaxy SDSS J170842.02+283118.1.

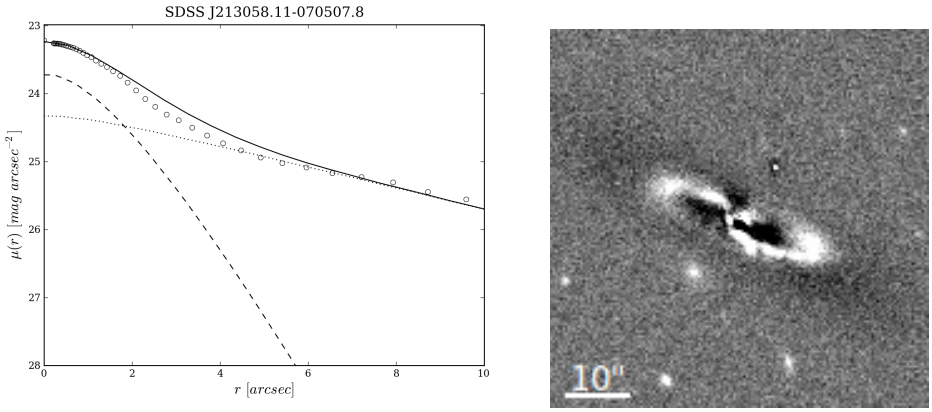

Same as Figure 3.9 but for galaxy SDSS J213058.11-070507.8.

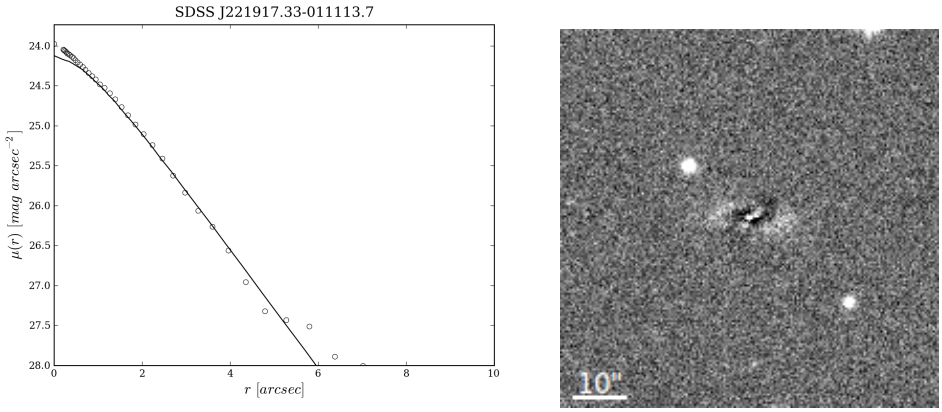

Same as Figure 3.7 but for galaxy SDSS J221917.33-011113.7.

References

[1] K. N. Abazajian, J. K. Adelman-McCarthy, M. A. Agüeros, S. S. Allam, C. Allende Prieto, D. An, K. S. J. Anderson, S. F. Anderson, J. Annis, N. A. Bahcall, and et al. The Seventh Data Release of the Sloan Digital Sky Survey. *ApJS*, 182:543–558, June 2009.

[2] J. A. L. Aguerri, M. Balcells, and R. F. Peletier. Growth of galactic bulges by mergers. I. Dense satellites. *A&A*, 367:428–442, Feb. 2001.

[3] E. Athanassoula. On the nature of bulges in general and of box/peanut bulges in particular: input from N-body simulations. *MNRAS*, 358:1477–1488, Apr. 2005.

[4] M. Balcells and R. F. Peletier. Colors and color gradients in bulges of galaxies. *AJ*, 107:135–152, Jan. 1994.

[5] J. C. Barentine and J. Kormendy. Two Pseudobulges in the "Boxy Bulge" Galaxy NGC 5746. *ApJ*, 754:140, Aug. 2012.

[6] E. F. Bell. Galaxy Bulges and their Black Holes: a Requirement for the Quenching of Star Formation. *ApJ*, 682:355–360, July 2008.

[7] J. Binney. Dynamics of elliptical galaxies and other spheroidal components. *ARA&A*, 20:399–429, 1982.

[8] M. R. Blanton, D. J. Schlegel, M. A. Strauss, J. Brinkmann, D. Finkbeiner, M. Fukugita, J. E. Gunn, D. W. Hogg, Ž. Ivezić, G. R. Knapp, R. H. Lupton, J. A. Munn, D. P. Schneider, M. Tegmark, and I. Zehavi. New York University Value-Added Galaxy Catalog: A Galaxy Catalog Based on New Public Surveys. *AJ*, 129:2562–2578, June 2005.

[9] G. Bruzual and S. Charlot. Stellar population synthesis at the resolution of 2003. *MNRAS*, 344:1000–1028, Oct. 2003.

[10] J. A. Cardelli, G. C. Clayton, and J. S. Mathis. The relationship between infrared, optical, and ultraviolet extinction. *ApJ*, 345:245–256, Oct. 1989.

[11] B. Carroll and D. Ostlie. *An introduction to modern astrophysics, ch. 25.* Pearson Addison-Wesley, 2007.

[12] R. Cid Fernandes, A. Mateus, L. Sodré, G. Stasińska, and J. M. Gomes. Semi-empirical analysis of Sloan Digital Sky Survey galaxies - I. Spectral synthesis method. *MNRAS*, 358:363–378, Apr. 2005.

[13] R. Cid Fernandes, L. Sodré, H. R. Schmitt, and J. R. S. Leão. A probabilistic formulation for empirical population synthesis: sampling methods and tests. *MNRAS*, 325:60–76, July 2001.

[14] L. Ciotti and G. Bertin. Analytical properties of the $R^{1/m}$ law. *A&A*, 352:447–451, Dec. 1999.

[15] B. Coelho. AGN feedback and quenching of star formation: a multiwavelength approach with the EURO-VO. Master's thesis, Universidade do Porto, Portugal, 2010.

[16] C. J. Conselice. The Relationship between Stellar Light Distributions of Galaxies and Their Formation Histories. *ApJS*, 147:1–28, July 2003.

[17] J. J. Dalcanton, P. Yoachim, and R. A. Bernstein. The Formation of Dust Lanes: Implications for Galaxy Evolution. *ApJ*, 608:189–207, June 2004.

[18] W. J. G. de Blok, J. M. van der Hulst, and G. D. Bothun. Surface photometry of low surface brightness galaxies. *MNRAS*, 274:235–255, May 1995.

[19] V. de Lapparent, A. Baillard, and E. Bertin. The EFIGI catalogue of 4458 nearby galaxies with morphology. II. Statistical properties along the Hubble sequence. *A&A*, 532:A75, Aug. 2011.

[20] G. de Vaucouleurs. Recherches sur les Nebuleuses Extragalactiques. *Annales d'Astrophysique*, 11:247, Jan. 1948.

[21] G. de Vaucouleurs. Classification and Morphology of External Galaxies. *Handbuch der Physik*, 53:275, 1959.

[22] S. Djorgovski and M. Davis. Fundamental properties of elliptical galaxies. *ApJ*, 313:59–68, Feb. 1987.

[23] M. C. Eliche-Moral, M. Balcells, J. A. L. Aguerri, and A. C. González-García. Growth of galactic bulges by mergers. II. Low-density satellites. *A&A*, 457:91–108, Oct. 2006.

[24] S. L. Ellison, L. Simard, N. B. Cowan, I. K. Baldry, D. R. Patton, and A. W. McConnachie. The mass-metallicity relation in galaxy clusters: the relative importance of cluster membership versus local environment. *MNRAS*, 396:1257–1272, July 2009.

[25] S. M. Faber and R. E. Jackson. Velocity dispersions and mass-to-light ratios for elliptical galaxies. *ApJ*, 204:668–683, Mar. 1976.

[26] D. B. Fisher and N. Drory. The Structure of Classical Bulges and Pseudobulges: the Link Between Pseudobulges and SÉRSIC Index. *AJ*, 136:773–839, Aug. 2008.

[27] D. B. Fisher and N. Drory. Bulges of Nearby Galaxies with Spitzer: Scaling Relations in Pseudobulges and Classical Bulges. *ApJ*, 716:942–969, June 2010.

[28] K. C. Freeman. On the Disks of Spiral and so Galaxies. *ApJ*, 160:811, June 1970.

[29] M. Fukugita, T. Ichikawa, J. E. Gunn, M. Doi, K. Shimasaku, and D. P. Schneider. The Sloan Digital Sky Survey Photometric System. *AJ*, 111:1748, Apr. 1996.

[30] D. A. Gadotti. Structural properties of pseudo-bulges, classical bulges and elliptical galaxies: a Sloan Digital Sky Survey perspective. *MNRAS*, 393:1531–1552, Mar. 2009.

[31] Y. Guo, D. H. McIntosh, H. J. Mo, N. Katz, F. C. van den Bosch, M. Weinberg, S. M. Weinmann, A. Pasquali, and X. Yang. Structural properties of central galaxies in groups and clusters. *MNRAS*, 398:1129–1149, Sept. 2009.

[32] E. P. Hubble. Extragalactic nebulae. *ApJ*, 64:321–369, Dec. 1926.

[33] P. Jablonka, P. Martin, and N. Arimoto. The Luminosity-Metallicity Relation for Bulges of Spiral Galaxies. *AJ*, 112:1415, Oct. 1996.

[34] R. I. Jedrzejewski. CCD surface photometry of elliptical galaxies. I - Observations, reduction and results. *MNRAS*, 226:747–768, June 1987.

[35] W. A. Joye and E. Mandel. New Features of SAOImage DS9. In H. E. Payne, R. I. Jedrzejewski, and R. N. Hook, editors, *Astronomical Data Analysis Software and Systems XII*, volume 295 of *Astronomical Society of the Pacific Conference Series*, page 489, 2003.

[36] S. J. Kautsch. The Edge-On Perspective of Bulgeless, Simple Disk Galaxies. *PASP*, 121:1297–1306, Dec. 2009.

[37] J. A. Keselman and A. Nusser. Pseudo-bulge formation via major mergers. *MNRAS*, 424:1232–1243, Aug. 2012.

[38] S. Khochfar. Merger History of Galaxies and Disk+Bulge Formation. In S. Jogee, I. Marinova, L. Hao, and G. A. Blanc, editors, *Galaxy Evolution: Emerging Insights and Future Challenges*, volume 419 of *Astronomical Society of the Pacific Conference Series*, page 197, Dec. 2009.

[39] J. Kormendy. Observations of galaxy structure and dynamics. In L. Martinet and M. Mayor, editors, *Saas-Fee Advanced Course 12: Morphology and Dynamics of Galaxies*, pages 113–288, 1982.

[40] J. Kormendy, R. Bender, and M. E. Cornell. Supermassive black holes do not correlate with galaxy disks or pseudobulges. *Nature*, 469:374–376, Jan. 2011.

[41] J. Kormendy, N. Drory, R. Bender, and M. E. Cornell. Bulgeless Giant Galaxies Challenge Our Picture of Galaxy Formation by Hierarchical Clustering. *ApJ*, 723:54–80, Nov. 2010.

[42] J. Kormendy and R. C. Kennicutt, Jr. Secular Evolution and the Formation of Pseudobulges in Disk Galaxies. *ARA&A*, 42:603–683, Sept. 2004.

[43] M. Kregel and P. C. van der Kruit. Radial truncations in stellar discs in galaxies. *MNRAS*, 355:143–146, Nov. 2004.

[44] D. Larson, J. Dunkley, G. Hinshaw, E. Komatsu, M. R. Nolta, C. L. Bennett, B. Gold, M. Halpern, R. S. Hill, N. Jarosik, A. Kogut, M. Limon, S. S. Meyer, N. Odegard, L. Page, K. M. Smith, D. N. Spergel, G. S. Tucker, J. L. Weiland, E. Wollack, and E. L. Wright. Seven-year Wilkinson Microwave Anisotropy Probe (WMAP) Observations: Power Spectra and WMAP-derived Parameters. *ApJS*, 192:16, Feb. 2011.

[45] L. D. Matthews and J. S. Gallagher, III. B and V CCD Photometry of Southern, Extreme Late-Type Spiral Galaxies. *AJ*, 114:1899, Nov. 1997.

[46] L. D. Matthews and J. M. Uson. H I Imaging Observations of Superthin Galaxies. II. IC 2233 and the Blue Compact Dwarf NGC 2537. *AJ*, 135:291–318, Jan. 2008.

[47] H. Mo, F. C. van den Bosch, and S. White. *Galaxy Formation and Evolution*. 2010.

[48] A. Oemler, Jr. The Systematic Properties of Clusters of Galaxies. Photometry of 15 Clusters. *ApJ*, 194:1–20, Nov. 1974.

[49] C. Y. Peng, L. C. Ho, C. D. Impey, and H.-W. Rix. Detailed Structural Decomposition of Galaxy Images. *AJ*, 124:266–293, July 2002.

[50] C. Y. Peng, L. C. Ho, C. D. Impey, and H.-W. Rix. Detailed Decomposition of Galaxy Images. II. Beyond Axisymmetric Models. *AJ*, 139:2097–2129, June 2010.

[51] M. Pohlen and I. Trujillo. The structure of galactic disks. Studying late-type spiral galaxies using SDSS. *A&A*, 454:759–772, Aug. 2006.

[52] W. H. Press, S. A. Teukolsky, W. T. Vetterling, and B. P. Flannery. *Numerical Recipes 3rd Edition: The Art of Scientific Computing*. Cambridge University Press, New York, NY, USA, 3 edition, 2007.

[53] C. W. Purcell, S. Kazantzidis, and J. S. Bullock. Galactic Disk Transformation via Massive Satellite Accretion Events. In S. Jogee, I. Marinova, L. Hao, and G. A. Blanc, editors, *Galaxy Evolution: Emerging Insights and Future Challenges*, volume 419 of *Astronomical Society of the Pacific Conference Series*, page 248, Dec. 2009.

[54] R. Roškar, V. P. Debattista, G. S. Stinson, T. R. Quinn, T. Kaufmann, and J. Wadsley. Beyond Inside-Out Growth: Formation and Evolution of Disk Outskirts. *ApJL*, 675:L65–L68, Mar. 2008.

[55] J. L. Sersic. *Atlas de galaxias australes*. 1968.

[56] L. Sparke and I. John S. Gallagher. *Galaxies in the Universe: An Introduction*. Cambridge University Press, 2007.

[57] S. van den Bergh. A Preliminary Luminosity Clssification of Late-Type Galaxies. *ApJ*, 131:215, Jan. 1960.

[58] F. C. van den Bosch. The Formation of Disk-Bulge-Halo Systems and the Origin of the Hubble Sequence. *ApJ*, 507:601–614, Nov. 1998.

[59] P. C. van der Kruit. Optical surface photometry of eight spiral galaxies studied in Westerbork. *A&AS*, 38:15–38, Oct. 1979.

[60] R. A. Vincent and B. S. Ryden. The Dependence of Galaxy Shape on Luminosity and Surface Brightness Profile. *ApJ*, 623:137–147, Apr. 2005.

[61] Y. Wadadekar, B. Robbason, and A. Kembhavi. Two-dimensional Galaxy Image Decomposition. *AJj*, 117:1219–1228, Mar. 1999.

[62] D. G. York, J. Adelman, J. E. Anderson, Jr., S. F. Anderson, J. Annis, N. A. Bahcall, J. A. Bakken, R. Barkhouser, S. Bastian, E. Berman, W. N. Boroski, S. Bracker, C. Briegel, J. W. Briggs, J. Brinkmann, R. Brunner, S. Burles, L. Carey, M. A. Carr, F. J. Castander, B. Chen, P. L. Colestock, A. J. Connolly, J. H. Crocker, I. Csabai, P. C. Czarapata, J. E. Davis, M. Doi, T. Dombeck, D. Eisenstein, N. Ellman, B. R. Elms, M. L. Evans, X. Fan, G. R. Federwitz, L. Fiscelli, S. Friedman, J. A. Frieman, M. Fukugita, B. Gillespie, J. E. Gunn, V. K. Gurbani, E. de Haas, M. Haldeman, F. H. Harris, J. Hayes, T. M. Heckman, G. S. Hennessy, R. B. Hindsley, S. Holm, D. J. Holmgren, C.-h. Huang, C. Hull, D. Husby, S.-I. Ichikawa, T. Ichikawa, Ž. Ivezić, S. Kent, R. S. J. Kim, E. Kinney, M. Klaene, A. N. Kleinman, S. Kleinman, G. R. Knapp, J. Korienek, R. G. Kron, P. Z. Kunszt, D. Q. Lamb, B. Lee, R. F. Leger, S. Limmongkol, C. Lindenmeyer, D. C. Long, C. Loomis, J. Loveday, R. Lucinio, R. H. Lupton, B. MacKinnon, E. J. Mannery, P. M. Mantsch, B. Margon, P. McGehee, T. A. McKay, A. Meiksin, A. Merelli, D. G. Monet, J. A. Munn, V. K. Narayanan, T. Nash, E. Neilsen, R. Neswold, H. J. Newberg, R. C. Nichol, T. Nicinski, M. Nonino, N. Okada, S. Okamura, J. P. Ostriker, R. Owen, A. G. Pauls, J. Peoples, R. L. Peterson, D. Petravick, J. R. Pier, A. Pope, R. Pordes, A. Prosapio, R. Rechenmacher, T. R. Quinn, G. T. Richards, M. W. Richmond, C. H. Rivetta, C. M. Rockosi, K. Ruthmansdorfer, D. Sandford, D. J. Schlegel, D. P. Schneider, M. Sekiguchi, G. Sergey, K. Shimasaku, W. A. Siegmund, S. Smee, J. A. Smith, S. Snedden, R. Stone, C. Stoughton, M. A. Strauss, C. Stubbs, M. SubbaRao, A. S. Szalay, I. Szapudi, G. P. Szokoly, A. R. Thakar, C. Tremonti, D. L. Tucker, A. Uomoto, D. Vanden Berk, M. S. Vogeley, P. Waddell, S.-i. Wang, M. Watanabe, D. H. Weinberg, B. Yanny, N. Yasuda, and SDSS Collaboration. The Sloan Digital Sky Survey: Technical Summary. *AJ*, 120:1579–1587, Sept. 2000.

[63] J. Zavala, V. Avila-Reese, C. Firmani, and M. Boylan-Kolchin. The growth of galactic bulges through mergers in LCDM haloes revisited. I. Present-day properties. *ArXiv e-prints*, Apr. 2012.